Investigation of Triggering Mechanism of Internal Transport Barriers on the Alcator C-Mod Tokamak Using Thomson Scattering Diagnostic

by

Kirill Zhurovich

B.S. Applied Mathematics and Physics (1998)
M.S. Applied Mathematics and Physics (2000)
Moscow Institute of Physics and Technology

Submitted to the Department of Nuclear Science and Engineering in partial fulfillment of the requirement for the degree of

Doctor of Philosophy in Nuclear Science and Engineering

at the

MASSACHUSETTS INSTITUTE OF TECHNOLOGY
[September 2007]
August 2007

Author .....
Department of Nuclear Science and Engineering
August 1, 2007

Certified by .....
Catherine Fiore
Research Scientist, Plasma Science and Fusion Center
Thesis Supervisor

Certified by .....
Ian Hutchinson
Professor of Nuclear Science and Engineering, Department Head
Thesis Reader

Certified by .....
Darin Ernst
Research Scientist, Plasma Science and Fusion Center
Thesis Reader

Certified by .....
Professor Jeffrey A. Coderre
Chairman, Department Committee on Graduate Students

Investigation of Triggering Mechanism of Internal Transport Barriers on the Alcator C-Mod Tokamak Using Thomson Scattering Diagnostic

by

Kirill Zhurovich

Submitted to the Department of Nuclear Science and Engineering on August 1, 2007, in partial fulfillment of the requirements for the degree of Doctor of Philosophy in Nuclear Science and Engineering

Abstract

Internal transport barriers (ITBs) in tokamak plasmas are characterized by the reduction of transport in one or more of the particle, momentum, or energy channels in the core plasma region. On Alcator C-Mod, significant contributions to ITB studies were made possible with the core Thomson scattering (TS) diagnostic, which measures profiles of electron temperature ($0.03 \leq T_e[\text{keV}] \leq 10$) and density ($0.05 \leq n_e[10^{20}\text{m}^{-3}] \leq 5$) with ~1 cm resolution in the ITB region. For the transport analysis purposes, TS profiles are complemented by measurements from other diagnostics and fitted with smooth curves.

This thesis research examines the plasma conditions necessary to trigger ITBs on C-Mod. ITBs can be routinely produced in C-Mod steady enhanced D_α (EDA) high-confinement (H-mode) plasmas by applying off-axis ion cyclotron range of frequencies (ICRF) heating ($|r/a| \geq 0.5$). They are observed primarily in the electron particle channel and are marked by the steepening of the density and pressure profiles.

ITB formation in C-Mod appears to be the result of competition between an inward particle pinch and the outward diffusion caused by various fine scale plasma instabilities. Several experiments were performed on C-Mod to verify whether ITB formation can be explained within a paradigm of marginal stability. Analyses of the temperature profiles reveal that the T_i profile widens and the T_e profile exhibits flattening in the ITB region when the ICRF resonance is moved off-axis. Transport and gyrokinetic stability analyses demonstrate that reduction of the temperature gradient suppresses the temperature gradient driven instabilities. Nonlinear gyrokinetic simulations of plasma microturbulence show that this results in a significant reduction of the outward diffusion, and allows the inward particle pinch to dominate, peaking the density profile.

Thesis Supervisor: Catherine Fiore
Title: Research Scientist, Plasma Science and Fusion Center

Thesis Reader: Ian Hutchinson
Title: Professor of Nuclear Science and Engineering, Department Head

Thesis Reader: Darin Ernst
Title: Research Scientist, Plasma Science and Fusion Center

Acknowledgements

Now, as I prepare to leave MIT after spending so many years here, I feel nostalgia. This thesis research would not be possible without all the great people I've met at and beyond the PSFC. I am glad that I can take my time now to thank them. At this moment, I can completely appreciate the importance of the acknowledgement section in the thesis.

First and foremost, I am in great debt to Dr. Catherine Fiore, my supervisor. She has been very helpful and encouraging, patient but persistent. She has always been available to answer my numerous questions and open for discussions. It was her wise guidance that helped plan my thesis work and steered it in the right direction. She helped me see the big picture and the light at the end of the tunnel.

Many thanks go to Dr. Darin Ernst, the reader of this thesis. He spent many hours teaching me to how to use the GS2 code, discussing the results, and answering my innumerable and sometimes silly questions. If it were not for Darin, profiles fitting software would never have seen the light of day.

I would like to thank Prof. Ian Hutchinson for the financial support he secured for me when he was the head of the Alcator project and for being the reader of this thesis. He gave me criticism when I deserved it and I saw it as a challenge and my professional duty not to let him down. Only now do I understand how wise some of his pieces of advice or decisions were. I constantly felt his presence and support behind the scene, which stimulated my work.

I have to thank Dr. Dmitri Mossessian, who was my thesis supervisor for almost three years. It was his energy and dedication that made Thomson scattering upgrade a success. I learned a lot about laboratory techniques and work ethics from him.

I would like to thank Prof. Ron Parker and Prof. Jeff Freidberg for sitting on my thesis committee. I am also in debt to them for their personal advice and words of wisdom when I needed it.

Dr. Earl Marmar, as the head of Alcator, provided financial support not only for my thesis research but also for the undergraduate students who worked to help me upgrade profiles fitting software.

Throughout the thesis I relied heavily on discussions with many colleagues, in particular with John Rice, Paul Bonoli, Martin Greenwald, Amanda Hubbard, David Mikkelsen, and Jim Irby. Their valuable comments significantly improved my various presentations and papers, including this thesis. I am thankful to Steve Wolfe for his help running kinetic EFIT.

I am grateful to many engineers and technicians who helped me with various hardware, software, and electronics issues at different times of my thesis project. Edgar Rollins was of great help at the early stage of building the core TS system. Tom Toland provided his expertise and help on numerous vacuum-related matters during my entire time at MIT. I would like to thank Jim Irby, Ed Fitzgerald, Gary Dekow, and Rui Vieira for their advice on engineering issues. Much hardware support came from Joe Bosco, Yuri Rokhman, and Bill Burke. Josh Stillerman and Tom Fredian were always there when software-related help was needed. I am thankful to Bill Parkin and Dave Bellofatto for their often sought and much needed help with solving various electronics problems. Finally, I want to express my appreciation to Jerry Hughes, with whom I worked hand in hand in the TS group for six years.

I would like to thank Doug McCune and Rob Andre for the time they spent helping to get my TRANSP runs to work.

I acknowledge the contribution of MIT undergraduate students, Eric Grebing and David Ely, to the development of the graphical user interface for the profiles fitting routines. David really made this project come to life.

I also am grateful for the support of the Alcator HQ administrative staff: Valerie Censabella, Megan Tabak, Corrinne Fogg, Dragana Zubcevic, and Jessica Coco.

I have benefited from being in the company of fellow students, some of whom have moved on: Ken Marr, Greg Wallace, John Liptac, Vincent Tang, Howard Yuh, Ishtak Karim, Jennifer Ellsworth. Alex Ince-Cushman, Matt Reinke, Rachael McDermott, Sanjay Gangadhara, Brock Bose, Arturo Dominguez, Eric Edlung, Liang Lin, Natalia Krasheninnikova, Eugenia Smirnova, Andrey Simakov, Chris Boswell, Alex Mazurenko, Bo Bai, Vadim Roytershtein, Tim Graves, Marco Ferrara, Noah Smick, Xenia Samokhvalova, Alexey Kuznetsov, Eric Nelson-Melby, Davis Lee, Jinseok Ko, Dave Schmittdiel, Alex Parisot, and Eugenio Ortiz.

Extracurricular activities helped me free my mind and release stress. I thank the entire Alcator softball team for teaching me this wonderful sport and giving me a chance to play. I particularly want to recognize the team leaders who embodied team spirit: Bill Parkin and Valerie Censabella. I will never forget Bob Granetz who introduced me into scuba diving. He is the most skillful underwater navigator and 'lobstah divah' I have ever seen. I would like to thank my friends with whom I shared trips to Maine, New Hampshire, and New York, and MIT soccer club 'footie'.

I am grateful to Paul Rivenberg and Mary Pat McNally for their help in organizing the PSFC Student Alumni Club and the setting up a website for that.

I say many thanks to my mom Svetlana and brother Maxim Zhurovich for their love and support. My mom always wanted me to become a scientist and come to the US. So, her dream came true and I know she is very proud.

Finally, I thank my long time girlfriend Lena Kadeykina for being by my side all these years. Lena gave me her love, encouragement, and support when I needed it. She even stayed long hours at the PSFC helping me do the calibrations and handle some TS components. I doubt that I would be able to endure the stress and perils of graduate student life without her.

Contents

List of Figures

List of Tables

Chapter 1

1 Introduction

It has been debated in recent history whether there is enough fuel in nature to keep up with the energy needs of mankind. All projections of future energy consumption and estimates of natural fuel resources suggest that we need to develop sources of energy alterative to fossil fuels. Fusion energy is one of the most promising concepts in this direction.

1.1 Plasma fusion

Nuclear fusion energy is released in a process of combining (fusing) light nuclei. The most suitable reactions for this are

$$D + D \rightarrow T + p + 4.03\,MeV$$

$$D + D \rightarrow {}^{3}He + n + 3.27\,MeV$$

$$D + T \rightarrow {}^{4}He + n + 17.6\,MeV$$

$$D + {}^{3}He \rightarrow {}^{4}He + n + 18.3\,MeV \qquad (1.1)$$

where D and T represent nuclei of deuterium (^{2}H) and tritium (^{3}H) respectively. The amount of energy released depends on the fusion rate, which for D-T reaction is given by

$$R_f = n_D n_T < \sigma v > \qquad (1.2)$$

where $<\sigma v>$ is the reaction cross-section averaged over the Maxwellian velocity distribution

$$f(\mathrm{v}) = n\left(\frac{m}{2\pi T}\right)^{3/2} \exp\left(-\frac{m\mathrm{v}^2}{2T}\right) \tag{1.3}$$

of each species with mass *m*, density *n*, and temperature T. The reaction cross-section is energy dependent, and in order to achieve fusion-relevant temperatures, heating of the nuclear fuel is required. At these temperatures deuterium and tritium gas is ionized and exists in the form of plasma.

Plasma is a fourth state of matter, where ions are stripped of electrons and they coexist together as freely moving particles. Plasma possesses several important qualities, one of which is quasineutrality. For a pure deuterium plasma, it means that $n_e \approx n_D$ and for multiple ionic species *i* with charge Z_i it takes form

$$n_e \approx \sum_i n_i Z_i \tag{1.4}$$

Quasineutrality helps define the effective plasma charge as

$$Z_{eff} = \frac{\sum_i n_i Z_i^2}{n_e} \tag{1.5}$$

The effective plasma charge equals 1 for a singly charged ion plasma and $Z_{eff} > 1$ indicates the presence of impurities. Quasineutrality also means that there is a strong Coulomb force that arises if there is a charge separation. This force results in a natural frequency of the plasma, which is given by:

$$\omega_p = \left(\frac{ne^2}{\varepsilon_0 m_e}\right)^{1/2} \tag{1.6}$$

This is the frequency at which a displaced group of electrons will oscillate in space.

1.2 Confinement and transport

It is necessary to keep hot plasma away form the walls of the containment vessel, to prevent damage to the containment and to prevent cooling and contamination of the plasma. Since plasma consists of a group of charged particles it is natural to confine it by applying a magnetic field. Charged particles can travel freely along the magnetic field line, but they experience a Lorentz force if they have a velocity in a perpendicular direction. This force is given by

$$\mathbf{F} = e\mathbf{v} \times \mathbf{B} \tag{1.7}$$

and is perpendicular to both the particle velocity and the magnetic field. It causes a particle to rotate around the magnetic field line at its cyclotron frequency,

$$\omega_c = \Omega = \frac{eB}{m} \tag{1.8}$$

and with a gyro-, or Larmor radius

$$\rho = \frac{\mathrm{v}_\perp}{\omega_c} = \frac{m\mathrm{v}_\perp}{eB} \tag{1.9}$$

In order to eliminate end losses, magnetic field lines are wrapped to form a torus and close on themselves. This is the basis of a highly successful design of magnetic fusion device, a tokamak. Fig. 1-1 shows a quarter of a typical tokamak plasma with a major radius R_0, a minor radius a, and a circular cross-section. Radius r, poloidal (θ) and toroidal (Φ) angles define the toroidal geometry. A strong toroidal magnetic field B_T (or B_ϕ) is applied externally, while the poloidal magnetic field B_θ is generated by the plasma current I_p, which is driven by induction from a central transformer. The combination of toroidal and poloidal fields results in a total magnetic field that has a helical form around the torus. Associated with the pitch of the magnetic field is the safety factor q, which

equals the number of toroidal turns the field line must undertake in order to return to the same poloidal position. For a circular plasma and a large aspect ratio R_0/a it can be approximated as

$$q = \frac{rB_T}{RB_\theta} \tag{1.10}$$

Generally, q is of order 1 near the plasma center and increases towards the edge.

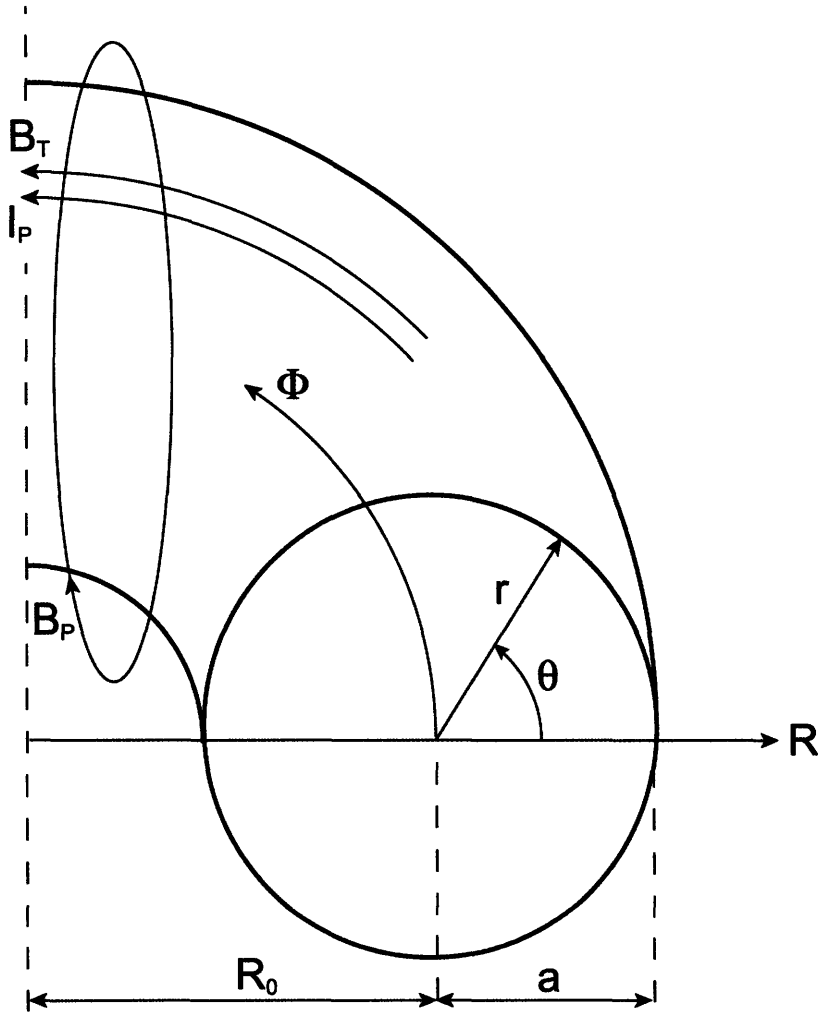

Figure 1-1: Typical toroidal plasma geometry with a major radius R_0 and a minor radius *a*. The toroidal magnetic field B_T is applied externally, while poloidal magnetic field B_θ is generated by the plasma current I_P.

Since present day tokamaks usually operate with a non-circular cross-section, the poloidal flux function ψ is introduced. The tokamak plasma is symmetric in Φ, and in any poloidal cross-section it consists of an infinite number of nested surfaces of constant ψ. The magnetic field lines lie on these surfaces. Since parallel heat transport is very large, the temperature can be considered constant on a flux surface, or to be a flux function. Due to force balance considerations, there is no parallel pressure gradient, which means that pressure and density, are flux functions as well.

In a toroidal geometry, the gradients of the magnetic field lead to a vertical displacement of the guiding centers of each particle species from their nominal flux surfaces. This toroidal drift can be written as [1, Ch. 2.6]

$$\mathbf{v}_d = \frac{\mathrm{v}_{\|}^2 + \mathrm{v}_{\perp}^2/2}{\Omega B^2}\mathbf{B}\times\nabla B. \tag{1.11}$$

Because of the twist in the magnetic field lines created by the combination of the two magnetic fields, the particles spend time both and above and below the magnetic axis allowing this drift to cancel. Another important drift arises when an electric field is perpendicular to the ambient magnetic field. This is called $\boldsymbol{E}\times\boldsymbol{B}$ drift and is given by

$$\mathbf{v}_d = \frac{\mathbf{E}\times\mathbf{B}}{B^2} \tag{1.12}$$

Local changes in the electric field can result in a radial plasma flow, which is usually associated with enhanced transport. In some cases they can generate sheared poloidal flows which break turbulent eddies and reduce radial transport, thus improving confinement. It will be shown later what role these drifts play for instabilities that can occur in tokamak plasmas.

Plasmas in tokamaks are often characterized by the energy confinement time, τ_E, which defines the loss rate of energy contained in the plasma. If W_p is the plasma stored kinetic energy, and P_{in} and P_{out} are the input and loss power, then

$$\frac{dW_p}{dt} = P_{in} - P_{out} = P_{in} - \frac{W_p}{\tau_E} \tag{1.13}$$

and in steady-state,

$$\tau_E = \frac{W_p}{P_{in}} \tag{1.14}$$

Input power comes from the alpha-particle heating from fusion reactions, ohmic heating from the plasma current and also from auxiliary heating by microwaves and neutral beams.

The energy confinement time is a convenient description of global confinement properties, but it conceals details of transport mechanisms such as diffusion, convection, and radiation. An extensive theory of *neoclassical transport* has been developed to account for these issues. However, experiments demonstrate that the observed particle and energy transport in present tokamaks usually exceeds the predictions of the neoclassical theory. This transport is believed to be governed by various plasma instabilities of different scales and is called *anomalous*.

There are certain regimes of plasma operation, when plasma confinement is significantly improved because the so-called *transport barriers* develop. These barriers are regions where particle and/or energy transport is significantly reduced. Neoclassical levels of transport can be achieved inside these barriers. Edge transport barriers form at the edge of the plasma and result in high confinement, or H-mode, regime. Under certain conditions similar barriers form inside the plasma and are termed internal transport

barriers (ITBs). The formation of the transport barriers has been associated with the suppression of the plasma instabilities.

1.3 Alcator C-Mod

This thesis presents the results of the research done on a tokamak called Alcator C-Mod. [2] This machine is located at the Plasma Science and Fusion Center at Massachusetts Institute of Technology.

1.3.1 Plasma parameters and geometry

Alcator C-Mod is a compact tokamak with $R_0 = 0.68$ m and $a = 0.22$ m. Most operation is at 5.4 T, which is where the auxiliary radio frequency can be used to resonantly heat hydrogen minority ions near the plasma center. The magnetic field can vary from 2.6 T to 8.1 T, however. Typical current through the plasma is in the range of 0.6 - 1.5 MA. High central densities in the range of 1-5 $x10^{20}$ m^{-3} can be achieved because of the high field and compact machine design. The central temperature is usually 1-4 keV. The high densities and high magnetic field make this machine very relevant to future tokamak reactors. To date Alcator C-Mod has employed ion cyclotron range of frequencies (ICRF) heating as the only auxiliary heating system [3, 4], although lower hybrid heating is becoming available.

Figure 1-2 shows a cross-section of the C-Mod tokamak. The C-Mod plasma is typically D-shaped, meaning that last closed flux surface (LCFS), or separatrix, forms an x-point, or null, and the chamber walls are in contact only with open field lines. All

discharges analyzed in this thesis have the lower single null configuration. The plasma facing components consist of molybdenum tiles, which are usually coated with boron shortly before ITB-related experiments.

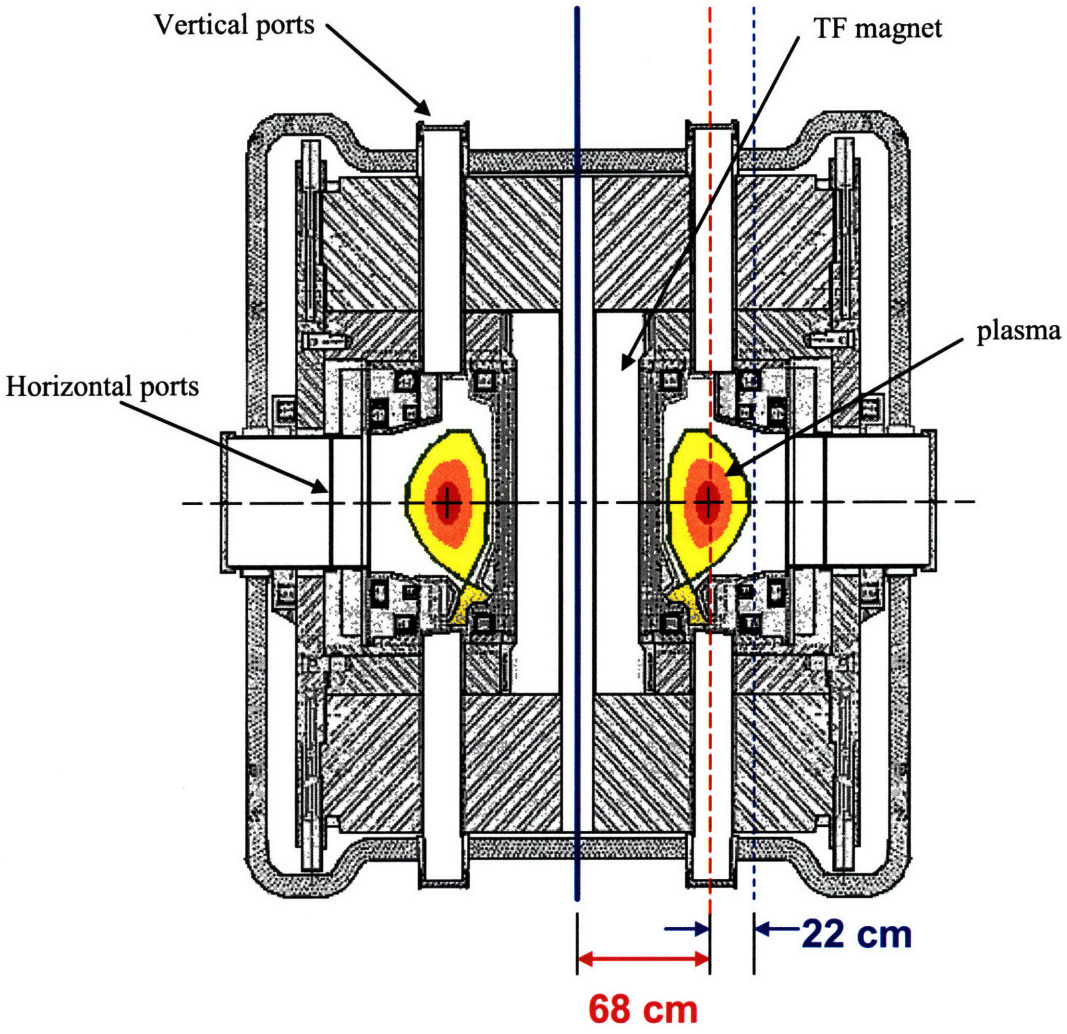

Figure 1-2: Cross-section of Alcator C-Mod. A typically shaped plasma is pictured.

1.3.2 Operational regimes

All discharges analyzed in this thesis developed enhanced D_α (EDA) H-mode. [5, 6] The name takes its origin from the increased level of the Balmer alpha line from

deuterium (D_α) compared to the levels of other H-mode phases such as ELM-free (edge localized modes). This plasma regime requires auxiliary heating to reach H-mode and therefore, ICRF D(H) minority heating is used. The L-H transition is induced by the application of the ICRF power above a certain threshold and the EDA H-mode develops over ~100 ms after that. Typically it can be maintained in steady state until the ICRF power is shut off.

The core of this thesis research concerns the formation of internal transport barriers (ITBs), which can be routinely produced in C-Mod steady EDA H-mode plasmas by applying off-axis ($|r/a| \geq 0.5$) ICRF heating on either the high or low field side of the magnetic axis. ITBs were first observed on the Alcator C tokamak with the injection of frozen hydrogen pellets. [7] Internal transport barriers in tokamak plasmas are characterized by the reduction of transport in one or more of the particle, momentum, or energy channels in the core plasma region. On C-Mod they are observed primarily in the electron particle channel and are marked by the steepening of the density and pressure profile following the L-H transition. The fact that the central temperature does not decrease as the density rises is evidence that a thermal barrier exists as well.

1.3.3 Thomson scattering and other diagnostics

In order to study the physics of the internal transport barriers, reliable measurements of density and temperature profiles in the core plasma region are required. This is done mainly by the core Thomson scattering (TS) system, a major component of which is the upgrade that was installed on C-Mod in 2002. [8, 9, 10, 11] The system takes measurements along the laser beam coming through the vertical port of the tokamak

and uses EFIT [12] magnetic reconstruction results to map derived plasma densities and temperatures onto the midplane along the poloidal flux surfaces. At this point the TS diagnostic utilizes 2 lasers each operating at 30 Hz. The pulse trains are evenly staggered to provide 60 Hz measurements of plasma density and temperature profiles. However, a relative time shift between the laser pulses can be introduced to study transient plasma phenomena. At present the core TS system has 11 spatial channels with positions optimized to provide ~1 cm resolution in the region of the ITB. Currently another upgrade is being undertaken to improve the spatial resolution of the core TS diagnostic even further. The working description of the system, and the results obtained from it, are the subject of the subsequent chapters.

Electron cyclotron emission

The electron temperature (T_e) on C-Mod is also measured using a variety of electron cyclotron emission (ECE) diagnostics. These include two grating polychromator (GPC) systems, one with 9 and the other with 18 spatial channels [13, 14], and a heterodyne 32-channel ECE system [15]. They provide good spatial coverage with high temporal resolution (< 1 ms) and complement TS measurements in most cases. However, the ECE signal is subject to cutoff at high plasma densities. Therefore, these systems often lose signal in the region of interest during the ITB operation.

Visible Brehmsstrahlung

Data are also available from a visible brehmsstrahlung (VB), or visible continuum array, which measures line-integrated emissivity at 536 nm along tangential chords at the

midplane. [16] In the core plasma the emissivity is dominated by the free-free bremsstrahlung and its intensity has a weak temperature dependence. T_e is obtained from TS or ECE measurements. After the emissivity profiles are corrected for the plasma temperature, the resultant high resolution $n_e\sqrt{Z_{eff}}$ profiles are obtained using an Abel inversion technique [17, Ch. 4.4]. These measurements can serve as a proxy for the density profiles as well as provide $Z_{eff}(R)$ calculations when used in combination with TS density measurements.

X-ray diagnostic

A limited amount of ion temperature (T_i) profile and plasma rotation data is obtained from a scannable array of five high spectral resolution x-ray spectrometers (HIREX) [18]. A small amount od argon is puffed into the plasma and spectra from Ar emission are typically collected every 50-100 ms during plasma discharges. Broadening of the Ar lines determines the Ar temperature, which is assumed to be equal to the temperature of the major ion species. The Doppler shift of these lines determines the plasma rotation velocity.

Neutron rate

The total neutron flux is measured using two different systems. The first one consists of 18 neutron detectors, has 1 msec time resolution, and is absolutely calibrated with Cf^{252} and D-D fusion neutrons from Alcator C-Mod [19]. The second detector system provides fast measurements of the total neutron production with 0.1 msec time resolution and is cross-calibrated with the first system. The measured neutron rate, due to

its high sensitivity to the ion temperature, enables us to determine the central value of the ion temperature when density profiles are available.

1.4 Thesis goal and outline

The goal of this thesis is to contribute to the understanding and to provide a systematic analysis of the formation mechanisms of internal transport barriers in ICRF heated C-Mod plasmas. During the thesis work, several experiments were successfully performed on Alcator C-Mod that helped experimentally verify certain trends. Further transport simulations and stability analysis helped identify and verify key ingredients of ITB formation and suggested further conditions that might play an important role. The central experimental part of the thesis work was installation and calibration of the core TS upgrade, and this thesis describes the implementation of this system for the research on ITB formation.

The presentation of the thesis studies is organized as follows:

- Chapter 2 provides detailed description of the experimental studies of ITB formation on other tokamaks. Prior results from C-Mod are also included.
- Chapter 3 introduces the theory of Thomson scattering and describes the core TS upgrade installed on C-Mod with conjunction to this thesis research. A series of required calibration procedures are outlined. More emphasis is put on a new method of absolute calibration of TS systems that was developed for this thesis work.
- Chapter 4 provides basic insight into the physics of microturbulent drift instabilities. Their relevance to C-Mod plasmas is also discussed.

- Chapter 5 describes the experiments performed on C-Mod that was designed to study the formation mechanisms of ITBs in ICRF heated discharges.
- Chapter 6 covers the transport analysis and simulations done with the TRANSP code. Introduction to the density and temperature profiles fitting software is also presented in this section.
- Chapter 7 presents the results of the gyrokinetic stability analysis done with the GS2 code. A brief introduction into the geometry and model equations of the GS2 code is provided. Simulation results of the dependence of the microturbulent instability growth rates on certain plasma parameters are presented.
- Chapter 8 summarizes the results of the thesis and provides suggestions for further research.

References for Chapter 1

[1] J. A. Wesson, *Tokamaks* (Oxford University Press, New York, NY, 1997).
[2] I. H. Hutchinson *et al.*, Phys. Plasmas **1**, 1511 (1994).
[3] Y. Takase *et al.*, *14th Symp. on Fusion Engineering,* San Diego, 1992 (IEEE, Piscataway, NJ, 1992), p. 118.
[4] G. Schilling *et al.*, *13th Topical Conf. on Radio Frequency Power in Plasmas*, Annapolis, 1999 (Melville, NY: AIP), Vol. 485, p. 429.
[5] Y. Takase *et al.*, Phys. Plasmas **4**, 1647 (1997).
[6] M. Greenwald *et al.*, Phys. Plasmas **6**, 1943 (1999).
[7] M. J. Greenwald *et al.*, Phys. Rev. Lett. **53**, 352 (1984).
[8] R. Watterson and K. Chen, Rev. Sci. Instrum. **61**, 2867 (1990).
[9] D. A. Mossessian, A. Hubbard, and J. Irby, Rev. Sci. Instrum. **70**, 759 (1999).
[10] J. W. Hughes *et al.*, Rev. Sci. Instrum. **74**, 1667 (2003).
[11] N. P. Basse *et al.*, "Diagnostics Systems on Alcator C-Mod," Fusion Sci. Technol. **51**, 476 (2007).
[12] L. Lao, H. John, R. Stambaugh, A. Kellman, and W. Pfeiffer, Nucl. Fusion **25**, 1611 (1985).
[13] P. J. O'Shea,A. E. Hubbard, and Alcator C-Mod group, *Proc. 9th Joint Workshop on ECE and ECH, Borrero Sprongs,* CA, January 23-26, 1995 (World Scientific, New Jersey, 1995), pp. 393-401.
[14] G. Taylor *et al.*, *Bull. Am. Phys. Soc.* **43**, 1821 (1998).
[15] J. W. Heard *et al.*, Rev. Sci. Instrum. **70**, 1011 (1999).
[16] E. S. Marmar *et al.*, Rev. Sci. Instrum. **72**, 940 (2001).
[17] I. H. Hutchinson, *Principles of Plasma Diagnostics*, Cambridge University Press, Cambridge, second edition, 2002.
[18] J. E. Rice and E. S. Marmar, Rev Sci. Instrum. **66**, 752 (1995).
[19] C. L. Fiore and R. L. Boivin, Rev Sci. Instrum. **66**, 045 (1995).

Chapter 2

2 Internal transport barriers

2.1 Definition and properties

Tokamak operation in enhanced confinement regimes with internal transport barriers (ITB) is attractive as it represents an important step towards the approach of ignition conditions. The ITBs are the regions of significantly reduced transport in one or more of the thermal, particle, or momentum channels for either the ions or the electrons, so that the region of improved confinement is formed inside. Moreover, a bootstrap current is generated as a consequence of the pressure gradient formed by the ITB, which is desirable for steady-state tokamak operation, and especially for advanced tokamak studies. Peaked density and temperature profiles also provide better fusion yield and ITBs are considered as one of the ITER hybrid scenarios. Even though early observation of a particle transport barrier with improved energy confinement was found on Alcator C in 1983 [1], ITB physics is still not well understood.

This chapter is a review of recent studies of ITBs on different machines. There are numbers of scenarios for each machine, which lead to ITB formation. There is a paradigm that ITB formation seems to have certain common physics, i.e. that microturbulent transport, which is likely due to ion temperature gradient driven modes, is stabilized by reversed magnetic shear, ExB flows or profile change. However, the ITB properties are very individual, not only for different tokamaks, but also for each particular scenario in a given machine. For this reason we will carefully describe all ITB

scenarios one by one. For each scenario being described some specific important issues will be addressed: the recipe for obtaining ITBs, the evolution of ITB discharges, the modes observed and their role in ITB evolution and termination, the transport analysis, the conditions for ITB triggering and location, and ITB sustainment and control.

For more comprehensive reviews of the ITB-related studies the author would recommend papers by Synakowski [2], Wolf [3], and the author's favorite by Connor *et al.* [4].

2.2 Experimental results from other tokamaks

2.2.1 JT-60U

Most of the ITBs on JT-60U are obtained in reversed shear (RS) discharges, where the magnetic shear $s = (r/q)dq/dr$ is the rate of change of the magnetic field pitch, denoted here by q, with respect to minor radius. The reversed magnetic shear configuration is established with neutral beam (NB) injection during the ramp phase of plasma current. This is known be an effective procedure to create a wide negative shear region. [5, 6]

One of the RS ITB scenarios on JT-60U is the predominately ion heated H-mode plasma. [7] For this type of discharge, 2 tangential NB injectors are used and the NB powers for co-direction and counter-direction (with respect to the direction of plasma current I_P) are kept nearly balanced in order to exclude the effect of external momentum. At the beginning of the main heating pulse, the plasma experiences transition into ELMy (edge localized modes) H-mode phase. These ELMs help to keep the edge density constant while the central density continues to rise, so that a peaked density (and

temperature) profile is formed. The electron density and temperature peaking starts with the ELMs and continues to rise until the discharge termination. Steep n_e and T_e gradients, which are associated with the ITB formation, are formed at $\rho = 0.51\text{-}0.62$ (ρ is the normalized minor radius). The ion temperature T_i is 30-45% higher than the electron temperature T_e because of the predominant ion heating by the neutral beams.

The observed n_e and T_e gradients in the ITB region are much larger (up to 20 times) than those outside the ITB. Also the gradients are larger for T_e, while the T_i gradient changes more smoothly. Inside the ITB the electron density profile is flat and the T_e and T_i gradients are small. The q reaches its minimum value of 3.6 at $\rho = 0.67$ and the magnetic shear is negative inside it. It can be concluded that the ITB lies in the negative shear region and the position of its outer edge is very close to the position of q_{min}. Overall the ITB extends beyond 60% of the plasma minor radius, which means that a large plasma volume has improved confinement. A bootstrap current fraction of up to 80% of the total plasma current is achieved under this scenario. [8] This is a quite promising result for advanced tokamak operation.

Transport analysis performed for this type of discharge reveals that the electron effective thermal diffusivity (convective loss is included), χ_e^{eff}, drops sharply by a factor of 20 within 5 cm around $\rho = 0.62$ and reaches value of 0.2-0.3 m^2/s. This drop occurs at the position of a large change of T_e gradient. On the other hand, χ_i^{eff} gradually decreases from the edge to the half radius and in the inner region reaches a value of 0.4-0.8 m^2/s, which is significantly smaller than the neoclassical prediction. Similar discrepancy in TFTR RS discharges was attributed to the violation of neoclassical theory, thermal pinch or anomalous ion-electron thermal equilibration [5].

In this scenario, high confinement of reversed shear discharges on JT-60U is terminated by a collapse caused by an ideal MHD instability with low n modes dominant.

Some ITB experiments for ion heated RS with an L-mode edge were carried out on JT-60U. [9] In these experiments the formation of strong ITBs in the positive shear zone of RS plasmas from the weak ITB in the RS zone is observed as a series of separate ITB events. [9, 10] These ITB events are abrupt in time and wide in spatial variations of heat diffusivity, observed as the simultaneous rise and decay of the electron temperature T_e in two plasma zones. The remarkable feature of these discharges is that the spatial zone of the heat diffusivity reduction first appears in the negative shear zone, but then shifts outside and settles in the positive shear zone. This results in a bigger plasma volume with improved confinement with a slight degradation of transport inside the position of q_{min}. Under this scenario ITBs are observed primarily in electron and ion temperature channels.

Temperature variations during the ITB events are measured by ECE diagnostics and the observed evolution of heat fronts can be used in heat pulse propagation (HPP) studies. Transport analysis based on HPP finds values of the electron dynamic heat diffusivity as low as ~0.1 m^2s^{-1} in the region with ~8 cm width. Similarly, low values of the ion dynamic heat diffusivity (~0.14 m^2s^{-1}) are found, which are close to the neoclassical values (0.1 m^2s^{-1} in this case). However, the relation between the dynamic heat diffusivity and that obtained from power balance is still unclear.

ITBs are also investigated in JT-60U electron-heated discharges. It is theoretically expected that $T_e/T_i > 1$ is a destabilizing factor to the ion temperature

gradient (ITG) micro-instabilities, which are believed to be responsible for the confinement degradation. Since in ITER plasmas $T_e > T_i$ due to predominant electron heating by α particles, the goal of these experiments was to investigate if the ITB would remain under a condition of $T_e > T_i$. [11]

In these experiments the desired temperature balance is achieved by central electron cyclotron range of frequencies (ECRF) heating. The plasma is started up initially with the standard scenario with positive–ion based NB (P-NBI) injection during the current ramp-up phase to form the RS configuration with an ITB. After RS and ITB are formed the heating power is switched from P-NBI to a combination of ECRF and negative–ion based NB (N-NBI) injection. As a result, the fractional power to the electrons rises from about 30% to about 55% of the total absorbed power and finally T_e exceeds T_i. These electron heated ITBs are compatible with both H- and L-mode edge. ITBs are clearly seen in n_e, T_e and T_i channels with the foot being located near $\rho \sim 0.6$, the location of q_{min}. Results show that good confinement (H-factor is 1.5 for H-mode and 2.9 for L-mode) can be maintained in strong negative magnetic shear plasma with dominant electron heating.

As far as the termination is concerned, it is reported that RS plasmas with strong ITBs on JT-60U often disrupt, especially when the minimum q is passing through 2. In order to avoid such a collapse and sustain a RS configuration with ITB, two approaches have been demonstrated. One uses current profile control and the other involves heating scenario optimization to achieve steady-state with high bootstrap fraction. [12] As a result, the maximum achieved H-factor for the RS discharges with ITBs is 3.4 and the density reaches up to ~70% of the Greenwald density limit n_G [13].

In order to investigate detailed features of ITB characteristics under the $T_e > T_i$ condition, ECRF heating experiments on positive shear ITB plasmas with L-mode edge were carried out on JT-60U. [11] The existence of an ITB at $\rho \sim 0.55$ was observed from temperature radial profiles. The formation of the ITB was accompanied by the existence of a distinctive notch structure in the toroidal velocity V_t profile. The V_t profile becomes negative at the ITB foot, suggesting that the velocity shear might play an important role in triggering ITBs in JT-60U plasmas. [14] After the ECRF injection, flattening of V_t was observed. Calculation of the χ_i profile by power balance also showed that a jump in the χ_i profile at the ITB location was also smoothed with the ECRF injection, which again indicates weakening of the ITB. In these experiments, after the ECRF turn-off, the ITB structure reappeared and V_t notch structure recurred. Finally, from these observations it can be concluded that the ITB cannot be sustained on JT-60U in normal shear electron heated plasmas, which is in contrast to the RS case.

2.2.2 ASDEX Upgrade

On ASDEX Upgrade there are two scenarios that have been found to be most promising for stationary operation and enhanced performance.

The first scenario is a stationary ITB discharge in combination with an H-mode edge and flat q profile with $q(0) \approx 1$. [15, 16] During the current ramp phase of such a discharge, a moderate NB heating of 2.5 MW is applied to reduce current diffusion. After the current flat top is reached and the X-point is formed, the NBI power is increased up to 5 MW, the L-H transition occurs, and the line averaged density is kept at 4×10^{19} m^{-3} ($\approx$0.3 Greenwald density n_G). T_i reaches almost twice the value of T_e since

75% of the power goes to the ions. The profiles of plasma temperature, density and toroidal rotation velocity show the formation of an ITB at $\rho = 0.6$ with a strong density peaking of 1.5, which means that not only energy confinement but also the particle confinement is improved.

Energy transport analysis shows that in the central region of the plasma χ_i drops to the neoclassical value, while χ_e is also low, indicating that the transport reduction is not limited to the ions. Transport simulations also reveal that a combination of the magnetic shear stabilization with E×B shearing rate, $\omega_{E\times B}$, is required to explain such a reduction of thermal diffusion coefficients. [17] They found that the E×B shearing rate is above the linear turbulence growth rates for $\rho < 0.5$, and even in the rest of the plasma, a strong reduction of χ is calculated due to flow shear stabilization. [15]

Though there are some similarities between this and RS JT-60U scenarios, the different q profile seems to play an important role in the ITB evolution. In the scenario discussed, the only MHD activities observed in the core of the plasma are strong (1, 1) fishbones. They behave like a resistive MHD instability similar to sawteeth, but on a much faster scale of ~1 ms. These drive magnetic reconnections and could serve as a mechanism for stationary clamping of the q profile with $s \approx 0$ in the core and $q_0 \approx 1$ even in the absence of sawteeth. [16, 18, 19]

Furthermore, no temporal accumulation of impurities in the center is observed. This stationarity is probably caused by both the strong fishbone activity expelling impurities from the plasma core and by ELM activity at the edge. In such discharges a confinement improvement of $H_{ITERL\text{-}89P}=2.4$ or $H_{ITERLH\text{-}92P}=1.4$ and $\beta_N=2$ are achieved

and maintained for 6 s (40 confinement times), only limited by the duration of the pulse length.

For the sustainment of the ITB the heating power during the current ramp was found to be very critical. Applying more NBI power during the current ramp resulted in a large-scale MHD instability right after the L-H transition. Discharges without preheating in the current ramp-up phase showed only transient improvement of the plasma confinement, indicating that the current profile so obtained cannot stabilize the larger pressure gradients. A (3, 2) neoclassical tearing mode leads to a deterioration of the confinement and finally to (2, 1) locked modes.

Attempts to raise the density by gas fuelling at a constant heating power also resulted in deterioration of confinement, accompanied by a reduction of the density peaking and the appearance of sawteeth when T_i approaches T_c. Together with the ITB the high performance in terms of H-factor and β_N is lost, but is restored as soon as the gas puff and density are reduced.

It was found that in such ITB discharges, the density can be increased up to almost half of the Greenwald density by gas puffing with a simultaneous power ramp. However, the threshold for the heating power to sustain the ITB increases when the density is increased in this way (by up to 50%). No confinement deterioration is observed in this case and β_N increases while the density peaking decreases only moderately. The ASDEX Upgrade team found that the improved confinement properties are related to the density peaking, in agreement with having transport that is caused by the ITG instability. Further density rise was again limited due to neoclassical tearing modes caused by β_N rising up to the stability limit at $\beta_N = 2.2$.

Going into the configuration with higher triangularity increases the stability limit of neoclassical tearing modes. [15, 18] The density can then be increased, while the core energy confinement increases only slightly (in contrast to a conventional H-mode). $H_{ITERL\text{-}89P}$=3.0 can be achieved mainly due to a density rise up to 0.45 n_G. An important conclusion is that the density increase caused by improved core particle confinement using plasma shapes with higher triangularity does not change the ITB onset conditions. It should also be noted that no temporal accumulation of light impurities is observed.

The second ITB scenario on ASDEX Upgrade is the discharge with reversed shear and $q_{min} \geq 2$. Such RS scenarios were only achieved transiently during the current ramp phase by applying 5 MW NBI, resulting in strongly reversed shear. [15, 19] These discharges have an L-mode edge due to the initial limiter phase.

Steep pressure gradients with central values of T_i = 15 keV and T_e = 5 keV are obtained with NBI heating, but due to both the smaller radius of the barrier and the L-mode edge, the performance is reduced with a confinement enhancement factor $H_{ITERL\text{-}89P}$=1.9 and β_N = 1.6. In the barrier region both electron and ion thermal diffusivities are close to the ion neoclassical values.

Though low (m, n) neoclassical tearing modes are avoided by the reversed shear and $q_{min} > 2$, strong MHD activity is observed in this scenario. This is because in the evolution of the very hollow q profile many resonant q surfaces for MHD modes are passed. These modes can cause severe energy loss as in the JT-60U RS scenario, but might help to achieve quasi-stationary advanced discharges by clamping the q profile. For example, ASDEX Upgrade results [15] show that short stationary phases are obtained

with q_{min} fixed at 3 and finally at 2, up to 200 ms, which is slightly longer than an energy confinement time. When q_{min} reaches 2, (2, 1) fishbones are often observed. These clamp the current profile by magnetic reconnection without global confinement losses, as do the (1, 1) fishbones described earlier. However, there also are (2, 1) continuous double-tearing modes that deteriorate the confinement and can at least transiently destroy the ITB.

While the current profile clamping mechanism facilitates the establishment of this scenario, active control by external current drive is demanded for steady-state operation with either flat or RS profiles. In order to investigate the response of the ITB to central electron cyclotron heating and current drive (ECCD), some experiments on ASDEX Upgrade using simultaneous strong central NBI and ECRF heating in ITB discharges with basic NBI heating were carried out. [15] These experiments show that ITBs are formed for both electrons and ions simultaneously and with counter-ECCD it is possible to reach $T_e \geq T_i$ operation similar to the RS electron heated JT-60U case. With the co-ECCD, the faster decaying central q profile leads to enhanced MHD activity of the (2, 1) mode and disappearance of the RS zone, resulting in a loss of the ITB. It should be noted that in the situation of counter-CD with ECRF, T_i and toroidal rotation do not decrease with respect to the case of pure NBI heating, which is in contradiction to the predictions of ITG models.

2.2.3 JET

There are several standard scenarios for obtaining ITBs on JET, most of which involve reverse or low magnetic shear.

In the first JET scenario, internal transport barriers are formed with low magnetic shear in the center, safety factor near the axis close to 2 and with an H-mode edge. [20, 21] This type of q profile is obtained with 1 MW of ICRF (H minority) preheating the center during the current ramp-up phase. High power using a combination of NBI and ICRF is applied towards the end of current ramp-up phase.

The ITB begins shortly after the main power is applied and is followed by an ELM free H-mode phase and then by a type I ELM phase. Just before the start of the H-mode phase the density profile is quite peaked. However during the ELM free period the edge density rises rapidly. Furthermore, the toroidal rotation at the edge also increases while the center of the plasma remains at a constant rotation velocity. This implies that both the density gradient and the toroidal rotation shear decrease strongly at the ITB location. This leads to a weakening of the ITB. During the type I ELM phase the ITB disappears completely. It can be concluded then that an ITB cannot be maintained in JET discharges with type I ELMs. This scenario is similar to JT-60U low shear discharges in terms of q profile, but in this case strong ELM activity at the edge destroys the confinement.

In order to sustain ITBs in JET, some experiments with edge and core control were done for this type of ITB scenario. [21] Experiments aimed at increasing the density have concentrated on deuterium gas fuelling in combination with argon puffing. Argon is used to reduce the edge pressure and the size of the ELMs (type III). Analysis shows, however, that the best steady ITB discharges are obtained without additional deuterium fuelling but with argon injection alone. Good confinement is obtained in these discharges with H_{97} = 1.2-1.6 at line averaged density of 30-40% n_G.

Also, pellet fuelling of ITB discharges has been studied as an alternative to gas fuelling. The observations, however, show that the pellet ablation leads to type I ELM activity and a collapse of the ITB, though the ITB can re-form when this ELM activity stops. [21]

Finally, it should be noted that the reported initial power required to form an ITB in the typical JET scenario with low magnetic shear is 18 MW. In this scenario ITBs are formed near the location of integer q surfaces (typically $q = 3$ or 2). [22] The triggering of the ITB is attributed to the coupling between an edge MHD mode, destabilized when q at the edge reaches an integer value, and the mode at a rational q surface inside the plasma. [23, 24] The internal mode is thought to enhance the E×B shearing rate locally, which again is believed to be one the key factors for turbulence stabilization, leading to an ITB inside of the integer q surface.

The second ITB scenario in JET uses a discharge with negative magnetic shear obtained by adding lower hybrid heating and current drive (LHCD). [24] This is usually achieved during the first several seconds of other discharges (preheat phase) with different main heating schemes.

Though it might seem that it is just another RS scenario, it turns out that the heating mechanism matters. The distinctive and very important feature of this scenario is that the internal transport barrier is produced only in the electron temperature. This ITB is produced at ~3.35 m ($\rho \sim 0.3$) soon after the application of LH power. The ITB is located in the negative magnetic shear zone with its outer edge close to the position of q_{min}. It should be noted that it is possible to control the radial position of the electron ITB

by changing the LH power, which changes the q profile. In particular, measurements from different shots show that the width of the ITB is proportional to the width of the region with large negative shear.

During the evolution of such a discharge the electron density profile remains flat (as was pointed out above). T_i reaches ~2-3 keV and remains smaller than T_e (up to 10 keV). In addition, the ECE measurements show sawtooth-like collapses on shots that exhibit T_e ITBs and a large negative magnetic shear, with no obvious precursor MHD modes.

Some conditions and limitations on ITB formation are found. [24] For example, T_e ITBs have been observed only for LH power above 1.3 MW. Moreover, the initial plasma current is also an issue: plasmas with a low initial current will not exhibit an ITB later during the LH heat phase. This could be explained by the fact that a fast current ramp results in an accumulation of current in the plasma periphery. Also, a higher current leads to a higher temperature, and hence a slower current diffusion. These two factors can produce a hollow current profile, which again is believed to favor ITB formation. However, a very high current rise can lead to MHD instabilities associated with excessive current in the periphery, resulting in a redistribution of the current and preventing the development of a hollow current profile.

In dedicated experiments, the preheat LH phase has been prolonged to 10 s. [25] The electron ITB survives for as long as the LH pulse, though the radius of the ITB shrinks with time. The ITB is always located in the negative shear region and its inward movement seems to be related to the evolution of the q profile.

In the third ITB scenario on JET, ITBs are obtained in plasmas with NBI and ICRF heating and negative magnetic shear. Unlike the plasmas with LH described previously, JET plasmas with NBI and ICRF power can produce internal barriers in the particle and ion energy transport simultaneously, in addition to the electron energy channel. These ITBs are seen as steep gradients of the T_e, T_i, n_e and V_t profiles.

The distinctive feature is that in such a scenario, two types of ITBs can be seen, often simultaneously. [22, 24] One of them is typically at a small major radius (< 3.5 m), and does not seem to be related to integer q surfaces. The second one is usually situated at a wider radius (up to 3.7 m), and is linked to integer q surfaces. It is reported that the triggering mechanism has not been identified yet, but in several cases, the ITBs appear when q_{min} reaches an integer value (again typically 2 or 3). [23, 24]

It has been observed that at a moderate level of NBI and ICRF power (additional power < 16 MW), plasmas with negative magnetic shear form ITBs more easily than plasmas with low but positive shear. [22, 24] Moreover, the additional power required to access very high performance is lower in the negative magnetic shear case.

In order to understand better the role of the q profile in the ITB triggering and termination, an ITB scenario with long NBI and ICRF power pulses has been developed in JET. This particular scenario is characterized by reproducible ITBs emerging at two times during the pulse. Soon after the start of the main heating phase the plasma forms an edge pedestal with associated ELMs, which remains until the end of the heating pulses. The ICRF and NBI powers do not change during the high additional power phase. The plasma density also remains constant, except during the ITBs where it peaks. The first ITB is triggered ~1 s after the start of the main heating phase. The temporal

analysis of the T_e profile shows the outward propagation of its foot. The study of the evolution of the q profile shows that this ITB terminates when the $q = 3$ surface reaches its foot and the ITB is destroyed by MHD activity related to a $q = 3$ surface. The second ITB is triggered when q_{min} reaches 2, and persists until the heating pulse ends.

Important progress has been made towards the steady state ITB scenario. [24] In discharges where the LH current fraction in the preheating phase is maximized, the q profile evolution is almost frozen. As a consequence, ITBs can be sustained for times of the order of the current diffusion time, and several times longer than the confinement time.

In the fourth JET ITB scenario using RS plasma configurations, both electron and ion ITBs have been obtained with full current drive by optimizing the coupling of the LHCD system. [26] Unlike the normal shear H-mode discharges, it was found that the plasma forms a pressure pedestal, corresponding to an H-mode, with small type III ELM activity during the high power NBI phase. [26, 27]

An electron ITB is triggered right at the beginning of the LH coupling. The ion ITB forms immediately after the injection of the NBI and ICRF. Both barriers disappear at the same time when the additional power is switched off. It must be stressed that the ITB is very resilient and is never lost despite minor temperature collapses observed in this type of discharges. The first type of collapse is connected to n=1 MHD activity and is often observed in such discharges. The second type of collapses is a radiative one, connected with the central effective charge $Z_{eff}(0)$ behavior. It should be noted that impurity accumulation is observed in these ITBs. The additional important point is that

the current density profile is possibly frozen in such discharges. An averaged electron density of up to 50% n_G is achieved. The electron barrier lasts about 37 and the ion barrier about 27 energy confinement times, of the order of the current diffusion time.

Analysis shows that the barrier location remains more or less fixed (at $R \approx 3.45$ m or $\rho \approx 0.5$) throughout the discharge, in spite of the strong temperature gradient variations connected to the minor temperature collapses mentioned above. The electron density profile is peaked, indicating the presence of a particle transport barrier. It is worthwhile to underline the fact that the barrier location is in the negative shear region. Also it can be noted that the q profile evolves during the discharge, but it remains always reversed, with the $q_{min} > 2$ and $s = 0$ positions more or less radially constant. However, it is not clamped at some integer numbers of q_{min} as in the JT-60U RS case.

Experimental evidence confirms the importance of a reversed q profile in such ITB scenarios. For instance, the electron barrier, in the early phase of the discharge, is present only when a strong negative magnetic shear is provided by the LHCD, and the ITB is suddenly lost when the current relaxes. [26] Moreover, transport analysis shows that there is a strong correlation between the region of good confinement and the region where the E×B shearing rate exceeds the linear ITG growth rate. Furthermore, the criterion $\rho^*_{Te} > 0.014$ ($\rho^*_{Te} = \rho_S/L_{Te}$, where ρ_S is the local Larmor radius at the thermal sound velocity and L_{Te} – electron temperature gradient scale length) was shown by a statistical analysis [28] to be a condition for the occurrence of an ITB in JET.

In order to achieve more stable operation in this ITB scenario a double feedback system has been implemented on the total plasma pressure and on the local temperature gradient by using, respectively, the NBI and ICRF systems. [26] In this case, the

temperature collapse, present in the previous configuration due to kink modes, is no longer present. Impurity accumulation also takes place during the ITB. However, some peculiarities must be stressed. In the previous case the ITB is so resilient that it survives the radiative collapse. In this case after a phase of impurity accumulation, a sudden expulsion of impurities from the plasma core occurs. This event is linked with several other observations: a small n=1 MHD activity, a reduction of the central plasma rotation, and a modification of the density profile. Nevertheless, the important fact remains that at later time the ITB is sustained, without any further sign of central impurity accumulation, as long as the heating power is sustained. It means that the central impurity accumulation problem can be kept under control, for example, by acting on the electron density profile.

2.2.4 DIII-D

In the DIII-D tokamak, as in many other cases we have described above, ITBs are often observed in the advanced tokamak scenario, when NBI heating is applied to low density discharges during the initial current ramp phase, leading to an RS profile [29].

The first ITB scenario [30], which is based upon the co-current NBI, starts with the conventional L-mode phase. A transition to the ELM-free H mode phase occurs shortly after the start of the main heating pulse, and finally the plasma undergoes the transition to the ELMy phase. It should be noted that the formation of the ITB, which is especially evident in the T_i and the rotation profiles, is already seen at $\rho \approx 0.45$ in the L mode phase. In the ELM-free phase, the ITB broadens considerably (to $\rho \approx 0.65$), with the edge transport barrier appearing in the T_e and n_e profiles at the same time. Finally, in the ELMy phase, the ITB weakens due to the continual rise of the plasma density. The

ion temperature is a factor of 2-3 above the electron temperature, similar to all other cases with predominant ion heating.

The transport analysis shows that, even in the L mode, the total ion diffusivity is reduced to the neoclassical value in the interior. In the ELM-free phase, the combination of the ITB and the edge transport barrier helps to reduce χ_i to the neoclassical level across the entire plasma. This is accomplished through the establishment of an overlapping edge barrier and ITB. During the ELMy phase the ion transport increases, remaining within roughly a factor of 2 above the neoclassical level over most of the plasma volume. On the other hand, the electron transport remains at the L-mode level in the plasma interior during the whole duration of the discharge, with some reduction seen in the H-mode edge region. This phenomenon may be related to the occurrence of high frequency drift modes, such as electron temperature gradient (ETG) turbulence, which would not respond to E×B shear stabilization. [31]

The microstability analysis of the transport profiles seems to support the paradigm of E×B shear suppression of ITG turbulence. Specifically, the calculated $\omega_{E\times B}$ shearing rate exceeds the maximum ITG growth rate, γ_{max}, in the interior of the plasma, which is where the ITB is observed in the L mode phase. In the ELM-free H-mode phase, $\omega_{E\times B}$ exceeds γ_{max} over the entire volume. What remains unknown is why the ion thermal transport increases by a factor of 2 in the ELMy phase even though $\omega_{E\times B}$ is still much larger than the maximum growth rate. There are some speculations, however, that fast ions could play a role in this case.

Good confinement performance is achieved in this type of discharge. $\beta_N \approx 3.7$, $H_{89} \approx 2.4$, and a bootstrap fraction of 0.5 can be maintained for up to 16 energy confinement times.

As far as sustainment is concerned, it is reported that such discharges are robust to ELMs and low-n kink modes, as well as to high-n ballooning modes. This is in contrast to the JET RS ELMy discharges without argon puffing. Tearing modes do not appear to play a role in these discharges either. The beta collapse at the end of the high performance phase is associated with a non-ideal resistive wall mode which becomes destabilized when β_N exceeds the no-wall ideal n =1 limit. A very low power threshold for ITB (< 2.5 MW) in this scenario should be noted. [31, 32]

Further studies on DIII-D have discovered a new confinement regime in counter-NBI discharges, in contrast to the previous scenario possessing separate transport barriers in the core and edge. [33] In such discharges the H mode edge region is characterized by the edge harmonic oscillation (EHO), a steady MHD activity which enhances particle transport as ELMs do, but without their undesired divertor heat pulses. The distinctive feature of such discharges is that the lack of ELMs allows the ITB to develop relatively uninhibited, but separation between the two barriers is maintained by a narrow region where the E×B shearing rate crosses zero. This regime is called the 'quiescent double barrier', or QDB, and can be sustained for several seconds.

In such a scenario the plasma transitions into H-mode shortly after NBI is applied, followed by an ELMy phase several hundred milliseconds in duration. The ELMs eventually cease, after which the QDB regime is entered and an ITB is formed.

Although the global confinement of similar co- and counter-NBI heated discharges is nearly equal, there is a striking difference in the shapes of Ti and V_t profiles. Consistent with the predictions [34], the counter-injected profiles are significantly broader than their co-injected counterparts because of the larger beam ion orbits. It has been theoretically demonstrated [35] that broader heating profiles may be expected to result in a broadened barrier. Another difference between co- and counter-injection is the interplay between the rotation and pressure gradient terms of the E×B shearing rate. This results in an increasing or broadening of the pressure profile and shearing rate, thus providing stabilization to long wavelength turbulence. [31]

Transport analysis indicates that unlike the previous scenario both the ion and electron thermal diffusivities are reduced from L-mode to similar levels (close to or even below neoclassical) in the core. The calculated $\omega_{E\times B}$ is large in regions of reduced transport, but exhibits a zero crossing between the core and edge barriers. Together with the observations of the core turbulence suppression, it is consistent with the frequently advanced hypothesis of turbulence suppression by E×B sheared flows.

The power threshold for this scenario appears to be around 9 MW, which is much higher than in the co-injected configuration. This QDB regime can be sustained for several seconds, terminating only when the neutral beam heating pulse ends. High confinement parameters of $\beta_N \approx 2.9$, $H_{89} \approx 2.5$ can be achieved.

2.2.5 FTU

Two main scenarios for the formation of an ITB on the FTU tokamak also utilize low or reversed magnetic shear. In both cases the RS configuration is achieved by off-

axis lower hybrid current drive (LHCD). Electron barriers are formed in FTU plasmas at high density, which makes these regimes more relevant and attractive for ITER considerations.

In the first ITB scenario, electron cyclotron (EC) power is launched during the plasma current plateau phase with the resonance located very close to the magnetic axis and after the barrier is created by the LHCD. [36] ECRF reinforces the ITB, making it possible to achieve higher temperatures (T_{e0} up to 7-8 keV compared to 4-5 keV in LH only case). FTU adopts the JET criterion $\rho^*_{Te} > 0.014$ to determine the location and size of the barrier. This condition shows that the barrier formed in this scenario is virtually steady: its width extends to $\rho \sim 0.4$ and stays constant for as long as LHCD is applied, corresponding to about 35 energy confinement times, and is not affected by the ECRF. No density peaking is observed in such plasmas. It should be noted that there is constant low-level MHD activity which appears to be localized in the ECRF deposition region and which persists throughout the discharges. Similarly to the low shear ASDEX case, this MHD activity might be responsible for the fact that no impurity accumulation is observed in this scenario.

In the second ITB scenario on FTU the ECRF power is injected during the I_p ramp-up phase with the EC resonance slightly shifted off axis. [37] This increases and broadens the electron temperature profile which in turn assists the peripheral deposition of the LH power, forming a RS configuration. Strong electron thermal barriers ($T_{e0} \geq 15$ keV) are formed this way and slight electron density peaking is observed as well. Calculations of the q profile show that the edge value, q_{95}, decreases with q_{min} shifting

outward, which creates a wider region of negative magnetic shear. The LH power deposition profile shifts outward according to the evolution of the q profile. Temporal analysis reveals that the ITB foot expands to $\rho > 0.5$, following the outward shift of the LH deposition. Moreover, the ITB location does not correlate with the LH power, which means that the radial location of the reversal of the shear is more significant than the magnitude of its variation. No MHD activity is detected during the initial phase of the discharge and therefore, some central impurity accumulation is observed. The ITB lasts for about 5-6 energy confinement times. However, in this scenario the ITB is usually destroyed by the MHD modes, which are identified to be tearing modes.

Transport analysis shows that electron thermal diffusivity χ_e can be as small as $0.1 - 0.5\ m^2s^{-1}$ within the barrier in spite of the very large heating power density of $10 - 20\ MWm^{-3}$. [38] The ion thermal diffusivity χ_i approaches neoclassical values during the ITB phase.

Some experiments with coupling of ion Bernstein waves (IBW) to tokamak plasma by mode conversion of the lower hybrid wave have been performed on FTU. [39, 40] It was found that during the IBW injection an increase of plasma density is observed at constant electron temperature. Thermal transport analysis shows a substantial reduction of the electron thermal diffusivity inside the IBW absorption radius, possibly due to the formation of an ITB by the IBW induced sheared flow.

2.3 Previous results on Alcator C-Mod

Internal transport barriers have been observed for a variety of operational regimes in Alcator C-mod plasmas [41, 42]: a) during H to L-mode back transition (enhanced neutron or EN mode), b) during lithium pellet injection (pellet enhanced performance or PEP mode), c) during the peaked density ohmic H-mode, and d) with off-axis ICRF heating. Recent studies on C-Mod have concentrated on the fourth scenario and have shown that ITBs can be routinely produced in EDA H-mode plasmas using off-axis ICRF heating both on the high field side and the low field side when the wave resonance is located outward of $|r/a| \sim 0.5$.

During the discharge in such a scenario, first the EDA H-mode develops 100-150 ms after applying ICRF heating power, corresponding to a few energy confinement times. The ITB appears spontaneously after the H-mode appears and evolves on a longer (~400 ms) time scale.

All occurrences of ITBs on C-Mod are marked by the peaking of electron density profiles. While the plasma temperature typically increases during these events, a similar peaking of the temperature profiles is less dramatic than that of the density. This is probably due to the high electron density and therefore, strong coupling between ions and electrons. As a result, in these experiments $T_e \approx T_i$, allowing the electron thermal conductivity to dominate. Probably the most obvious experimental evidence of the existence of the thermal barrier is the fact that central temperature does not decrease as the density rises during the ITB phase. An interesting and distinctive feature of many C-Mod ITBs is a decrease and even reversal of the central toroidal plasma rotation with respect to the intrinsic co-current rotation found in H-mode plasmas. [43]

Earlier it was found that following the formation of the ITB, the core electron density as well as the impurity density peaked continuously in the off-axis ICRF heated discharges, leading to a radiative collapse of the barrier when the core radiation power exceeded the RF input power. [41, 44] In later experiments it has been discovered that by adding a modest amount (up to 600 kW) of on-axis power to an ITB discharge (formed by off-axis heating), the increase of the electron and impurity densities can be stopped and the barrier can be maintained in steady-state [44, 45, 46] for ~10 confinement times. It must be stressed that during such steady-state ITB periods the toroidal rotation increases and even becomes positive. The mechanism for the ITB control has been explored through nonlinear gyrokinetic simulation and comparison with fluctuation measurements. [47, 48, 49] The halt of the density rise appears to be linked to the temperature dependent excitation of trapped electron mode (TEM) turbulence driven by the density gradient.

Regarding external control of the ITB plasma parameters, the peak electron density may be regulated by varying the delay time of the on-axis heating power after the initial off-axis ICRF is used to create the barrier. The characteristics of the ITB plasmas are also affected by the power level of the additional on-axis heating used to stabilize the barrier. Earlier experiments showed that when too much (> 600 kW) power was added, increasing co-current rotation and slowly decreasing core electron density is observed, indicating a steadily weakening ITB. [44, 50] However, recent experiment, in which a higher level of off-axis IRCF power was used, have allowed a higher level of central ICRF heating to be added to an established ITB plasma without terminating the ITB. [51] The location of the ITB can be somewhat controlled through magnetic field and plasma

current, suggesting the dependence on the q profile with higher q values leading to the narrower ITBs. [46, 52] Comparison with the calculated q profile determined by EFIT shows that the typical ITB location lies between q values of 1.1 and 1.34. So far the location and the triggering of the ITBs on C-Mod have not been linked to any particular rational q surfaces.

Transport analysis shows that during the ohmic L-mode phase (the beginning of the discharge), the effective thermal diffusivity $\chi_{eff} = (\chi_i n_i \nabla T_i + \chi_e n_e \nabla T_e)/(n_i \nabla T_i + n_e \nabla T_e)$ profile is fairly flat, with a value just above 1 m^2/s. [44] When the ITB is fully developed, there is a substantial drop (nearly a factor of 10) in χ_{eff} inside the barrier foot, to the level close to neoclassical. With the application of central power to stabilize the density rise, the χ_{eff} profile increases, but is still a factor of 3 below the L-mode value in the core. It should be noted that it is more appropriate to consider χ_{eff} in this case rather than individual thermal conductivities for ion and electrons because of strong coupling between electrons and ion in high-density C-Mod plasmas.

There is no central particle source in these discharges. Therefore, the central density increase suggests that the outward diffusion is exceeded by the inward pinch. The inferred pinch velocity is consistent with the calculated neoclassical Ware pinch velocity. [48, 50]

Since the sawtooth instability is always present throughout these ITB discharges, the sawtooth-induced heat pulse propagation can be used to study the thermal transport [50] in a similar way as it was used on JT-60U. The analysis shows that the deduced thermal conductivity reaches 0.4 m^2/s right at the ITB foot, while in the rest of the plasma

the profile is flat with the value of 4 m^2/s. The transport barrier width determined from the HPP turns out to be less than 1 cm, the limit of the diagnostic resolution. Another interesting feature of this analysis is that this narrow barrier quickly moves inward during its evolution by ~ 4.5 cm. This inward movement of the ITB is not seen from either temporal evolution of the density and temperature profiles or from other transport analyses. However, as it was pointed out before, the relation between the thermal conductivity inferred from power balance and that from HPP analysis remains unclear. Furthermore, the value of 4 m^2/s used outside the barrier region is significantly higher than the core diffusivity χ_{eff} determined in the transport analysis.

The mechanism for ITB production via off-axis ICRF heating is a major subject of this thesis research. First of all, in such scenarios ITBs are only observed for EDA H-mode plasmas. There is a threshold in ICRF resonance location: discharges with the resonance location inside $|r/a| \sim 0.5$ do not exhibit ITBs. Up to date there has not been found a clear ICRF power threshold other than that for obtaining EDA H-mode plasmas. Since the q profile is monotonic, these discharges lack the reversed magnetic shear stabilization present on other machines. Measurements of plasma flows on C-Mod are too limited to make conclusive statements about the role of the flow shear stabilization. Previous experiments suggested a strong link between an ITB formation and a reversal of the co-current to counter-current toroidal plasma rotation. [43, 44, 50] However, the apparent velocity profiles during the H-mode prior to ITB are typically flat for $0 < r/a < 0.6$, covering the ITB location at $r/a \approx 0.45$. [53] Furthermore, recent measurements of the central plasma rotation at higher magnetic field with the ICRF resonance placed on the low field side of the plasma did not reproduce the flow reversal trend. Ernst *et al.*

[47] estimated that E×B shearing rate is not significant on C-Mod during the ITB phase, so its role during formation is still unclear.

Suppression of toroidal ITG modes in the ITB region may explain access to the off-axis ICRF heated ITBs. Moving the RF resonance outward can locally flatten the temperature profiles and reduce the drive for ITG and electron temperature gradient (ETG) driven modes. Plasma conditions in the core ITB region are close to marginal stability [47, 48], so that even a small flattening can lead to a significant drop in the turbulence level. Redi *et al.* [54] performed microturbulent drift mode stability analyses of the C-Mod H-mode plasmas, supporting a link between turbulence suppression and ITB formation.

All of these motivated the work for my thesis research. Details and results from experiments dedicated to this study as well as transport analysis and gyrokinetic stability analysis can be found in the next few chapters.

References for Chapter 2

[1] M. J. Greenwald *et al.*, Phys. Rev. Lett. **53**, 352 (1984).
[2] E. J. Synakowski, Plasma Phys. Control. Fusion **40**, 581 (1998).
[3] R. C. Wolf, Plasma Phys. Control. Fusion **45**, R1 (2003).
[4] J. W. Connor *et al.*, Nucl. Fusion **44**, R1 (2004).
[5] F. M. Levinton *et al.*, Phys. Rev. Lett. **75**, 4417 (1995).
[6] E. J. Strait *et al.*, Phys. Rev. Lett. **75**, 4421 (1995).
[7] T. Fujita *et al.*, Phys. Rev. Lett. **78**, 2377 (1997).
[8] T. Fujita *et al.*, Phys. Rev. Lett. **87**, 085001 (2001).
[9] S. V. Neudatchin *et al.*, Plasma Phys. Control. Fusion **43**, 661 (2001).
[10] S. V. Neudatchin *et al.*, Plasma Phys. Control. Fusion **44**, A383 (2002).
[11] S. Ide *et al.*, Plasma Phys. Control. Fusion **44**, A137 (2002).
[12] T. Oikawa, Nucl. Fusion **40**, 1125 (2000).
[13] M. Greenwald *et al.*, Nucl. Fusion **28**, 2199 (1988).
[14] Y. Sakamoto *et al.*, Nucl. Fusion **41**, 865 (2001).
[15] O. Gruber *et al.*, Plasma Phys. Control. Fusion **42**, A117 (2000).
[16] O. Gruber *et al.*, Phys. Rev. Lett. **83**, 1787 (1999).
[17] G. Pereverzev *et al.*, 26th EPS Conf. On Controlled Fusion and Plasma Physics (Maastricht, 1999) ECA vol. 23J, p. 1429.
[18] R. C. Wolf *et al.*, Plasma Phys. Control. Fusion **41**, B93 (1999).
[19] S. Guenter *et al.*, Plasma Phys. Control. Fusion **41**, B231 (1999).
[20] C. D. Challis *et al.*, 26th EPS Conf. On Controlled Fusion and Plasma Physics (Maastricht, 1999) vol. 23J, 69.
[21] JET team (prepared by A. C. C. Sips), Nucl. Fusion **41**, 1559 (2001).
[22] C. D. Challis *et al.*, Plasma Phys. Control. Fusion **43**, 861 (2001).
[23] E. Joffrin *et al.*, Plasma Phys. Control. Fusion **44**, 1739 (2002).
[24] J. Mailloux *et al.*, Phys. of Plasmas **9**, 2156 (2002).
[25] G. M. D. Hogeweij *et al.*, Plasma Phys. Control. Fusion **44**, 1155 (2002).
[26] F. Crisanti *et al.*, Phys. Rev. Lett. **88**, 145004 (2002).
[27] M. Becoulet *et al.*, Plasma Phys. Control. Fusion **44**, A103 (2002).
[28] G. Tresset *et al.*, Nucl. Fusion **42**, 520 (2002).
[29] J. E. Kinsey *et al.*, Phys. Rev. Lett. **86**, 814 (2001).
[30] V. S. Chan *et al.*, Nucl. Fusion **40**, 1137 (2000).
[31] C. M. Greenfield *et al.*, Phys. of Plasmas **7**, 1959 (2000).
[32] C. L. Retting *et al.*, Phys. of Plasmas **5**, 1727 (1998).
[33] C. M. Greenfield *et al.*, Phys. Rev. Lett. **86**, 4544 (2001).
[34] G. M. Staebler *et al.*, Nucl. Fusion **37**, 287 (1997).
[35] D. E. Newman *et al.*, Phys. of Plasmas **5**, 938 (1998).
[36] V. Pericoli Ridolfini *et al.*, Nucl. Fusion **43**, 469 (2003).
[37] G. Bracco *et al.*, in *Proc. 18th Int. Conf. on Fusion Energy*, Sorrento, 2000, Vienna:IAEA, CD-ROM, file EX6/3. Available at http://www.iaea.org/programmes/ripc/physics/fec2000/html/model.htm.
[38] P. Buratti *et al.*, Phys. Rev. Lett. **82**, 560 (1999).
[39] B. Angelini *et al.*, Nucl. Fusion **43**, 1632 (2003).

[40] R. Cesario *et al.*, Phys. of Plasmas **8**, 4721 (2001).
[41] C. L. Fiore *et al.*, Phys. of Plasmas **8**, 2023 (2001).
[42] C. L. Fiore *et al.*, Fusion Sci. and Technol. **51**, 303 (2007).
[43] R. E. Rice *et al.*, Nucl. Fusion **41**, 277 (2001).
[44] R. E. Rice *et al.*, Nucl. Fusion **42**, 510 (2002).
[45] P. Bonoli *et al.*, in *Proc. of the 14th Topical Conf. on Radio-Frequency Power in Plasmas*, Oxnard, CA, American Institute of Physics, Woodbury, New York, 178 (2001).
[46] C. L. Fiore *et al.*, Phys. of Plasmas **11**, 2480 (2004).
[47] D. R. Ernst *et al.*, Phys. of Plasmas **11**, 2637 (2004).
[48] D. R. Ernst *et al.*, in *Proc. 20th IAEA Fusion Energy Conf.*, Vilamoura, Protugal, November 1-6, 2004, paper IAEA-CN-116/TH/4-1. Available as http://www-naweb.iaea.org/napc/physics/fec/fec2004/datasets/TH_4-1.html.
[49] D. R. Ernst *et al.*, in *Proc. 21st IAEA Fusion Energy Conf.*, Chengdu, China, Ocrober 16-21, 2006, paper IAEA-CN-149/TH/1-3. Available as http://www-pub.iaea.org/MTCD/Meetings/FEC2006/th_1-3.pdf.
[50] S. J. Wukitch *et al.*, Phys. of Plasmas **9**, 2149 (2002).
[51] C. L. Fiore *et al.*, Plasma Phys. Control. Fusion **46**, B281 (2004).
[52] J. E. Rice *et al.*, Nucl. Fusion **43**, 781 (2003).
[53] W. D. Lee *et al.*, Phys. Rev. Lett. **91**, 205003 (2003).
[54] M. H. Redi *et al.*, Phys. Plasmas **12**, 072519 (2005).

Chapter 3

3 Core Thomson scattering diagnostic on Alcator C-Mod

3.1 Incoherent Thomson scattering

Thomson scattering (TS) is the scattering of the incident electromagnetic wave off free charged particles (electrons) [1] [2, Ch.7]. It can be viewed as a limiting case of Compton scattering when the photon energy is much less than the charge rest energy: $\hbar\omega << m_e c^2$. It has become a common technique in modern plasma experiments for measuring plasma density and temperature.

Scattering of a single charged particle can be viewed as a two-step process, where the particle is first accelerated by the electric field $\mathbf{E_i}$ of the incident wave with the wavevector $\mathbf{k_i}$. The accelerating particle then emits a scattered wave $\mathbf{E_s}$ with the scattering wavevector $\mathbf{k_s}$. In the nonrelativistic limit the radiated power per solid angle can be calculated using the "dipole approximation" and is given by simple formula

$$\frac{dP}{d\Omega} = r_e^2 c\varepsilon_0 E_i^2 \sin^2\alpha, \qquad (3.1)$$

where $r_e \equiv \frac{e^2}{4\pi\varepsilon_0 m_e c^2}$ is the classical electron radius and α is the angle between $\mathbf{E_i}$ and $\mathbf{k_s}$. Choosing $\alpha = \pi/2$ maximizes the quantity (3.1), resulting in the geometry sketched in Fig. 3-1. This geometry is used for the C-Mod TS diagnostic, more details of which can be found in the next section.

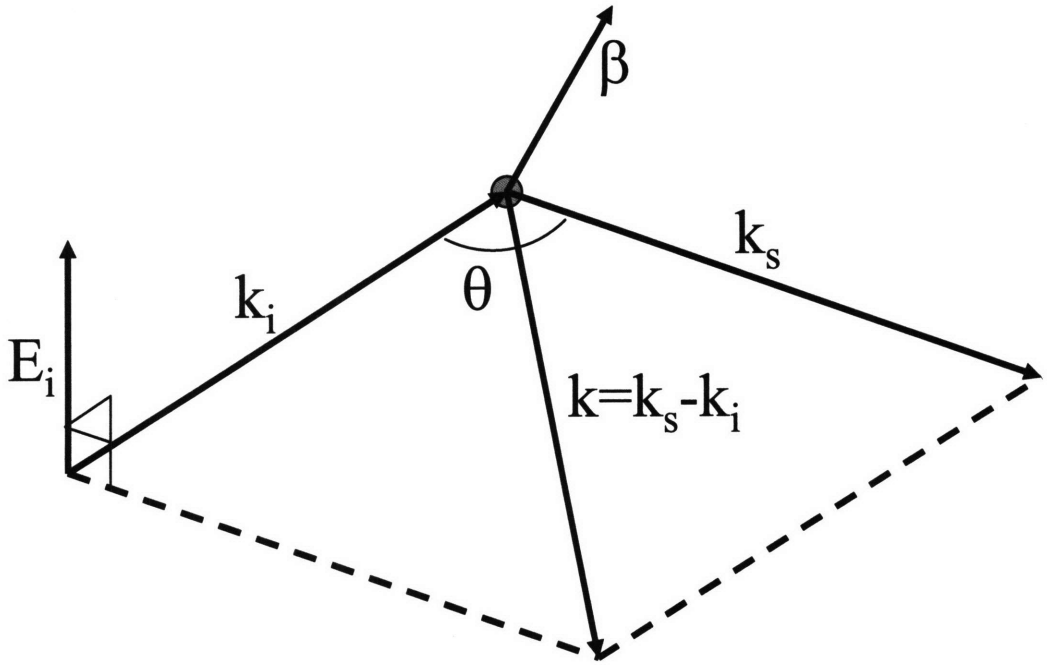

Figure 3-1 (Adapted from Hutchinson): Scattering geometry with $\alpha = \pi/2$, where β is the electron's relativistic velocity and θ is the angle of observation.

Scattering from individual charged particles in plasma occur with different phases. Now if these phase differences are uncorrelated the scattering powers from each electron can be summed to give the power scattered in the far field. It can be shown [1, Chs. 6-7] [2, §7.2] that this condition is satisfied when $k\lambda_D >> 1$, where $k = |\mathbf{k_s} - \mathbf{k_i}|$ and $\lambda_D = \left(\frac{\varepsilon_0 T}{ne^2}\right)^{1/2}$ is the Debye length. If this is not true then scattering from each individual electron will be almost balanced by the absence of scattering from its shielding cloud. For ions, though, there is going to be scattering from their shielding electrons clouds, since ions are heavier and therefore, direct ion scattering is negligible. The latter process is called coherent Thomson scattering and it conveys information about the ion distribution function [2, §7.3].

Since $k_s \approx k_i$, the incoherence condition can be rewritten in the form of $k \approx 2k_i \sin(\theta/2)$, where θ is the angle between the incident and the scattering vectors. Therefore, this condition can be transformed into

$$\frac{\lambda_i}{\lambda_D} << 4\pi \sin\frac{\theta}{2}, \tag{3.2}$$

where λ_i is the wavelength of the incident wave. Relation (3.2) is easily satisfied for the C-Mod TS diagnostic ($\lambda_i \sim 1$ μm, $\lambda_D \sim 20$ μm, $\theta \sim \pi/2$).

Satisfying the incoherence condition ensures that scattering from individual electrons is unaltered by their shielding cloud, and thus incoherent Thomson scattering reveals information about the electron distribution function.

Each electron moving with the velocity v (or relativistic β) sees a Doppler-shifted incident wave and likewise emits a Doppler-shifted scattered wave. The frequency of the latter can be written as

$$\omega_s = \omega_i + \mathbf{k}\cdot\mathbf{v} = \omega_i + (\mathbf{k_s} - \mathbf{k_i})\cdot\mathbf{v} = \omega_i\left(\frac{1-\hat{\mathbf{k}}_\mathbf{i}\cdot\mathbf{v}/c}{1-\hat{\mathbf{k}}_\mathbf{s}\cdot\mathbf{v}/c}\right) \tag{3.3}$$

Assuming a Maxwellian distribution for the plasma electrons the ratio of the scattered to the incident power is given by [1, Ch. 3]

$$\frac{P_s}{P_i} = r_e^2 n_e L\left|\hat{\mathbf{k}}_\mathbf{s}\times(\hat{\mathbf{k}}_\mathbf{s}\times\hat{\mathbf{E}}_\mathbf{i})\right|^2 S(T_e,\theta,\lambda) \tag{3.4}$$

where n_e is the electron density, L is the length of the scattering volume and $S(T_e, \theta, \lambda)$ is a form factor determining the shape of the spectral distribution as function of electron temperature T_e, angle of observation θ and scattered wavelength λ. For the case in which the polarization of the incident radiation is perpendicular to the scattering plane ($\alpha = \pi/2$),

the scattered power in the range $\lambda_s \rightarrow \lambda_s + d\lambda$ and in the solid angle $d\Omega$ is given by [1, Ch. 9]

$$P_s(T_e,\theta,\lambda_s)d\lambda_s \cdot d\Omega = \frac{P_i r_e^2 d\Omega n_e L}{2\sqrt{\pi}\sin\frac{\theta}{2}}\left\{1-\frac{3.5\Delta\lambda}{\lambda_i}+\frac{c^2\Delta\lambda^3}{4v_{th}^2\lambda_i^3\sin^2(\frac{\theta}{2})}\right\} \times \frac{cd\lambda_s}{v_{th}\lambda_i}\exp\left\{-\frac{c^2\Delta\lambda^2}{4v_{th}^2\lambda_i^2\sin^2(\frac{\theta}{2})}\right\}, \quad (3.5)$$

where $v_{th}=(2kT_e/m_e)^{1/2}$ is the electron thermal velocity. For the low-temperature plasma ($\Delta\lambda/\lambda_i \rightarrow 0$) this spectrum has a Gaussian shape. Therefore, for a given angle of observation the width of the spectrum of scattered photons is proportional to the square root of the local plasma temperature, while the number of photons scattered is proportional to the local plasma density. For higher plasma temperatures, the TS spectrum broadens and shifts toward shorter wavelengths. The 'blue shift' of the spectrum is a relativistic effect, and becomes important at $T_e \sim 1$ keV. Typical central T_e values on the Alcator C-Mod tokamak are 1-5 keV. Therefore, high-temperature corrections, included in Eq. (3.5), are required.

3.2 Diagnostic setup and principles of operation

The Thomson scattering diagnostic on C-Mod has two major components, a core TS and an edge TS systems that measure T_e and n_e in these respective regions of the plasma. The core TS system consists of two parts: the original diagnostic [3, 4], which collected its first data in 1995, and a 2002 upgrade [5], which was the major experimental component of this thesis. All of the diagnostics operate simultaneously, sharing a laser

setup, collection optics, and a variety of controlling hardware and software tools. For more detailed description of all three systems see Ref [6].

3.2.1 Laser setup and collection optics

The diagnostic uses two identical Continuum PowerLight 9030 Q-switched Nd:YAG lasers (λ_0 = 1064 nm) [7], which are controlled remotely with a PC running LabVIEW software. Each laser has a fixed pulse rate of 30 Hz, with a nominal 1.3 J, 8 ns pulse. The triggers for the flash lamp and the Q switch pulses are generated by CAMAC hardware, set up to provide two staggered Nd:YAG pulse trains and subsequent measurements of TS profiles at 60 Hz. In some special cases the pulse trains can be brought close to each other to within ~ 4 ms (limited by the acquisition electronics of the edge TS system) in order to study fast phenomena in the plasma. Each Nd:YAG beam is coaligned with a CW He-Ne laser to assist alignment of the beams in the tokamak vessel.

The two beam paths are made close to parallel ($d\theta \sim 5$ mrad) and directed along a beam path of 15 m length to a vertical port positioned over the tokamak vessel. A pair of remotely controlled steering mirrors on the laser optical bench is used to make fine adjustments to one or both beam positions above the machine. The beams are steered through a vertical port and maintained at a major radius of 0.69 m, the approximate position of the plasma center. A 3 m focal length doublet atop the machine focuses the beams such that the nominal beam width is less than 2 mm across the length of the vertical chord passing through a typical C-Mod plasma. Fig. 3-2 shows the tokamak poloidal cross section as well as contours of constant poloidal flux obtained from the magnetic reconstruction code EFIT [8].

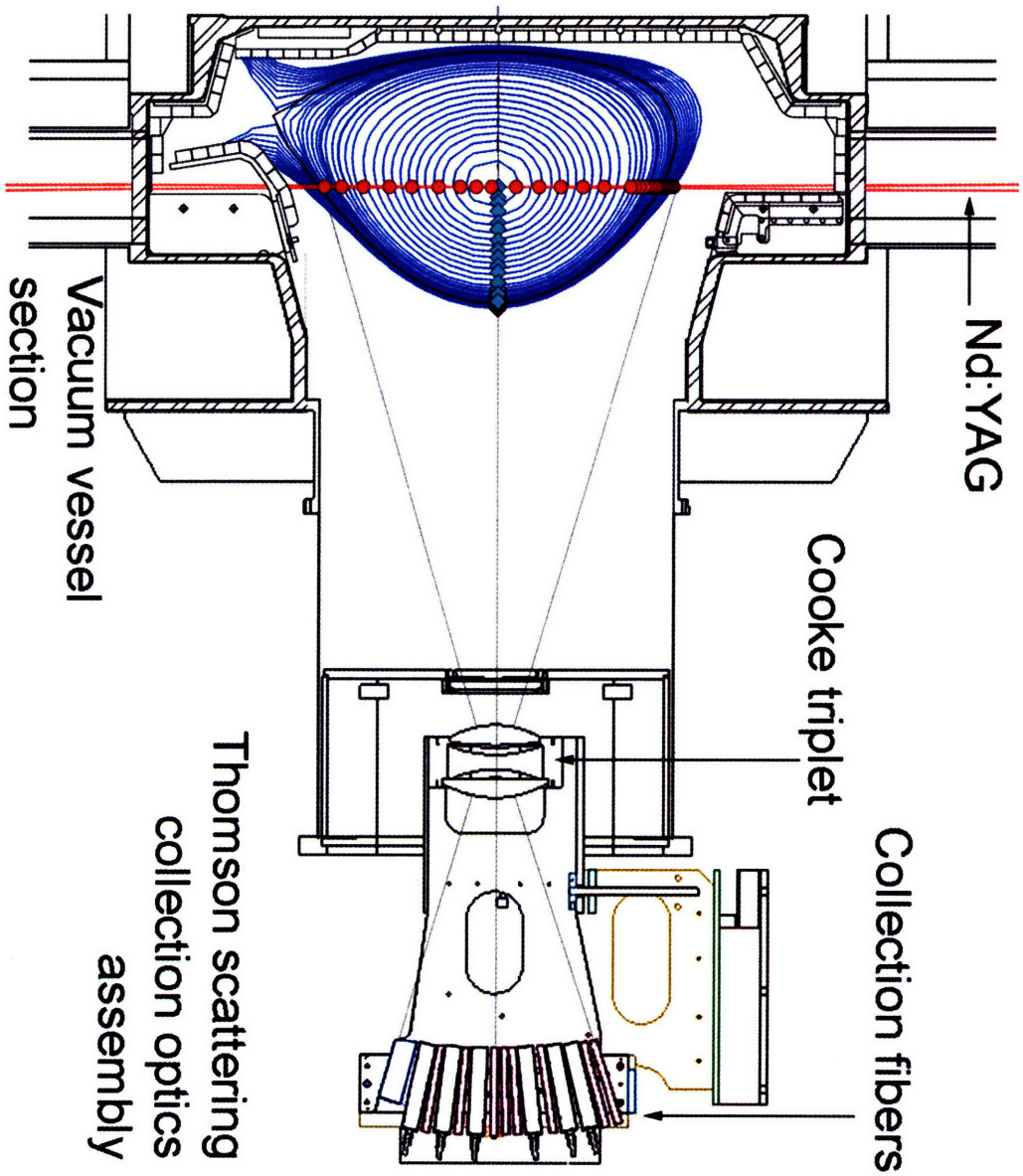

Figure 3-2: Alcator C-Mod cross-section and layout of TS collection optics (Figure courtesy of J. W. Hughes).

Also shown are the TS collection optics and sample ray traces. Thomson scattered light is collected by an air-spaced Cooke triplet lens at F/7. This lens has a focal length of 30.8 cm and 1:2 demagnification, with minimal aberrations. At the focal surface of this lens are the TS collection fibers, mounted upon a vertical tilt plate. [5] The tilt plate with mounted fibers and controlling stepper motors is shown in Fig. 3-3. The vertical alignment of the tilt plate relative to the laser beam is monitored with two special sets of 1 mm fibers, which are mounted on the top and bottom of the plate. The three fibers in either set are aligned horizontally and closely spaced, thus obtaining a crude Nd:YAG beam image. The tilt plate lateral position can then be adjusted across a distance of more than 2 cm with submillimiter precision, and the angle of the plate can be varied up to 10°. Stepper motors controlling the movements of the fiber plate can be operated remotely using programming logic control (PLC), allowing for alignment corrections between plasma discharges.

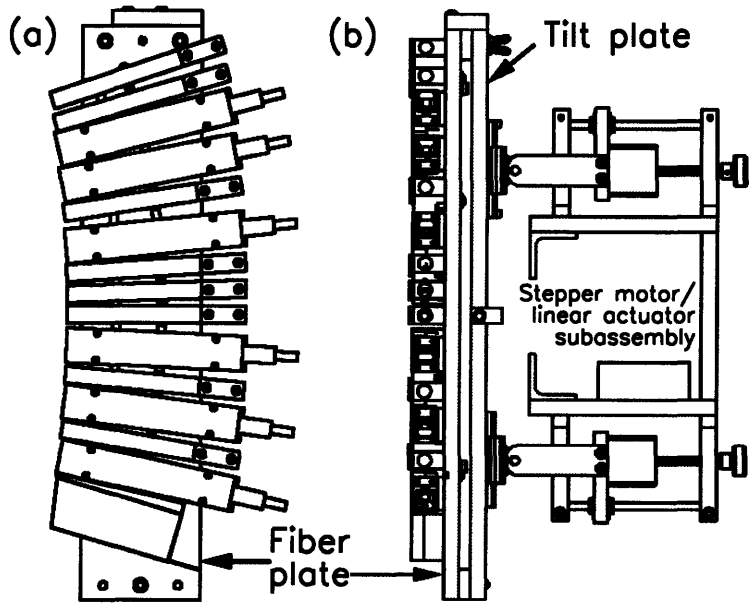

Figure 3-3: TS fiber mount assembly from a) side and b) rear, showing the linear actuators for horizontal position and tilt adjustment.

The fiber position on the tilt plate and the radial location of the laser beams determine the vertical location of the scattering volumes. The height of each scattering volume is roughly twice the vertical dimension of its corresponding fiber, and it is this dimension that determines the spatial resolution of a given TS channel. The fibers for the core TS upgrade system are ~ 4 mm in extent, which results in L ~ 8 mm for the observation volumes. The smaller size allows both improved spatial resolution in a given TS channel and closer spacing between fibers. Fig. 3-2 indicates the location of scattering volumes for one possible arrangement of collection fibers. Also shown are the mappings of these volumes along the surfaces of constant poloidal flux to the outboard tokamak midplane. Such mappings are obtained from the EFIT equilibrium, and radial profiles are typically plotted in terms of midplane radius, under the assumption of constant T_e, n_e on a flux surface. A midplane radial resolution of ~ 1 cm can be achieved for certain regions of interest using core TS diagnostics.

3.2.2 Multi-channel filter polychromator setup

The collected TS photons are transmitted to a system of polychromators designed to detect scattered light falling into distinct spectral bands near the Nd:YAG laser line. The core TS upgrade employs eight 4-channel compact filter polychromators [9] fabricated by General Atomics, modified to accept an input 0.4 cm fiber bundle at F/3.5. Each spectral channel detects light within a certain wavelength range defined by the corresponding filters in front of the detectors. The physical layout of the polychromator is presented in Fig. 3-4, while typical spectral functions are plotted in Fig. 3-5. The polychromators use Si avalanche photodiodes (APDs) for detection. The timing for this

pulsed data acquisition is provided by a portion of the laser beam that leaks through steering mirrors as the beam is directed to the tokamak.

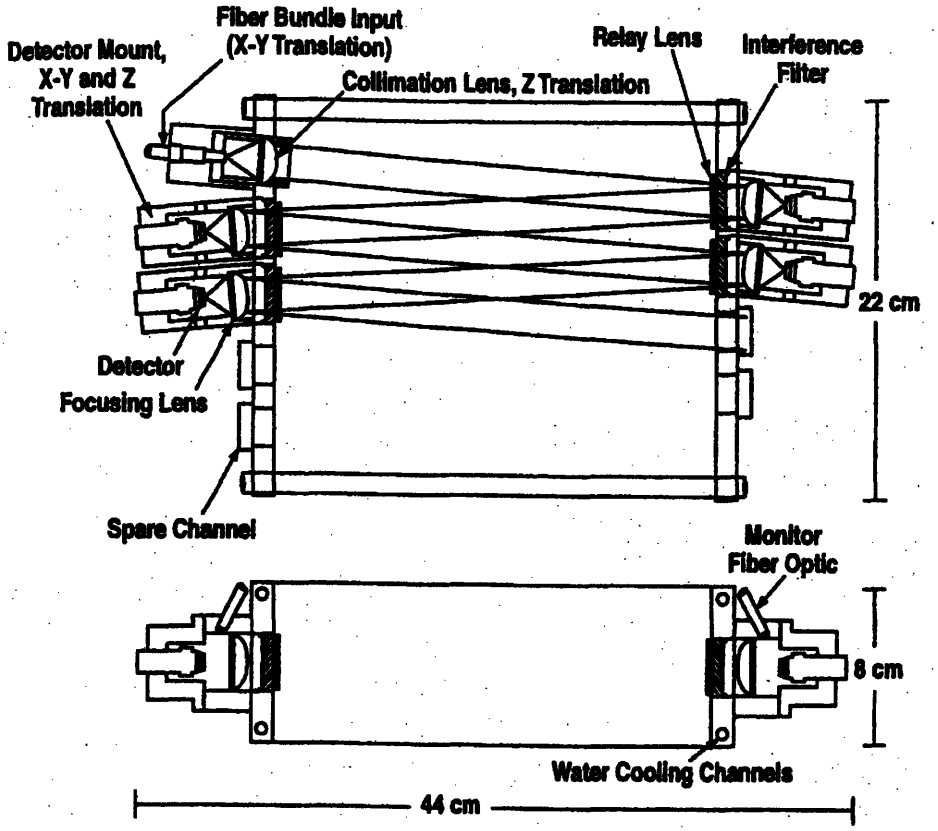

Figure 3-4: Design of a four channel polychromator using 3.0 cm diameter interference filters and relay lenses.

The gain of the detectors is sensitive to temperature and it changes approximately 3% per degree C. [10] Therefore, all 8 polychromators are placed into a thermal enclosure. A temperature control system was designed and built to ensure that APDs operate at constant temperature. A set of heaters and a water loop running from the thermostat through the polychromators provide temperature control for the system. The water serves as heating source during the startup phase and more as a heat sink when the

system is near the equilibrium temperature. Eight thermistors placed on APDs and distributed uniformly in the thermal enclosure box provide real time spatial temperature readings. Software, which operates with programmable logic controller (PLC) modules, was designed such that the polychromators reach the temperature set point of 34°C in ~ 1 hr. After the system reaches the thermal equilibrium the temperature stays constant in time and uniform in space to within 0.1°C.

The APDs have output signals for both the pulsed contribution from TS and the slowly varying contributions from plasma background light. During plasma operation the channel with the fast varying signal is used, since the plasma background signal is isolated and subtracted from the total signal by means of a delay line technique in the detector circuitry. [10] The signal corresponding to TS scattering has 0-1V amplitude and is digitized by LeCroy FERA fast charge digitizers, translating voltages into counts of 0-2048.

3.3 Calibrations

Including geometric factors the measured intensity at each wavelength in k^{th} spectrometer can be written as

$$I_k(\lambda) = P_i r_e^2 \Omega_k n_e L \eta_k \nu_k(\lambda) S(T_e, \theta, \lambda), \qquad (3.6)$$

where Ω_k is the fiber's collection angle, η_k is the wavelength independent optics transmission coefficient, $\nu_k(\lambda)$ is the optics instrumental function, $S(T_e, \theta, \lambda)$ is the form factor from Eq. (3.5).

A signal registered by each detector is the result of the convolution of the TS spectrum and the detector's instrumental function. Therefore, for the j^{th} detector in the k^{th} spectrometer the registered signal is

$$I_{j,k} = P_i r_e^2 \Omega_k n_e L \eta_k \int \nu_{j,k}(\lambda) S(T_e, \theta, \lambda) d\lambda \tag{3.7}$$

Introducing the relative calibration coefficients as

$$c_{j,k} = \frac{\int \nu_{1,k}(\lambda) d\lambda}{\int \nu_{j,k}(\lambda) d\lambda} \tag{3.8}$$

gives a normalized spectral response for each detector

$$\mu_{j,k} = \nu_{j,k} \cdot c_{j,k}. \tag{3.9}$$

Expression (3.7) can then be rewritten as

$$I_{j,k} = P_i r_e^2 \Omega_k n_e L \eta_k \frac{\int \mu_{j,k}(\lambda) S(T_e, \theta, \lambda) d\lambda}{c_{j,k}}. \tag{3.10}$$

The relative calibration coefficients (3.8) show how much 'weight' different spectral channels have with respect to each other. When analyzing the data during plasma operation the measured signals are corrected for these coefficients and normalized to the laser energy, which is measured independently

$$I_{j,k}^{norm} = \frac{I_{j,k} \cdot c_{j,k}}{P_i} = r_e^2 \Omega_k n_e L \eta_k \int \mu_{j,k}(\lambda) S(T_e, \theta, \lambda) d\lambda. \tag{3.11}$$

For given angles of observation, a table of values for $\int \mu_{j,k}(\lambda) S(T_e, \theta, \lambda) d\lambda$ is calculated for different plasma temperatures. This table is then used for a non-linear least-squares fit to the signals $I_{j,k}^{norm}$. The fitting parameters are T_e and χ, where

$$\chi = r_e^2 \Omega_k n_e L \eta_k. \tag{3.12}$$

From this plasma electron density can be derived

$$n_e = \chi \cdot \frac{1}{r_e^2 \Omega_k L \eta_k}. \tag{3.13}$$

3.3.1 Spectral Calibration

In order to measure the instrumental functions of each channel the input fibers of the polychromators are filled at F/3.5 with the output of a scannable Czerny-Turner monochromator having a known spectral function. A wavelength scan is performed for all polychromator channels over a range of 700 – 1100 nm. Fig. 3-5 shows spectral distributions for two temperatures as well as typical spectral responses of the polychromators.

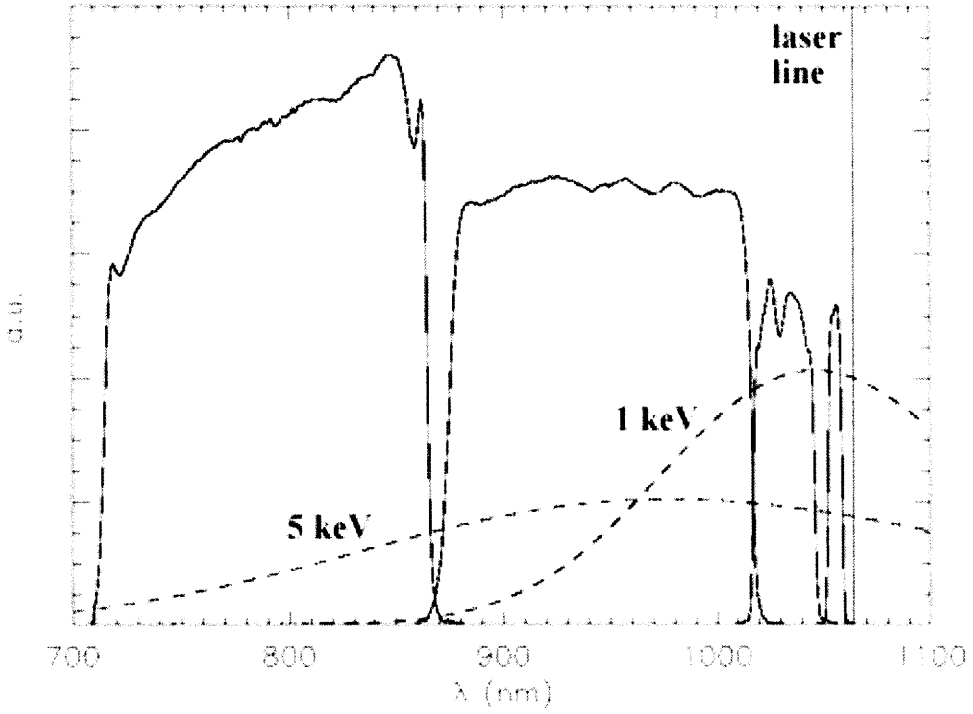

Figure 3-5: Typical spectral responses of the core TS polychromators (solid lines). Dashed curves represent typical TS spectra for a given density and angle of observation.

Subsequent to the collection of the normalized spectral response the integral response of the individual channels is measured by illuminating the collection fibers with a uniform source of known spectral brightness. For this "white plate" calibration, the fibers are filled with F/3.5 using a Labsphere integrating sphere with spatially uniform intensity and spectral intensity varying little over the domain of interest. The detector responses to this steady light source determine the relative calibration coefficients (3.8).

From the Fig. 3-5 it can be seen that for a given density higher temperature results in more scattered light in the spectral channels with bandwidths that are further from the laser line. This effect is due to both widening of the Thomson scattering spectrum and the "blue shift" and is captured by the analytical formula for $S(T_e,\theta,\lambda)$ (3.5). As mentioned above, the detectors' responses $\int \mu_{j,k}(\lambda) S(T_e,\theta,\lambda) d\lambda$ are calculated for different plasma temperatures. Typical form of these functions for a given plasma density and a given polychromator with angle of observation $\theta = \pi/2$ is shown in Fig. 3-6. On this plot, functions which have non-zero values at higher temperatures correspond to the spectral channels that are further away from the laser line. These values are used in the non-linear least squares fit of Eq. (3.11) with the T_e being one of the fitting parameters. Calculated uncertainties in T_e from the least squares fit are typically 10-15%. From Fig. 3-6 one can also determine the useful T_e range of the core TS system, which can be defined as the region with substantial gradients in detectors' response functions for more than one spectral channel. This range is approximately 0.03 – 10 keV for the core TS upgrade.

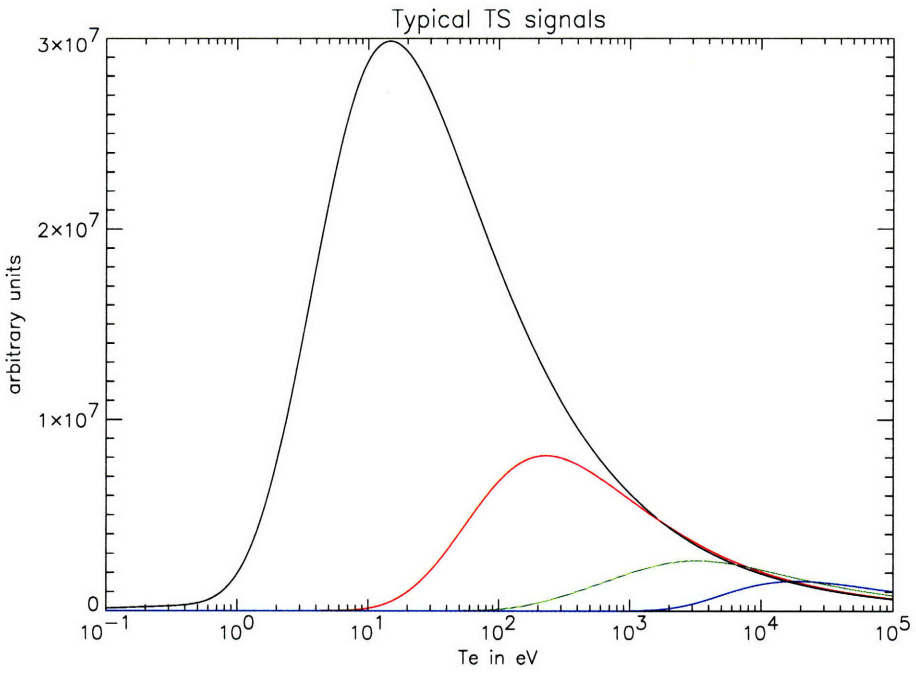

Figure 3-6: Typical detectors responses for a given electron density and angle of observation $\theta = \pi/2$. Curves with non-zero values at higher temperature correspond to spectral channels with bandwidths further away from the laser line.

3.3.2 Absolute calibration

The plasma density is obtained from the fitting parameter χ in Eq. (3.13). In principle the optics transmission coefficient η_k as well as the geometric factors Ω_k and L can be measured directly. However, high uncertainties associated with the measurements undermine the results. The coefficient $\frac{1}{r_e^2 \Omega_k L \eta_k}$ is called the absolute calibration coefficient and in practice is measured as a whole.

Raman scattering is considered a conventional technique for the intensity calibrations of TS systems. [11, 12, 13, 14, 15] In this method the vacuum chamber used for plasma operations is filled with a diatomic molecular gas and a laser scattering signal

is measured. Known cross-sections for Raman scattering make it possible to relate the measured signal to the gas pressure and, therefore, relate measured TS signal to the plasma density. The choice of a particular gas and type of scattering depends on each particular TS diagnostic. One must have at least one strong Raman scattering line in the range of wavelengths used to measure the TS spectrum.

Calibrations with both D_2 and H_2 have been done for the core TS system on C-Mod. However, the very low signals lead to high uncertainty in the calibration coefficients, undermining the results. Furthermore, the walls of the vacuum vessel of the Alcator C-Mod tokamak absorb some fraction of the gas molecules. The absorbed molecules dissociate during plasma discharges, penetrate into the plasma volume and, thus, affect plasma operations. Due to this there are restrictions on filling the tokamak with gases other than D_2, which is the source of the major ion species during normal operation. Hence, the calibrations with gases other than D_2 cannot be done easily.

Rayleigh scattering in molecular gases is another standard technique for TS intensity calibrations. [15, 16] Unlike Raman scattering this type of scattering occurs without wavelength shift from the laser line. Since the polychromators used for the core TS system on the C-Mod cut off the laser line at 1064 nm, this type of scattering is not an option for these intensity calibrations.

A new absolute calibration technique was developed and tested over the course of this thesis research. [17] The proposed method is based on the fact that electron cyclotron emission cannot propagate through the plasma if the plasma density is above a critical cutoff value. Therefore, if the abrupt loss of the ECE signal is registered during the plasma discharge this clearly indicates that the plasma density has reached this critical

value. This value in its turn can be calculated from the dispersion relation for ECE wave propagation and be used for TS density calibration.

To obtain an absolute calibration for TS we make special discharges, during which we ramp the density up to reach the critical values to cut off the ECE signal. The ECE diagnostic used for this calibration is a grating polychromator (GPC), which has 9 spatial channels and is normally used to measure electron temperature profiles. [18] This system measures second harmonic ECE perpendicular to the magnetic field in the extraordinary mode. For this type of mode and angle of observation, from the dispersion relation it can be determined that the ECE signal is cut off if the second harmonic ECE frequency is less than the right-hand cutoff frequency [2, §5.2]

$$\omega_{GPC} = 2\Omega_{ce} < \omega_R = \Omega_{ce}\left[1 + (1 + 4\omega_p^2 / \Omega_{ce}^2)^{1/2}\right]/2, \qquad (3.14)$$

where $\Omega_{ce} = eB/m_e$ is electron cyclotron frequency and ω_p is the electron plasma frequency. So, the condition for wave propagation becomes

$$\Omega_{ce}^2 > \tfrac{1}{2}\omega_p^2 \qquad (3.15)$$

This condition can be rewritten in terms of the plasma density

$$n_e < n_{crit}, \qquad (3.16)$$

where $n_{crit} = \frac{1}{2}\frac{\omega_{GPC}^2 m_e \varepsilon_0}{e^2}$ is the critical plasma density at which ECE signal is cut off.

The GPC diagnostic operates at fixed, experimentally verified frequencies, which can be adjusted shot-to-shot by selection of the grating spacing and angle. There is a unique critical density value for each channel. During a plasma discharge the density increases and, as the local n_e reaches the critical value n_{crit}, abrupt loss of signal in the corresponding GPC channel is observed. Radial positions of the emission for all spatial

GPC channels are known since the frequency of the emission is proportional to the magnetic field in the tokamak. The magnetic field in the tokamak in turn is approximately inversely proportional to R, the major radius. This brings $\sim 1/R^2$ dependence into the critical density profile. Corrections due to poloidal field and paramagnetic effects are computed using EFIT. By changing the magnetic field during a plasma discharge we shift the radial positions of the ECE channels. Some of them might be shifted to the region where the local plasma density is above the critical value corresponding to these channels, and consequently the cutoffs are observed. So, as the density profile evolves and/or the magnetic field changes during a plasma shot, cutoffs can be observed in the GPC channels one by one across the entire outboard side of the plasma. Thus, we are able to calculate the density values at certain positions in the plasma at times of ECE cutoffs and use them for absolute calibration of the TS system.

Fig. 3-7 shows time-dependent plots of some ECE data along with the line-integrated density for a 4.5 T discharge. In order to obtain cutoffs in the GPC channels, in this case we kept the magnetic field constant and relied on an increase in the plasma density. This keeps the radial positions of the observed ECE emission at fixed values and decreases the uncertainty in the radial positions of the n_{crit} values. As the plasma density increases (Fig. 3-7 a) during the discharge density ramp, the cutoffs are seen consequently starting from the outer channels (Fig. 3-7 b-e). The critical density value and the radial position in plasma at the time of the cutoff are calculated for each channel in which cutoff is observed. In general, the data points in the reconstructed critical density profile do not coincide in time and space with those of the TS system. By interpolating the measured core TS profiles to the observed cutoffs in time and space we

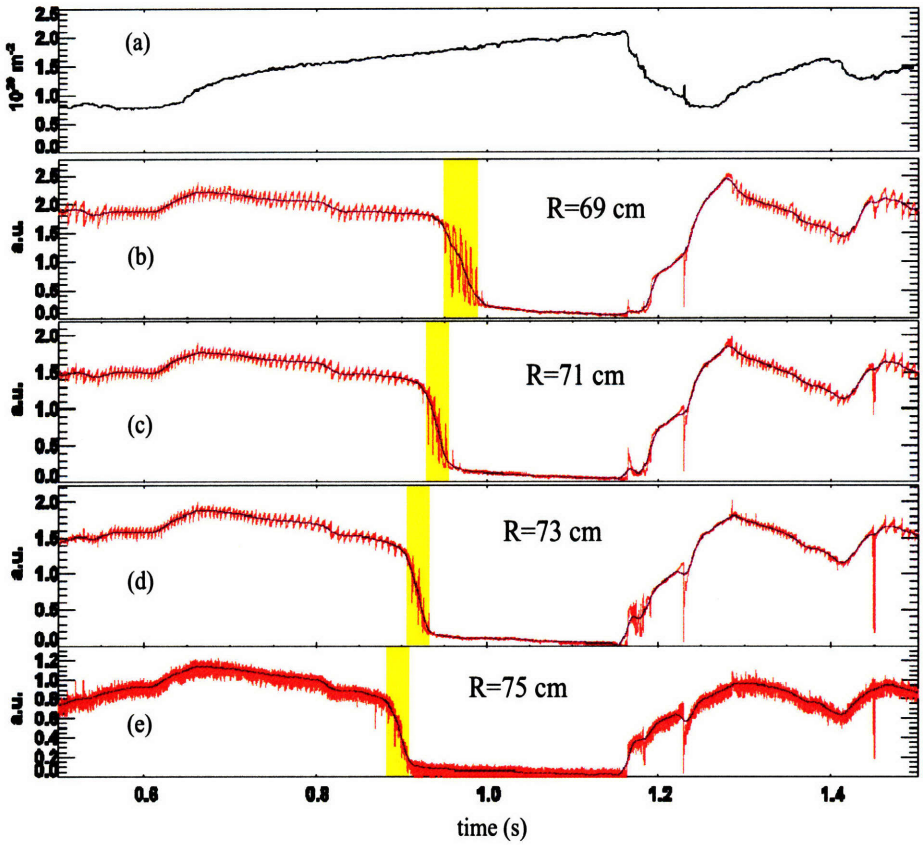

Figure 3-7: Time-dependent ECE cutoff data for 4.5 T discharge in which the density (a) was ramped. ECE signal from four channels are plotted in (b)-(e). Cutoffs are shown as shaded regions.

can determine a set of calibration coefficients for the TS channels.

The result is shown in Fig. 3-8. The diamonds are the ECE cutoff measurements at corresponding times (shadow regions in Fig. 3-7). The circles represent TS density profiles with applied calibration coefficients at the times closest to the ECE cutoff times.

There are enough TS radial data points to confirm that density profiles in plasma regimes used for the absolute calibration purposes are smooth and monotonic. This is also confirmed by the independent measurements from a visible bremsstrahlung (VB) diagnostic, which justifies the procedure of interpolating density values in space. During the density ramp phase of plasma discharges designated for TS calibration, density

linearly increases in time, which is confirmed by the interferometer measurements (Fig. 3-7 a). This justifies the interpolation of the density profile in time. Comparisons of the TS measurements calibrated using this procedure with the results from other diagnostics will follow in the next section.

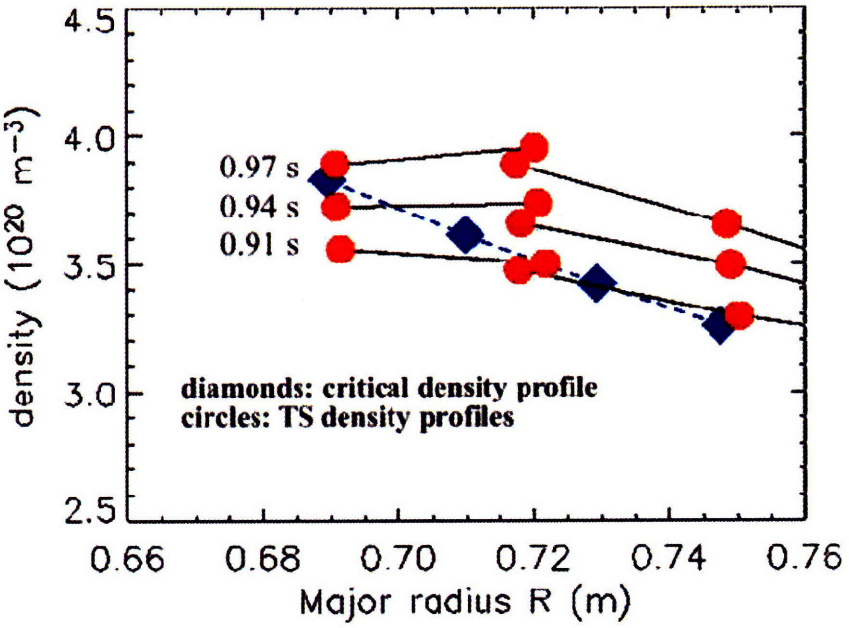

Figure 3-8: TS data points (circles) and ECE critical density values (diamonds).

Two major sources of uncertainty in the derived calibration coefficients are the uncertainties in the measured TS signal and those due to interpolation (usually ~ 5-10% combined). The uncertainty in the cutoff radial positions is ≤ 1 cm. The drop in ECE signal occurs over a finite time window due to strong beam divergence, since the index of refraction approaches 0 as the density approaches the critical value. However, this effect is minimized since the diagnostic's field of view lies on the midplane and the uncertainty in the absolute density values due to finite time window of the ECE cutoffs is ~ 5%.

There is an additional uncertainty associated with the difference in the radial positions of the TS data points and the ECE cutoff densities. Combined uncertainties determine the effective weight of each ECE cutoff in a weighted average, which determines the calibration coefficients for the adjacent TS channels. After several plasma discharges with clear cutoffs for each TS channel, we can determine absolute calibration coefficients for the TS system with 10% or less uncertainty, which is less than the uncertainty of the results obtained from the gas scattering calibrations.

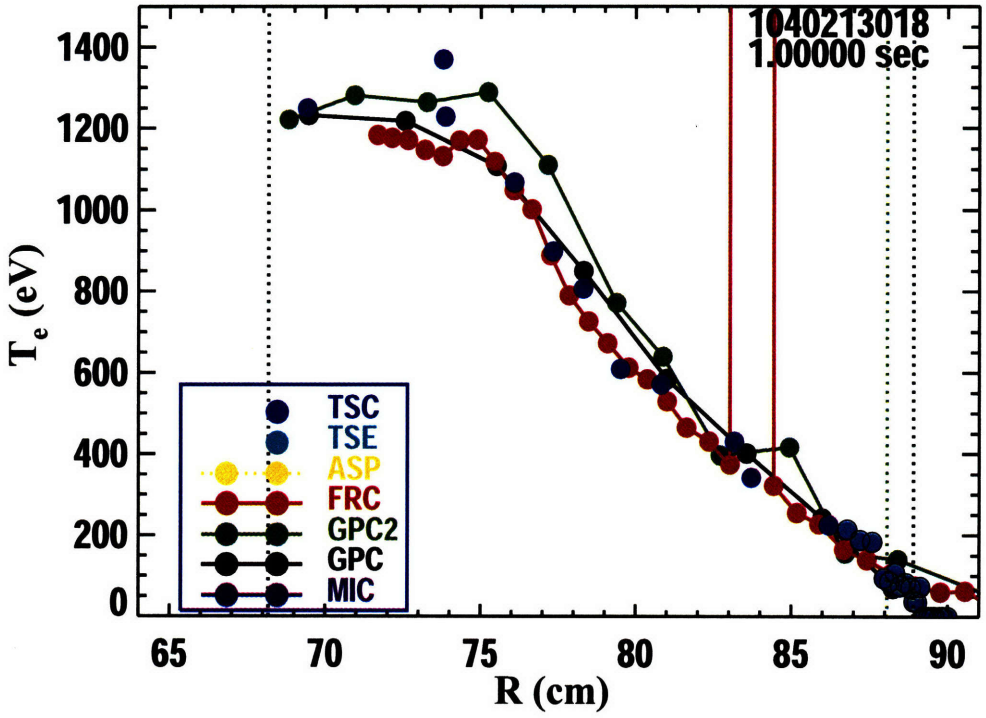

Figure 3-9: Electron temperature profile measurements from various diagnostics. Labels: TSC – core TS diagnostic, TSE – edge TS diagnostic, ASP – A-port scanning probe (data not available for this shot), FRC – heterodyne ECE system, GPC – 9-channel prating polychromator system, GPC2 – 18-channel grating polychromator system, MIC – Michelson interferometer (data not available for this shot).

3.4 Comparison with other diagnostics

It is desired that comparison of core TS results with measurements from other diagnostics be performed to verify operational validity. Temperature profile comparison is fairly straightforward and is shown in Fig. 3-9. It is found that within experimental uncertainties (~ 10-15% for any diagnostic) electron temperature profiles from core TS are consistent with those from various ECE diagnostics. It should also be noted that good agreement is obtained consistently between outer core TS measurements and edge TS for both T_e and n_e.

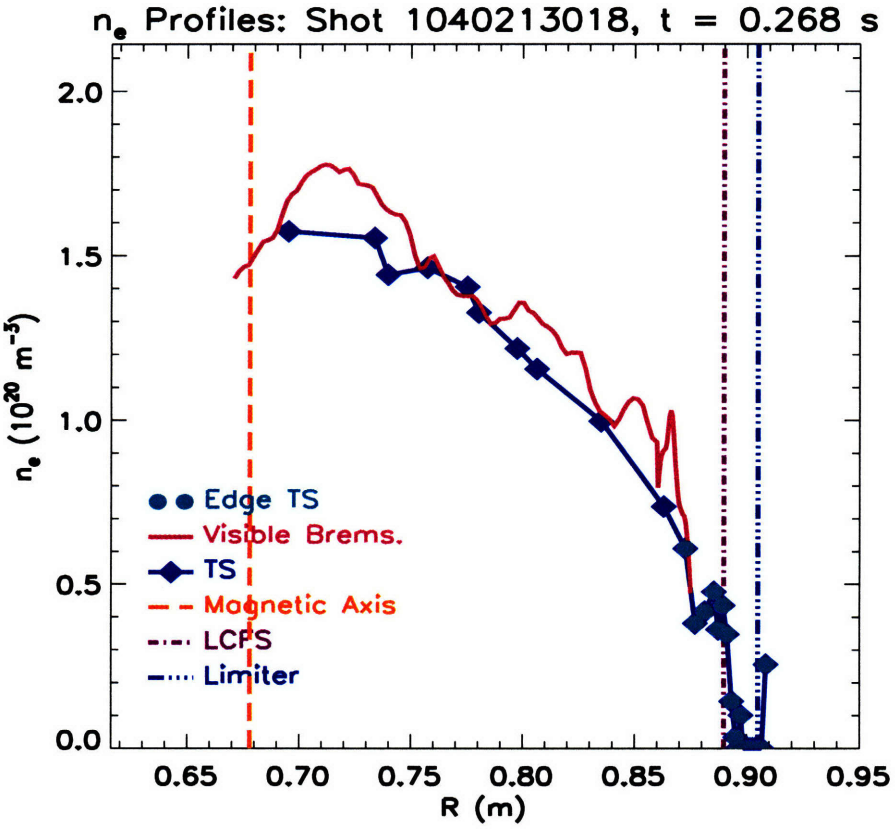

Figure 3-10: Typical density and VB profiles during L-mode.

Density measurements are compared to those from the Visible Bremsstrahlung (VB) diagnostic and interferometry. The VB diagnostic on C-Mod [19] detects

continuum emission profile and through Abel inversion with temperature correction yields a $n_e\sqrt{Z_{eff}}$ profile, where $Z_{eff}(R)$ is the effective plasma charge. Previous results [19, 20] indicate that in L-mode discharges at typical C-Mod densities Z_{eff} is close to 1 across the whole plasma. Fig. 3-10 shows typical L-mode profiles of both core TS and edge TS as well as $n_e\sqrt{Z_{eff}}$, derived from the visible continuum measurements. Z_{eff} derived from the core TS and VB measurements is close to 1 throughout the whole plasma cross-section, which implies a good agreement between core TS and $n_e\sqrt{Z_{eff}}$ profiles.

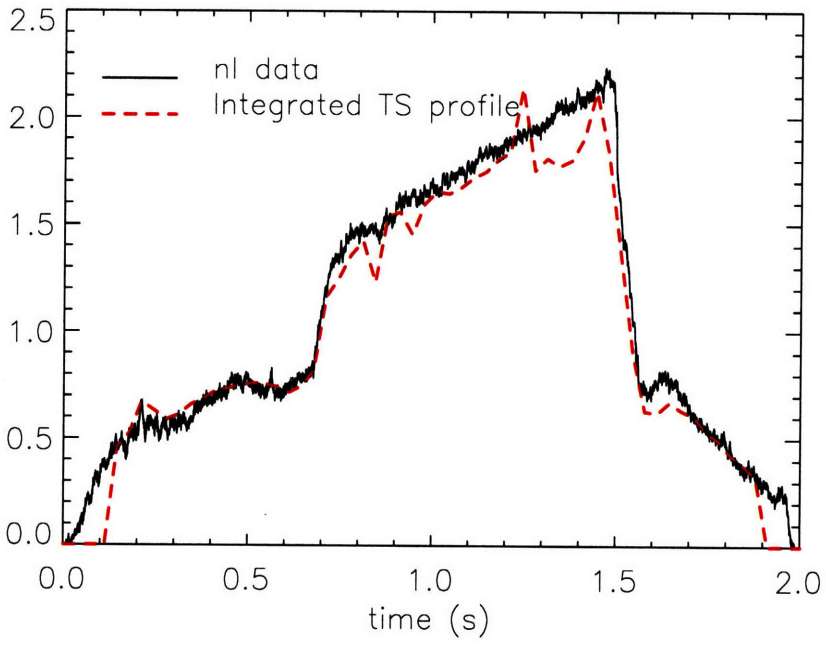

Figure 3-11: Comparison of the integral under the TS density profile (dashed line) with the line-integrated density measurements from the central TCI chord as a function of time.

A two-color interferometer (TCI) is used on C-Mod to measure line-integrated density along 10 vertical chords in the core plasma region. [21] In order to compare TS

results with the TCI measurements, TS profiles are integrated along any chosen TCI chord. First, a TCI chord's grid is mapped by the EFIT code along the contours of the constant poloidal flux to the midplane outer radius. Second, a TS density profile is interpolated onto this grid and integrated over it. The result of such analysis is shown in the Fig. 3-10. Line-integrated density from the TCI (solid line) is in good agreement with the integrated TS profile (dashed line).

References for Chapter 3

[1] J. Sheffield, Plasma Scattering of Electromagnetic Radiation (Academic Press, New York, 1975).
[2] I. H. Hutchinson, Principles of plasma diagnostics, 2nd ed. (Cambridge University Press, 2002).
[3] R. Watterson and K. Chen, Rev. Sci. Instrum. **61**, 2867 (1990).
[4] D. A. Mossessian, A. Hubbard, and J. Irby, Rev. Sci. Instrum. **70**, 759 (1999).
[5] J. W. Hughes *et al.*, Rev. Sci. Instrum. **74**, 1667 (2003).
[6] N. P. Basse *et al.*, "Diagnostics Systems on Alcator C-Mod", Fusion Sci. Technol. **51**, 476 (2007).
[7] Continuum. *Operation and Maintenance Manual for the Powelight 9030 Series Laser.* Santa Clara, CA, October 1993.
[8] L. Lao, H. John, R. Stambaugh, A. Kellman, and W. Pfeiffer, Nucl. Fusion **25**, 1611 (1985).
[9] T. N. Carlstrom *et al.*, Rev. Sci. Instrum. **61**, 2858 (1990).
[10] *User Manual General Atomic Polychromator Model GAPB-1064-4-1K*, by T. N. Carlstrom, General Atomics, San Diego, CA, October 1999.
[11] H. Rohr, Phys. Lett. A **60,** 185 (1977).
[12] J. Howard, B. W. James, and W. I. B. Smith, J. Phys. D **12**, 1435 (1979).
[13] F. Flora and L. Giudicotti, Applied Optics **26**, No. 18, 4001 (1987).
[14] H. Rohr, Phys. Lett. A **81**, 451 (1981).
[15] E. Thomas Jr. *et al.*, Calibration of the ORNL two-dimensional Thomson scattering system, ORNL/TM-9507 (1985).
[16] W. T. Change, D. P. Murphy, and H. R. Griem, Phys. Lett. A **72A**, 341 (1979).
[17] K. Zhurovich *et al.*, Rev. Sci. Instrum. **76**, 053506 (2005).
[18] P. J. O'Shea, A.E. Hubbard, and Alcator C-Mod group, in *Proc. 9th Joint Workshop on ECE and ECH*, Borrego Springs, CA, Jan23-26, 1995, pp393-401.
[19] E. S. Marmar *et al.*, Rev. Sci. Instrum. **72**, 940 (2001).
[20] E. S. Marmar, J. E. Rice, J. L. Terry, and F. H. Seguin, Nucl. Fusion **22**, 1567 (1982).
[21] J. H. Irby, E. S. Marmar, E. Sevillano, and S. M. Wolfe, Rev. Sci. Instrum. **59**, 1568 (1988).

Chapter 4

4 Microturbulent drift instabilities

Microinstabilities are a class of instabilities with a wavelength comparable to the ion Larmor radius. Drift instabilities are a particularly important class of microinstabilities that have often been considered as the source of plasma turbulence and responsible for anomalous transport in tokamaks. The term "drift" takes its origin from various drift mechanisms which give rise to charge separation and therefore, lead to E×B convection. These modes are essentially electrostatic in nature, which means that magnetic field perturbations are not important. They result from temperature and/or density gradients in the plasma which serve as a source of the free energy. The geometry of the confining magnetic field often plays an important role because of the nature of the drift mechanisms and their effect on the resultant instability. Trapped and passing particles in a tokamak behave differently in the electrostatic potential perturbations. Therefore, different dispersion relations are obtained, depending on whether passing or trapped particle dynamics is dominant. Collisions might play an important role since they scatter trapped particles into the passing domain and vice versa. Moreover, trapping can be neglected when the mode frequency exceeds the particle bounce frequency. Typical examples of passing particle instabilities would be those driven by ion temperature gradient (ITG) or electron temperature gradient (ETG) while the most commonly considered trapped particle instability is trapped electrons modes (TEM). The next few sections will provide some basic insight into these instabilities with respect to

the conditions for the instabilities and their driving mechanisms, primarily focusing on ITG modes.

4.1 Simple physics of toroidal temperature gradient driven instability

The toroidal ITG mode has ballooning structure and is primarily driven by bad curvature effects. The ∇B and curvature drifts can be combined into the toroidal drift [1, Ch. 2.6]

$$\mathbf{v}_d = \frac{\mathrm{v}_{\|}^2 + \mathrm{v}_{\perp}^2/2}{\Omega B^2}\mathbf{B}\times\nabla B. \qquad (4.1)$$

Consider a pressure perturbation on a flux surface on the outer midplane of the tokamak as shown in Fig. 4-1. For a chosen magnetic configuration the ion drift velocity is down while the electrons drift up. Because drift velocity $\mathbf{v}_d$ depends on particle velocity or conversely, temperature, hot particles will drift faster than the cold particles. This increases the density below the hot areas and above the cold areas, primarily due to ions. The ion density perturbation produced by $\mathbf{v}_d$ in turn creates a potential perturbation, which results in the electric field as shown. This electric field induces $\boldsymbol{E}\times\boldsymbol{B}$ drift in the radial direction, which convects hotter plasma from the core region into the hot spots and colder plasma from the edge region into the cold spots, thus causing the perturbation to grow. On the inner midplane ("good curvature" region), however, ∇p and ∇B point into the opposite directions and now $\boldsymbol{E}\times\boldsymbol{B}$ convection brings hotter plasma into the cold spots and vice a versa, thus damping the perturbation.

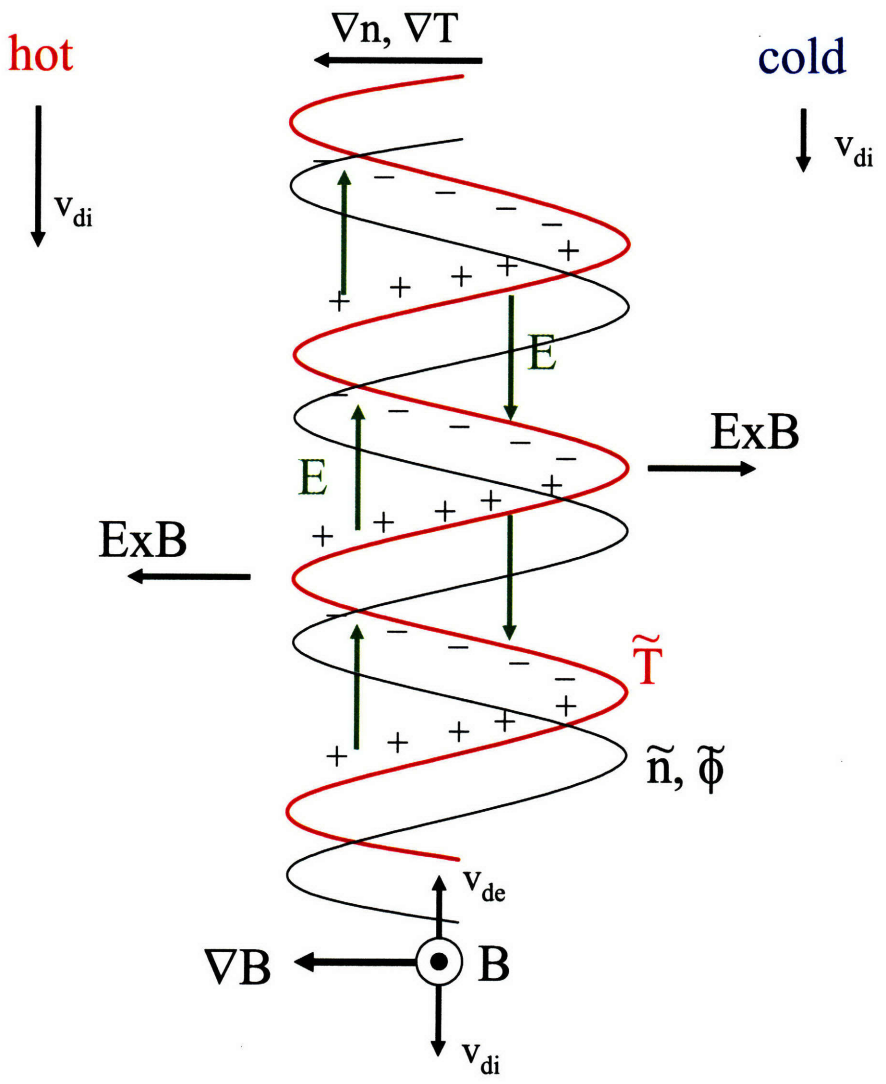

Figure 4-1 (Expanding on Ernst, Hammett picture): Simple physical picture of the toroidal ITG instability. Consider a temperature perturbation on the outer midplane of a tokamak. The velocity dependence of the toroidal drift produces ion density build-up above the cold spots and below the hot spots, which induces an electric field. The resultant *E×B* drift convects hot plasma into the cold area and vice versa, casing the instability to grow. On the inner midplane of a tokamak ∇p and ∇B point to the opposite directions and the initial perturbation is damped.

4.2 ITG growth rate

Gyrokinetic equations describe plasma processes which are slow compared to the Larmor frequency and which vary slowly in space compared to the Larmor radius. They

are usually derived from the Vlasov equation through averaging over the gyro-motion which reduces the equation's dimensionality.

In the following we develop a basic understanding of what the conditions for the ITG instability are and what the main driving mechanism is when this mode is unstable. Our derivation of the ITG instability will closely follow the one done by Hammett in Ref. [2]. Let's start with the electrostatic gyrokinetic equation written for the full, gyro-averaged, guiding center density $\bar{f}(R, \mathrm{v}_{||}, \mu, t)$

$$\frac{\partial \bar{f}}{\partial t} + (\mathrm{v}_{||}\hat{b} + \mathbf{v}_E + \mathbf{v}_d)\cdot\nabla\bar{f} + (\frac{q}{m}E_{||} - \mu\nabla_{||}B + \mathrm{v}_{||}(\hat{b}\cdot\nabla\hat{b})\cdot\mathbf{v}_E)\frac{\partial \bar{f}}{\partial \mathrm{v}_{||}} = 0 \tag{4.2}$$

where $\mathbf{v}_E = -\frac{c}{B}\nabla\tilde{\Phi}\times\hat{b}$ is the $\boldsymbol{E}\times\boldsymbol{B}$ drift velocity caused by the electrostatic potential perturbations, $E_{||} = -\hat{b}\cdot\nabla\tilde{\Phi}$ is the parallel electric field, $\mathbf{v}_d = \frac{\mathrm{v}_{||}^2}{\Omega}\hat{b}\times(\hat{b}\cdot\nabla\hat{b}) + \frac{\mu}{\Omega}\hat{b}\times\nabla B$ is the combined toroidal and curvature drift velocity, and $\mu = \frac{\mathrm{v}_{\perp}^2}{2B}$ is the magnetic adiabatic invariant. Following the standard convention, tilde denotes perturbed quantities. Here the equilibrium $\boldsymbol{E}\times\boldsymbol{B}$ flow is not included, since its primary effect will be to introduce a shift into the mode's frequency. Now we linearize the equation by breaking the full distribution function into the equilibrium and perturbation components: $\bar{f} = F_0 + \tilde{f}$. F_0 is the equilibrium part of the distribution function which satisfies the equilibrium equation and has a Maxwell form. The next step in the linearization procedure is to obtain the next order equation for the perturbed component of the distribution function. It has the form

$$\frac{\partial \tilde{f}}{\partial t} + (\mathrm{v}_{\|}\,\hat{b} + \mathbf{v}_d)\cdot\nabla\tilde{f} - \mu\nabla_{\|}B\frac{\partial \bar{f}}{\partial \mathrm{v}_{\|}} = -\mathbf{v}_E\cdot\nabla F_0 - (\frac{q}{m}E_{\|} + \mathrm{v}_{\|}(\hat{b}\cdot\nabla\hat{b})\cdot\mathbf{v}_E)\frac{\partial F_0}{\partial \mathrm{v}_{\|}} \tag{4.3}$$

We can rewrite this using Fourier transformation as follows

$$(-i\omega + i\,\mathrm{v}_{\|}\,k_{\|} + i\mathbf{v}_d\cdot\bar{k}_{\perp})\tilde{f} = -\mathbf{v}_E\cdot\nabla F_0 - (\frac{q}{m}E_{\|} + \mathrm{v}_{\|}(\hat{b}\cdot\nabla\hat{b})\cdot\mathbf{v}_E)\frac{\partial F_0}{\partial \mathrm{v}_{\|}} \tag{4.4}$$

It is convenient to introduce certain drift frequencies to rewrite Eq. (4.4) in a more intuitive way. $\omega_* = \bar{k}\cdot\mathbf{v}_* = -k_\theta\,\mathrm{v}_t\frac{\rho}{L_n} = -\frac{cT}{eB}\frac{k_\theta}{L_n}$ is the diamagnetic drift frequency, where $L_n = \left(\frac{\nabla n_0}{n_0}\right)^{-1}$ is the characteristic density scale length. Using this we can also define $\omega_*^T = \omega_*[1+\eta(\mathrm{v}_{\|}^2/2\,\mathrm{v}_t^2 + \mu B/\mathrm{v}_t^2 - 3/2)]$, where $\eta = \frac{L_n}{L_T}$. Let's also introduce the toroidal drift frequency $\omega_d = \bar{k}\cdot\mathbf{v}_d = -\frac{\mathrm{v}_t\,\rho}{R}(k_\theta\cos\theta + k_r\sin\theta)$ and define $\omega_{dv} = \omega_d(\mathrm{v}_{\|}^2 + \mu B)/\mathrm{v}_t^2$.

The sign convention is consistent with the geometry depicted in Fig. 4-2. If we concentrate on the outer midplane where the curvature is bad, then θ = 0 and $\omega_d = -k_\theta\rho\,\mathrm{v}_t/R$.

In these notations Eq. (4.4) can be rewritten as

$$(-i\omega + i\,\mathrm{v}_{\|}\,k_{\|} + i\mathbf{v}_d\cdot\bar{k}_{\perp})\tilde{f} = -i(-\omega_*^T + \omega_{dv} + \mathrm{v}_{\|}\,k_{\|})\frac{e\tilde{\Phi}}{T}F_0, \tag{4.5}$$

which can be solved for $\tilde{f}$ to yield

$$\tilde{f} = \frac{-\omega_*^T + (\omega_{dv} + \mathrm{v}_{\|} k_{\|})}{\omega - (\omega_{dv} + \mathrm{v}_{\|} k_{\|})} \frac{e\tilde{\Phi}}{T} F_0 . \tag{4.6}$$

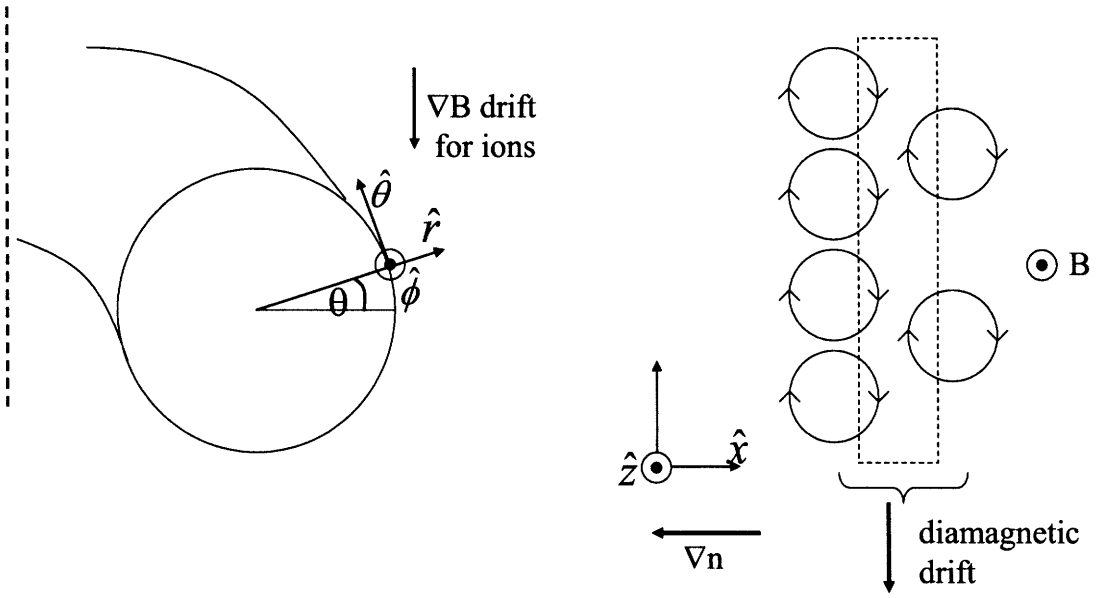

Figure 4-2: Sign conventions for various drifts. For a chosen geometry ∇B for ions is downward. On the outer midplane where ∇n is inward the diamagnetic drift is also downward.

We are interested in the modes with $k_{\|} \mathrm{v}_{ti} << \omega, \omega_*^T, \omega_{dv} << k_{\|} \mathrm{v}_{te}$.

Because of the low inertia, electrons flow rapidly along the field lines, generating parallel electric field satisfying force balance given by $neE_{\|} + \nabla_{\|} p_e = 0$. Linearizing this equation leads to a relation between the perturbed electron density $\tilde{n}$ and electrostatic potential $\tilde{\Phi}$: $\frac{\tilde{n}_e}{n_{e0}} = \frac{e\tilde{\Phi}}{T}$, which is also known as the Boltzman distribution. We also need the quasineutrality condition $\tilde{n}_e = \tilde{n}_i$, which using Eq. (4.6) can be expressed as:

$$n_{e0} \frac{e\tilde{\Phi}}{T_{e0}} = \int d^3 \mathrm{v} \frac{-\omega_*^T + \omega_{dv}}{\omega - \omega_{dv}} \frac{e\tilde{\Phi}}{T_{i0}} F_0 . \tag{4.7}$$

Using a "cold plasma" or "fast wave" approximation ($\omega >> \omega_{dv}$) we can do Taylor expansion of the denominator in the Eq. (4.7). Hammett [2] shows that this leads to an equation which defines the dispersion relation

$$\frac{T_{i0}}{T_{e0}} = 2\frac{\omega_d}{\omega} - \frac{\omega_*}{\omega} + 7\frac{\omega_d^2}{\omega^2} - 2\frac{\omega_d \omega_* (1+\eta)}{\omega^2}. \qquad (4.8)$$

Consider the flat density limit, which is a good approximation for Alcator C-Mod H-mode plasmas. In this case $\nabla n \rightarrow 0$, but ∇T is finite. Under these conditions $\eta \rightarrow \infty$, and $\omega_* \rightarrow 0$ and the dispersion relation (4.8) becomes

$$\omega^2 \frac{T_{i0}}{T_{e0}} - 2\omega_d \omega + 2\omega_d \omega_*^T - 7\omega_d^2 = 0, \text{ which can be solved for } \omega$$

$$\omega = \frac{2\omega_d \pm \sqrt{4\omega_d^2 - 4\tau(2\omega_d \omega_*^T - 7\omega_d^2)}}{2\tau}, \qquad (4.9)$$

where $\tau = T_{i0} / T_{e0}$.

In order for the instability to grow/damp, its frequency should have an imaginary part, which will define the growth/damping rate. Consider the large temperature gradient limit ($\omega_*^T \sim \nabla T >> 1$). In this case the growth rate is given by

$$\gamma = \sqrt{\frac{2\omega_d \omega_* \eta}{\tau}} = \sqrt{\frac{2\omega_d \omega_*^T}{\tau}} = \frac{\sqrt{2} k_\theta \rho_i}{\sqrt{\tau}} \frac{v_{ti}}{\sqrt{RL_T}}. \qquad (4.10)$$

It is interesting to note that the term $\frac{v_{ti}}{\sqrt{RL_T}}$ appears in the ITG growth rate, since it is a fundamental scaling of all bad-curvature driven instabilities. Expression (4.10) illustrates that for given global plasma parameters, the instability's growth rate is

determined by and can be changed through the local temperature gradient scale length L_T. Steepening temperature profile reduces the L_T parameter and drives the mode unstable.

4.3 Thresholds

The general dispersion relation (4.14) can be rewritten as

$$\omega = \frac{2\omega_d \pm \sqrt{(4+28\tau)\omega_d^2 - 8\tau\omega_d\omega_*^T}}{2\tau} \tag{4.11}$$

It is clearly seen that in order for instability to exist we need to have $\omega_d\omega_*^T > 0$. This is a necessary (but not sufficient) condition for instability, since other terms inside the square root in (4.11) are positive. From this condition, it is clearly seen from the definitions of ω_d and ω_*^T that ∇p and ∇B must point in the same direction for instability (which is true on the "bad" curvature side), and if they are antiparallel ("good" curvature side) the mode is stable. Because $\omega_* = -k_\theta\rho_i \mathrm{v}_{ti}/L_{ni}$ and $\omega_d = -(\rho_i \mathrm{v}_{ti}/R)(k_r \sin\theta + k_\theta \cos\theta)$, perturbations on the outer midplane of the torus (θ = 0) are unstable, while perturbations on the inner midplane (θ = π) are stable. Fig. 4-1 illustrates this once again. The dispersion relation (4.11) also means that the following condition $8\tau\omega_d\omega_*^T > (4+28\tau)\omega_d^2$ is required for instability. This condition can be rewritten as $\frac{R}{L_T} > \frac{1}{2}\left(7+\frac{T_e}{T_i}\right)$. This demonstrates that there is a critical gradient threshold R/L_{T_CRIT}, which determines whether the mode is driven unstable. However, it gives the wrong dependence on T_i/T_e because of the Taylor expansion of the resonant

denominator in (4.7). This expansion breaks down near marginal stability, since in this case $\omega \sim \omega_d$. In a more general case the parameter which determines the mode stability is η_i, defined above as the ratio of density to temperature scale lengths. That is why the ITG mode is sometimes referred to as "η_i mode". Romanelli and Briguglio [3] show that with a more careful treatment including kinetic ion response, the critical value of this parameter for the flat density profile limit is given by

$$\eta_i^{crit} = \frac{4}{3}\left(1+\frac{T_i}{T_e}\right) \tag{4.12}$$

A more general result for the threshold for instability is given by Jenko *et al.* [4]

$$\frac{R}{L_T^{crit}} = Max\left(\left(1+\frac{T_i}{T_e}\right)\left(1.33+1.91\frac{\hat{s}}{q}\right)\left(1-1.5\frac{r}{R}\right)\left(1+0.3\frac{rd\kappa}{dr}\right), 0.8\frac{R}{L_n}\right), \tag{4.13}$$

where $\hat{s} = (r/q)(dq/dr)$ is the magnetic shear, and κ is the plasma elongation. This parameterization is found empirically by fits to many gyrokinetic stability calculations. Wesson [1, Ch. 8.3] provides another expression for the instability threshold

$$\eta_i^{crit} = \begin{cases} 1.2, & \varepsilon_n < \varepsilon_{nc} \\ \frac{4}{3}(1+\tau)(1+2\hat{s}/q)\varepsilon_n, & \varepsilon_n > \varepsilon_{nc} \end{cases} \tag{4.14}$$

where $\varepsilon_n = L_n / R$ and $\varepsilon_{nc} = \dfrac{0.9}{(1+\tau)(1+2\hat{s}/q)}$. This expression demonstrates once again that when the density profile is sufficiently flat the threshold becomes a critical temperature gradient rather than a critical η_i.

It is instructive to go back and take a closer look at the dispersion relation. Beer [5] retains the polarization drift, in which case the perturbed electron and ion densities are

related by $\tilde{n}_e = \tilde{n}_i - b\frac{e\tilde{\Phi}}{T_{i0}}n_{i0}$, where $b = k_\perp^2\rho_i^2$. He obtains the dispersion relation in a similar form

$$\omega = \frac{3\omega_d(\tau+b)+\omega_d}{(\tau+b)} \pm \frac{\sqrt{3\omega_d^2(\tau+b)^2+\omega_d^2-2\omega_d\omega_*\eta_i(\tau+b)}}{(\tau+b)} \qquad (4.15)$$

It shows the stabilizing effect of $T_i > T_e$ ($\tau > 1$) both in the threshold for the stability and in the growth rate. The former is true because the stabilizing term $3\omega_d^2(\tau+b)^2$ increases faster with τ than the destabilizing term $-2\omega_d\omega_*\eta_i(\tau+b)$, and the latter is true because the $(\tau+b)$ in the denominator dominates the $\sqrt{\tau+b}$ from the drive. The stabilizing effect of $T_i > T_e$ occurs by reducing the ion density perturbation produced by $\tilde{\Phi}$, weakening the feedback mechanism that causes instability. In addition, Eq. (4.15) shows the stabilizing influence of finite Larmor radius (FLR) effects through b. Physically FLR stabilization occurs because the ions feel the averaged potential around their gyro-orbits, and this gyro-averaging reduces the response to high $k_\perp\rho_i$ components of the potential perturbation. In the large η_i limit Eq. (4.15) gives the same (to within FLR correction) expression (4.10) for the instability growth rate.

4.4 Electron (ETG/TEM) modes

There is another passing particle instability, which is driven by electron temperature gradient. Therefore, it is called electron temperature gradient (ETG), or "η_e" mode. It is similar to the ITG mode, but the roles of the ions and electrons are reversed. The perpendicular wavelength of this mode satisfies $\rho_e < \lambda < \rho_i$. Thus $k_\perp\rho_i >> 1$ and

in this case it is the ion response that satisfies a Boltzmann distribution $\frac{\tilde{n}_i}{n_{i0}} = \frac{e\tilde{\Phi}}{T}$. The derivation of the ETG mode is the same as above for the ITG mode, because the electron response is calculated from the gyrokinetic equation in a similar way as it was done for the ITG mode but with subscripts i replaced by e. Expression (4.13) for the critical temperature gradient remains the same, but with subscripts i and e interchanged. The difference between the ITG and ETG mode is that for the ITG mode electrons are often viewed as adiabatic because of their fast parallel motion, so there is no perturbed parallel electron flow. Therefore, there is no significant perturbed parallel current to drive the magnetic perturbations. Electromagnetic perturbations however may be important for the electron heat transport.

Trapped particles behave differently from passing particles, because they effectively average out their parallel motion over a bounce period. Also they spend most of their time in the bad curvature region on the outboard side of the tokamak, which makes them susceptible to ballooning-type instabilities. By considering plasma oscillations with sufficiently slow phase velocity we can illustrate the essential characteristics of the trapped particle instability. An initial density perturbation with $k_{||} \approx 0$ is shown in Fig. 4-3. Because trapped particles spend most of their time on the outer side, the curvature drift has a preferred direction for each species. It is again in the opposite direction for ions and electrons which results in the polarization shown in the picture. The induced local electric field drives $\boldsymbol{E}\times\boldsymbol{B}$ flows which enhance the initial perturbation causing the instability. This is the collisionless trapped particle mode, for

which FLR effects are not important. The trapped particle response to the electrostatic perturbation is described by the drift kinetic equation.

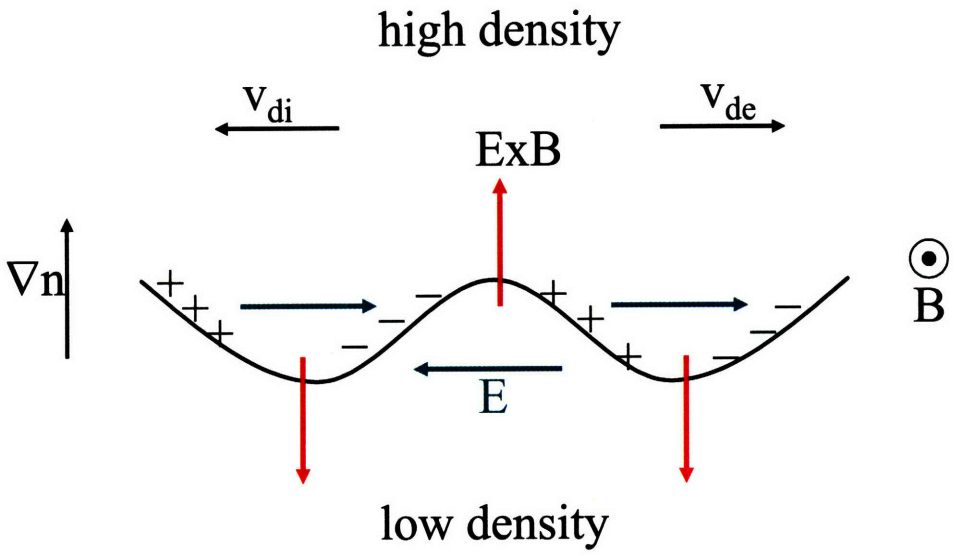

Figure 4-3 (adapted from Wesson): The physical mechanism of the trapped particle instability. Since trapped particles spend most of their time on the outer side of a tokamak their curvature drift has preferred direction. This causes charge separation and induces electric field. The resultant *E*×*B* flow enhances initial density perturbation.

Along similar lines, assuming quasineutrality and doing proper averaging over the trapped particle bounce orbits, the dispersion relation is derived [1, Ch. 8.4]

$$\frac{1}{\sqrt{2\varepsilon}}\left(\frac{1}{T_i}+\frac{1}{T_e}\right)=\frac{1}{T_i}\frac{\omega-\omega_{*i}}{\omega-\omega_{di}}+\frac{1}{T_e}\frac{\omega-\omega_{*e}}{\omega-\omega_{de}}, \qquad (4.16)$$

where the drift frequencies have been defined previously. If we assume $T_i = T_e$ which is usually a good assumption for C-Mod plasmas and $\omega_* >> \omega_d$ for each species, which is also relevant for the large aspect ratio limit, then the solution to this equation is given by

$$\omega^2 = \omega_{de}(\omega_{de} + \sqrt{2\varepsilon}\omega_{*e}). \qquad (4.17)$$

For a standard density profile which peaks towards the center ω_{*e} is positive while ω_{de} is negative, and instability then occurs for $\sqrt{2\varepsilon}\frac{R}{L_n} > 1$. This condition is similar to the one derived for the ITG mode, but density rather than temperature gradient appears here. The mode's growth rate is a function of ω_{*e} and ω_{de}. Therefore, the perturbed $\boldsymbol{E}\times\boldsymbol{B}$ and magnetic curvature drifts are important. Collisions become important when the effective collision frequency is of the same order as the relevant drift frequency. If this is the case, then trapped particles can be scattered through collisions into the passing domain and vice versa. But collision frequency must be low enough not to prevent the trapped particles from completing a banana orbit, i.e. $\nu_j < \varepsilon\omega_{bj}$, where ω_{bj} is the bounce frequency. The mode for which stability is determined only by trapped electron dynamics, but trapped ions do not play a role, is called dissipative trapped electron mode (TEM). As in the previous cases a similar derivation of this instability can be done [1, Ch. 8.4], which leads to $\gamma \sim \varepsilon^{3/2}\frac{\omega_{*e}^2}{\nu_e}\eta_e$ for the mode's growth rate. The major drive for this mode comes from the electron temperature gradient, although when $\eta_e \sim \varepsilon$ the magnetic curvature becomes important. Further studies [6] demonstrate that the TEM mode can be driven unstable predominately by the electron density gradient as well.

References for Chapter 4

[1] J. A. Wesson, *Tokamaks* (Oxford University Press, New York, NY, 1997).
[2] G. W. Hammett, CMPD/CMSO Winter School, UCLA, January 9, 2007.
[3] F. Romanelli and S. Briguglio, Phys. Fluids B **2**, 754 (1990).
[4] F. Jenko, W. Dorland, and G. W. Hammett, Phys. Plasmas **8**, 4096 (2001).
[5] M. A. Beer, "Gyrofluid models of turbulent transport in tokamaks", PhD Thesis, Princeton University, 1994.
[6] D. R. Ernst *et al.*, in Fusion Energy 2004 (*Proc. 20th IAEA Fusion Energy Conf., Vilamoura, 2004)* (Vienna: IAEA) CD-ROM file TH/4-1 and http://www-naweb.iaea.org/napc/physics/fec/fec2004/datasets/index.html.

Chapter 5

5 Experimental studies of ITB formation on C-Mod

As have been described in Chapter 2.3 of this thesis, recent ITB studies on Alcator C-Mod have concentrated on the scenario where ITBs are formed in off-axis ICRF heated discharges. [1, 2, 3] Under this scenario the plasma goes into EDA H-mode within a few energy confinement times after the application of ICRF heating power. The ITB appears spontaneously after the EDA H-mode starts and evolves on a longer time scale. These ITBs are marked by the peaking of electron density profiles, which happens without any central fuelling from neutral beam or pellet injections. Ions and electrons are well coupled in C-Mod H-mode plasmas due to the high density. All these factors make this regime relevant for reactor type scenarios.

Our hypothesis is that ICRF heated ITBs on C-Mod are formed as a result of competition between neoclassical inward pinch and outward diffusion primarily driven by microturbulent drift modes. During standard steady-state EDA H-mode operation, the inward Ware pinch is believed to be balanced or dominated by the outward diffusion, which can explain why the H-mode plasmas have relatively flat density profiles. Fig. 5-1(a) depicts a typical density profile during the steady-state H-mode phase. Circles and squares represent TS measurements from the core and edge systems, respectively. The solid line shows the fit to the data. Reducing the drive for the temperature gradient driven modes can suppress the outward diffusion. This can shift the balance in favor of the inward particle pinch and result in ITB formation and density profile peaking even without $\overline{E} \times \overline{B}$ shear or other stabilizing effects usually present on other machines. [4, 5]

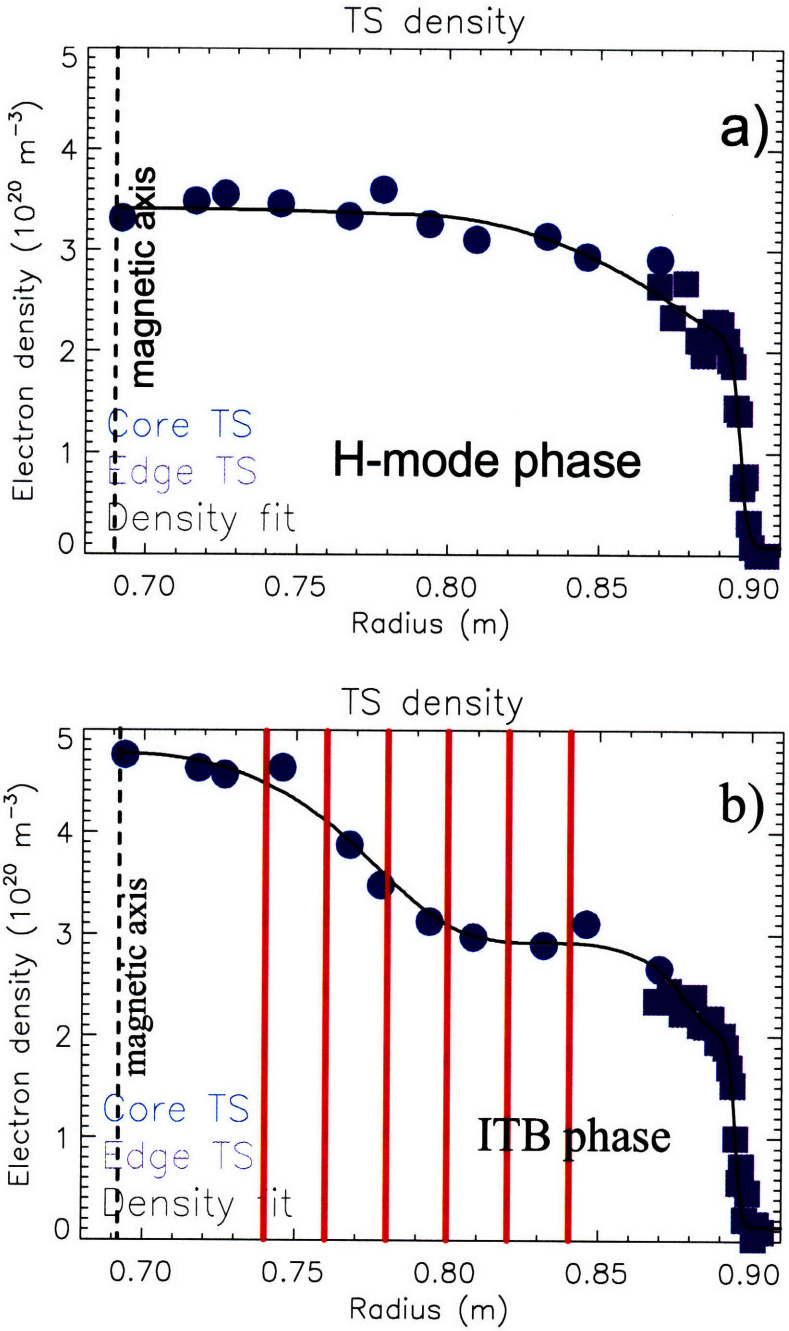

Figure 5-1: Typical C-Mod density profiles during a) steady-state H-mode phase and b) fully developed ITB phase. Circles and squares represent experimental measurements from the core and edge Thomson scattering diagnostics respectively, while solid line shows a fit to the experimental data. ITB foot is located at around R = 0.8 m, or r/a = 0.5. Vertical lines represent regions of interest for the temperature gradient analysis.

Fig. 5-1(b) shows the electron density profile in the fully developed ITB phase. The ITB is clearly distinguished with its foot located near R = 0.8 m, while the edge pedestal in this double barrier regime is located near R = 0.89 m. The working hypothesis is simply that broadening the temperature profile with off-axis ICRF suppresses toroidal ITG modes, which allows the neoclassical particle pinch to dominate the transport. Several sets of experiments were performed on the C-Mod tokamak to test this idea.

5.1 Magnetic field scan experiment

For a given ICRF frequency, the condition of achieving ICRF heated ITBs in C-Mod plasmas strongly depends on the magnetic field with small (if any) hysteresis. Given the one-to-one relation between ICRF frequency, the magnetic field, and thus the ICRF power deposition profile, this fact in turn suggests a strong dependence on the RF resonance location. [1] Fig. 5-2 illustrates this dependency once again. Density peaking is evaluated at 450 ms after the initiation of the ICRF pulse, which is enough to form an ITB. Green asterisks correspond to the discharges that did not develop ITBs, while red symbols depict ITB discharges. It is clearly seen that the threshold for achieving an ITB is that the location of the ICRF resonance be at $|r/a| \geq 0.5$ on either the high or low field side of the tokamak. It should be noted that it is difficult to analyze and compare discharges which differ by 0.1-0.2 T but are otherwise similar. Therefore, a systematic scan with wide range of magnetic fields is required in order to capture any trends with the ICRF resonance location.

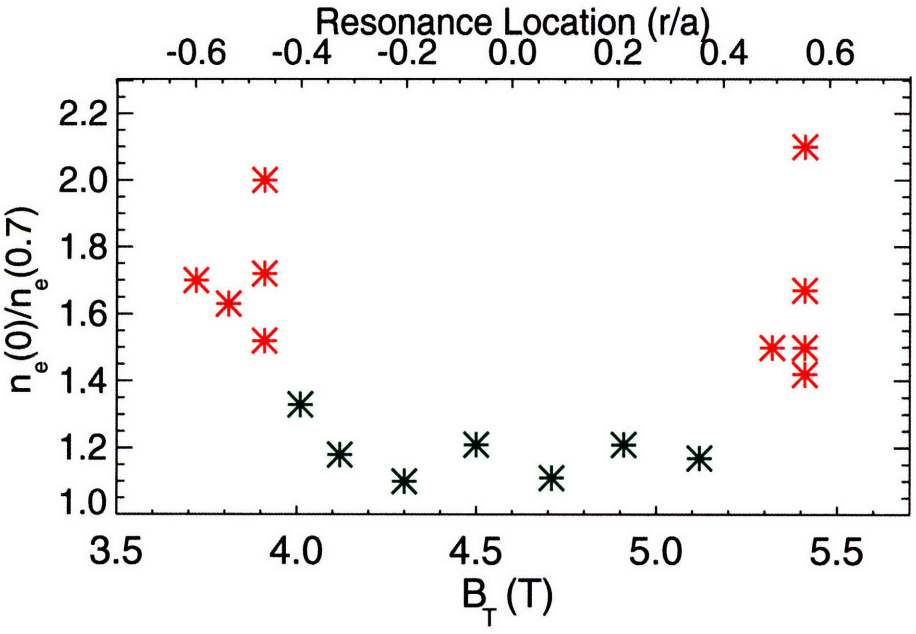

Figure 5-2: Density peaking factor as a function of toroidal magnetic field and the radial position of the ICRF resonance. The discharges shown in red had well established ITBs, while those shown in green did not. (Figure courtesy of J. Rice)

During the first set of experiments the toroidal magnetic field was varied between discharges from 5.45 T to 6.27 T, thus moving the ICRF resonance radially outward. In order to minimize other possible stabilizing effects, the total RF power was kept constant at 2.8 MW and the total plasma current was adjusted proportionally to the magnetic field (from 0.86 MA to 1 MA) to keep the safety factor q profile unchanged at $q_{95} = 4.5$. Also in order to avoid any possible hysteresis in machine performance, the sequence of the magnetic field was such that ITB discharges were followed by non-ITB ones and vice versa. Table 5-1 provides some global plasma parameters for these experiments. The ICRF antennas operated at 80 MHz, therefore the magnetic field scan resulted in a scan of the ICRF resonance position on the low field side from r/a ~ 0.1 up to r/a ~ 0.6. During these experiments a relatively sharp threshold in magnetic field for ITB formation was found, which is consistent with the previous C-Mod results. [1]

B_T (T)	I_P (MA)	q_{95}	ITB?
6.3	1.0	4.54	Yes
6.2	0.989	4.47	Yes
6.1	0.973	4.48	marginal
6.0	0.957	4.51	No
5.9	0.941	4.49	No
5.8	0.925	4.49	No
5.7	0.909	5.50	No
5.6	0.893	4.49	No
5.5	0.877	4.52	No
5.4	0.861	4.48	No

Table 5-1: Some of the global plasma parameters for the magnetic field scan experiments. Plasma current was adjusted proportionally to the magnetic field to keep q_{95} constant to mitigate possible effect of the magnetic shear. Discharges with higher magnetic field, which translates into more off axis heating, developed ITBs.

Figure 5-3 shows some of the plasma parameters for two representative discharges from this scan: a non-ITB (a) and an ITB (b) discharge. With the application of 2.8 MW of ICRF power at 0.6 s, the plasma immediately undergoes a transition from L-mode to EDA H-mode. In the discharge that does not develop an ITB, the density profile remains flat as can be judged by the density peaking ratio, while for the ITB discharge the density peaking factor rises starting at 1.2-1.3 s. Some back transitions occur during the initial phase of the H-mode during the ITB discharge; however these are not associated with the ITB formation. A rise in plasma stored energy is also observed during the ITB phase. $H_{ITER89P}$ factor reaches 1.1, which is just a marginal improvement

over the H-mode confinement. It is interesting to note that H factors are similar but slightly lower for the off-axis heated discharges than they are for the on-axis heated discharges. During the ITB phase the density is peaking in the core plasma region with the density profile during the fully developed ITB phase shown in Fig. 5-1(b).

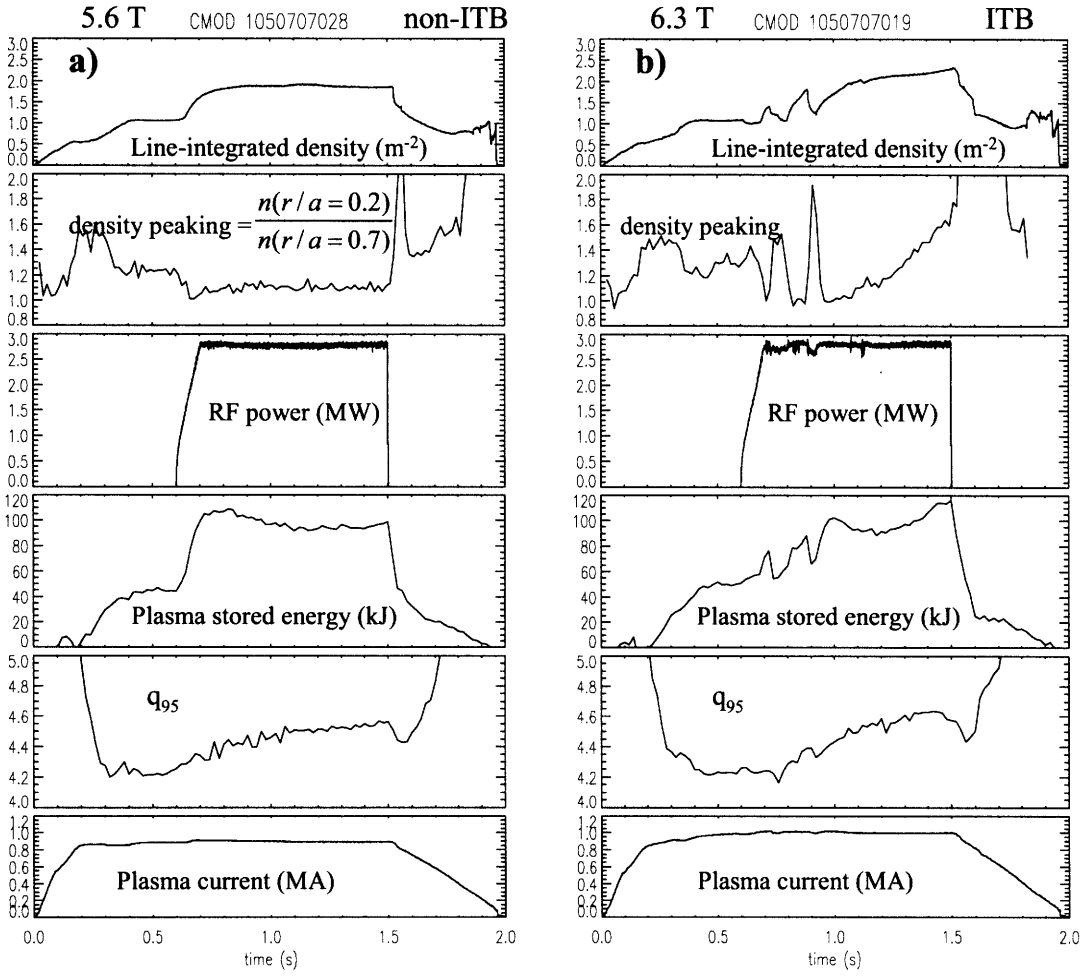

Figure 5-3: Selected plasma parameters for two representative discharges: non-ITB (a) and ITB (b), from the magnetic field scan experiment. During these experiments total ICRF power was kept constant and plasma current was adjusted proportionally to the magnetic field to keep q_{95} constant. Both discharges undergo L-H transition with an application of RF power. (a) Lower field translates into ob-axis heating with the ICRF resonance location at r/a ~ 0.15. Plasma remains in steady-state EDA H-mode regime. (b) Higher field results into more off-axis ICRF heating with the ICRF resonance location at r/a ~ 0.6 and plasma develops an ITB.

As have been shown in the previous chapter microturbulent drift modes become unstable if the η parameter exceeds some critical value, i.e. $\eta_{i,e} > \eta_{crit}$, where $\eta_{i,e} = L_n/L_T$ for ions or electrons correspondingly. In the flat density limit, $L_n >> L_T$, this criterion becomes a criterion on R/L_T rather than on η, and $R/L_T > R/L_{Tcrit}$ for instability, where

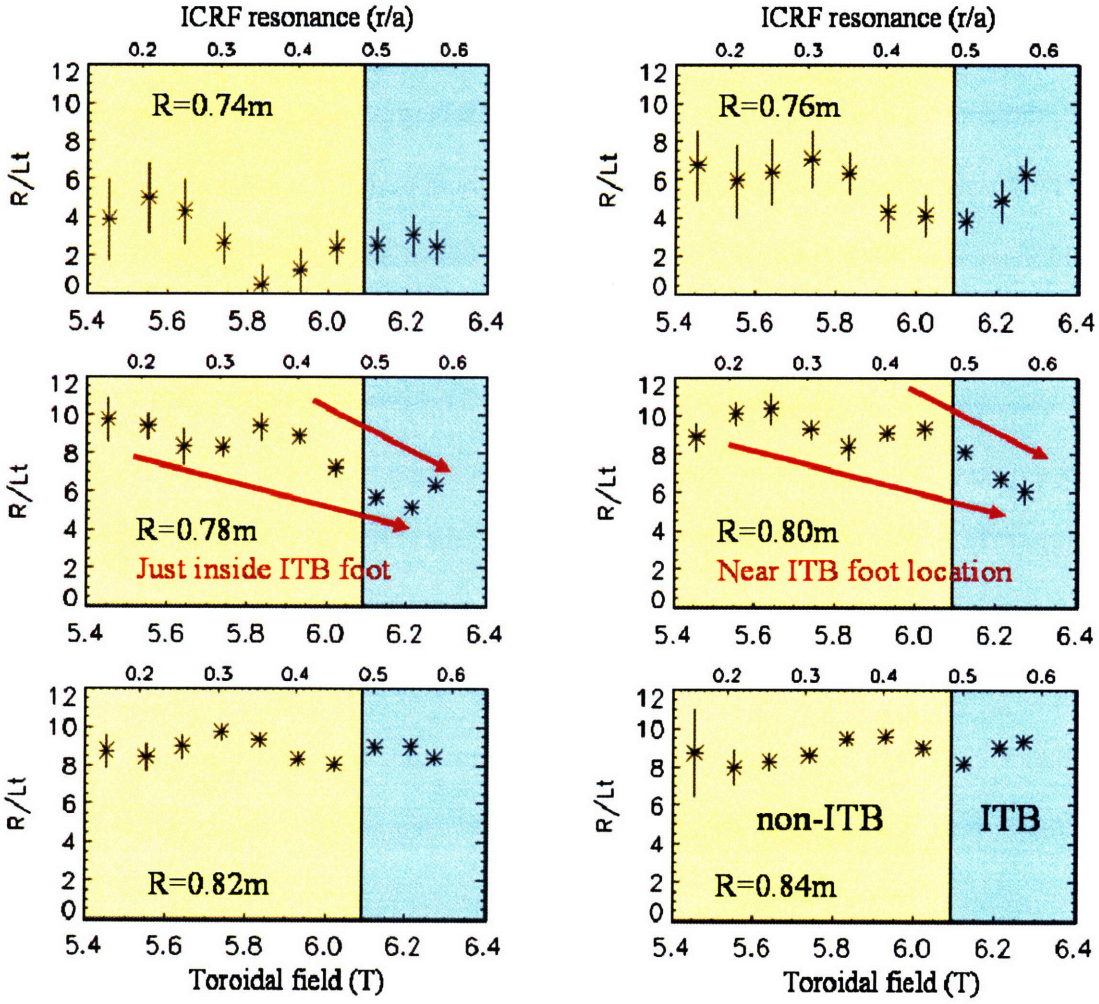

Figure 5-4: R/L_T for the electron temperature calculated at the indicated radial positions shown in Fig. 5-1(b). Averaging has been done over the steady portion of the discharge during the H-mode phase (pre-ITB for ITB discharges) and therefore, over many sawtooth oscillations. The yellow region on each plot corresponds to non-ITB discharges, while the blue region contains discharges that developed ITBs. For this experiment lower magnetic field translates into on-axis ICRF heating. The position of the ICRF resonance and therefore, the degree of "off-axis" heating is shown on the upper axis. While no systematic trend can be derived for inner or outer plasma regions, there is a downward trend for R/L_T at positions near or just inside ITB foot location as shown by the arrows.

$L_T^{-1} = \frac{1}{T}\frac{dT}{dr}$. In order to examine how the shift of the ICRF resonance location affects the temperature profiles, these R/L_T values were calculated at the radial locations marked in Fig. 5-1(b).

The results of this analysis are shown in Fig. 5-4. The electron temperature profiles were measured by the C-Mod 9-channel GPC ECE system. [6] The averaging of the gradient was done over steady portions of the discharges during the H-mode (pre-ITB for ITB cases) phase and therefore, over many sawtooth periods. Change in the magnetic field moves the ICRF resonance position, which is shown on the upper axis of each plot. No trend for R/L_T can be inferred for the inner or outer radial chords. On the contrary, the analysis of the temperature scale lengths at radial positions near or just inside the ITB foot suggests that there is a decrease in R/L_T for discharges that develop ITBs compared to non-ITB discharges. The pre-ITB values of R/L_T for ITB discharges at these radial positions are systematically lower than those from all non-ITB discharges.

Sawtooth oscillations might play an important role in setting the temperature gradient, since they redistribute the heat inside plasma core through magnetic reconnections. During these reconnections the plasma temperature profile crashes in the core region on a very fast time scale with a subsequent slower rise to approximately pre-crash values. Sawtooth oscillations are clearly seen by ECE systems and other diagnostics which measure temperature dependent plasma parameters. Sawteeth temporarily flatten the plasma temperature profile inside a certain radius and steepen the profile just outside it. This radius is called the sawtooth inversion radius and can be loosely defined as the location where the impact of the crash on the temperature profile changes sign. The sawtooth inversion radius in C-Mod plasmas is usually at $r/a \sim 0.2$ and

is well inside the ITB foot. In order to investigate the effect on the plasma temperature profile and therefore, the possibility of affecting the stability of the temperature gradient modes, a similar exercise was done and the R/L_T values at different stages of a sawtooth crash were calculated. For this, each sawtooth period is divided into 10 bins and the averaging within each bin is done throughout the steady portion of the H-mode.

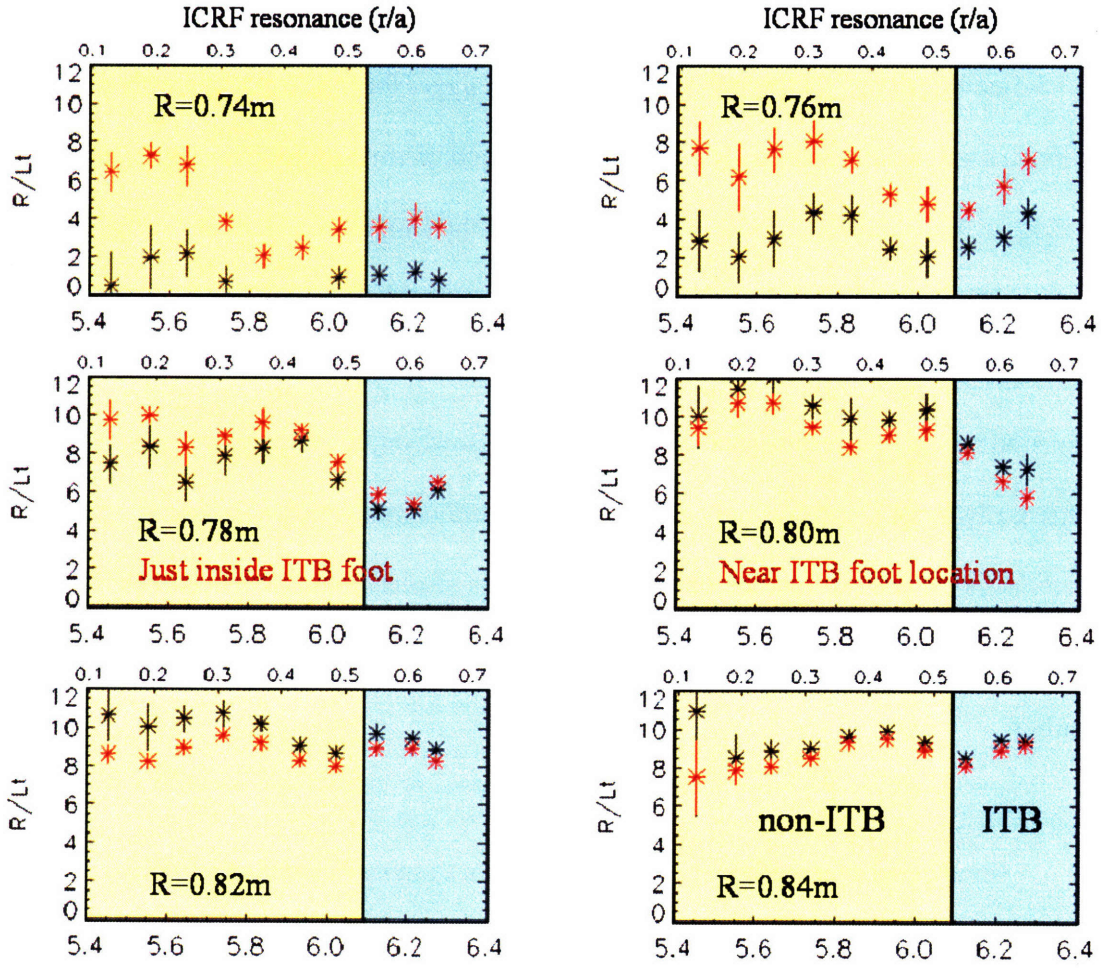

Figure 5-5: R/L_T values for the electron temperature calculated at the indicated radial positions shown in Fig. 5-1(b) and for times corresponding to before (red) and after (black) sawtooth crashes. Each sawtooth period within a time window of a steady phase of the H-mode (pre ITB for ITB discharges) is divided into 10 phases. Averaging has been done over these sawtooth phases.

The results for two extreme cases, corresponding to just before and after the sawtooth crash are shown in Fig. 5-5. In this figure R/L_T values for the electron temperature are plotted for the same radial positions as in Fig. 5-4. Data plotted in red asterisks correspond to pre-crash profiles, while black asterisks show post-crash values. The trend that R/L_T values systematically decrease near or just inside the ITB foot position as the ICRF resonance is moved outward is preserved and is independent of the sawtooth phase. Fig. 5-5 demonstrates that the effect of sawteeth is bigger for the discharges with on-axis heating as one would expect. The size of the sawtooth perturbations is larger for central heating. It also enables us to estimate the extent of the temperature gradient variation due to sawtooth oscillations and shows that the difference between pre-sawtooth crash and post-crash values can be up to a factor of 2 or 3 well inside the ITB. The sawtooth inversion radius for these shots is at $R \approx 0.76$ cm. However, the radial resolution of either x-ray or ECE systems only allows us to determine it to within a couple of centimeters. It is important to note that the previous results of similar discharges [2] suggested that the sawtooth mixing radius is larger for the discharges with on-axis heating.

Another set of experiments was done with an even more extensive toroidal magnetic field scan, where the magnetic field was varied from 3.7 T to 5.4 T on a discharge-by-discharge basis. With the ICRF system operating at 70 MHz, that resulted in the scan of the ICRF resonance location from the high to low field side, $-0.5 \leq r/a \leq 0.5$. For this set of discharges, some limited ion temperature profile information was available from the x-ray (HIREX) system [7] with the central temperature derived from

the neutron rate diagnostic [8]. The results of these measurements are shown in Fig. 5-6. Circles correspond to the central ion temperature as measured by the neutron rate system, whereas dots represent $T_i(0)$ measurement from the HIREX system. From Fig. 5-6 one can tell that there is a good agreement between these two diagnostics.

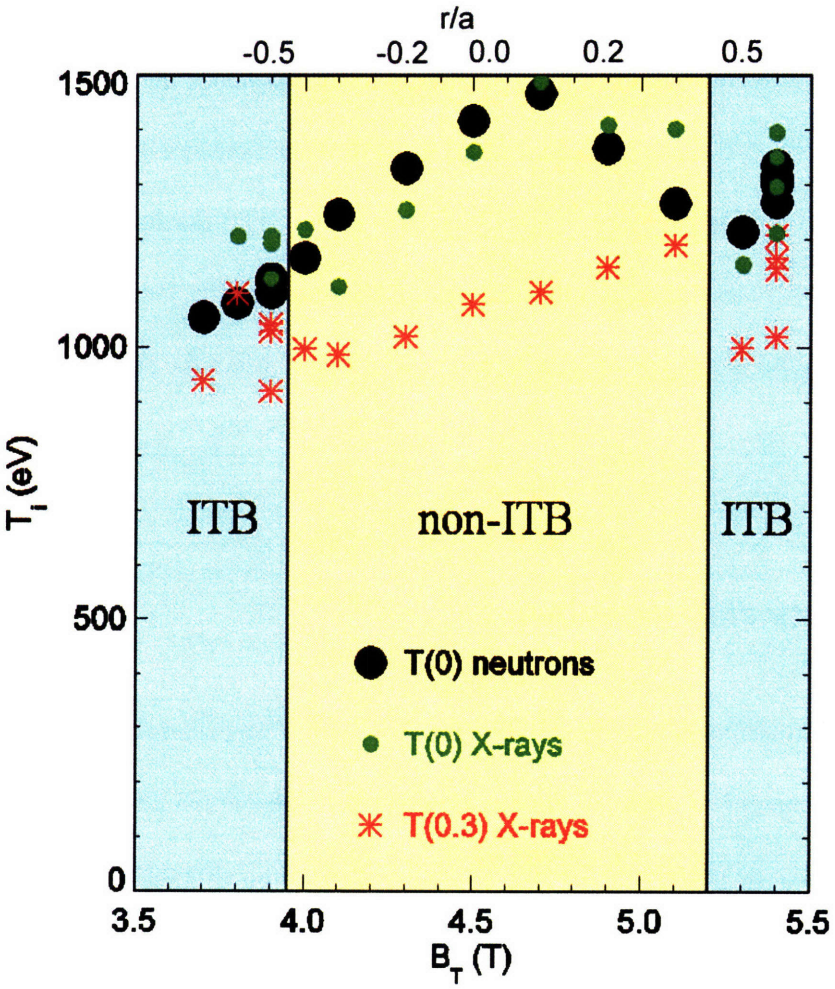

Figure 5-6: Ion temperature measurements for the magnetic field scan experiments. Circles are the central values of ion temperature derived from neutron rate measurements. Dots correspond to the central ion temperature as measured by x-ray (HIREX) diagnostic. Asterisks represent HIREX T_i measurements at r/a = 0.3. The ventral region corresponds to non-ITB discharges while the left and right regions contain data from the discharges that developed ITBs. The position of the ICRF resonance and therefore, the degree of "off-axis" heating is shown on the upper axis. Since there is bigger gap between on- and off-axis T_i values for non-ITB discharges, this means that ion temperature profile gets flatter as the ICRF resonance is moved off-axis.

Asterisks depict off-axis ion temperature measurements done by the HIREX diagnostic at r/a = 0.3. The left and right blue regions correspond to the discharges which developed an ITB. The r/a position of the ICRF resonance in each case and therefore, the degree of "off-axis" heating is shown on the upper axis. For the discharges, where an ITB formed, the ICRF resonance position was at $|r/a| \geq 0.5$ on HFS or LFS. The yellow region in the middle contains data from the non-ITB discharges with the ICRF resonance location inside $|r/a| = 0.5$. From Fig. 5-6 it can be deduced that the difference between $T_i(0)$ and $T_i(0.3)$ is smaller for ITB discharges (blue regions) than it is for non-ITB discharges (central region). This observation suggests that the ion temperature profiles get flatter as the ICRF resonance location is moved off axis, which in turn might affect the stability of the ITG modes.

5.2 ICRF frequency shift experiments

Finally a set of experiments was done where the ICRF setup was changed during a shot at a fixed toroidal magnetic field. A combination of D&E and J antennas operating at different frequencies can be used to control the amount of power injected into the plasma at a certain frequency. This provides an alternative method to change the ICRF heating location. These experiments were done with constant $B_T = 5.6$ T and therefore, 80 MHz operation corresponded to on-axis heating, while 70 MHz corresponded to off-axis LFS heating. Some of the plasma parameters from a selected discharge are shown in Fig. 5-7. In this case the application of ICRF heating starts with the 80 MHz D&E antennas, triggering an EDA H-mode. 150 ms into the H-mode phase of the discharge,

the 80 MHz power is gradually traded over a 150 ms window for 70 MHz off-axis heating from J-port antenna with the total ICRF power kept constant at 1.5 MW. The rest of the discharge is continued with 100% off-axis heating. An ITB develops during this phase of the H-mode as can be seen on Fig. 5-7 from the rise of the line-integrated density, the density peaking factor, and the plasma stored energy.

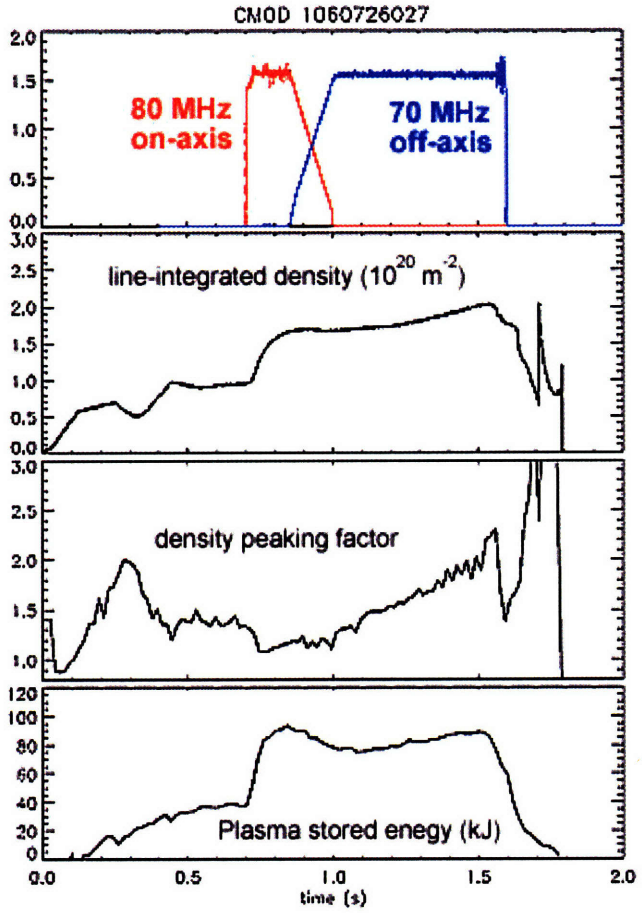

Figure 5-7: Selected plasma parameters for the selected discharge from the dual ICRF frequency setup experiment. Plasma undergoes L-H transition with the application of on-axis ICRF power, which 150 ms later is gradually traded over 150 ms time window for the off-axis RF power of the same magnitude. ITB develops during off-axis heating phase.

Electron temperature measurements were done using the heterodyne ECE system [9] and the results of the measurements are presented in Fig. 5-8. Fig. 5-8(d) shows temperature profiles at times corresponding to 100% on-axis heating, 50%-50% on- and off-axis, and

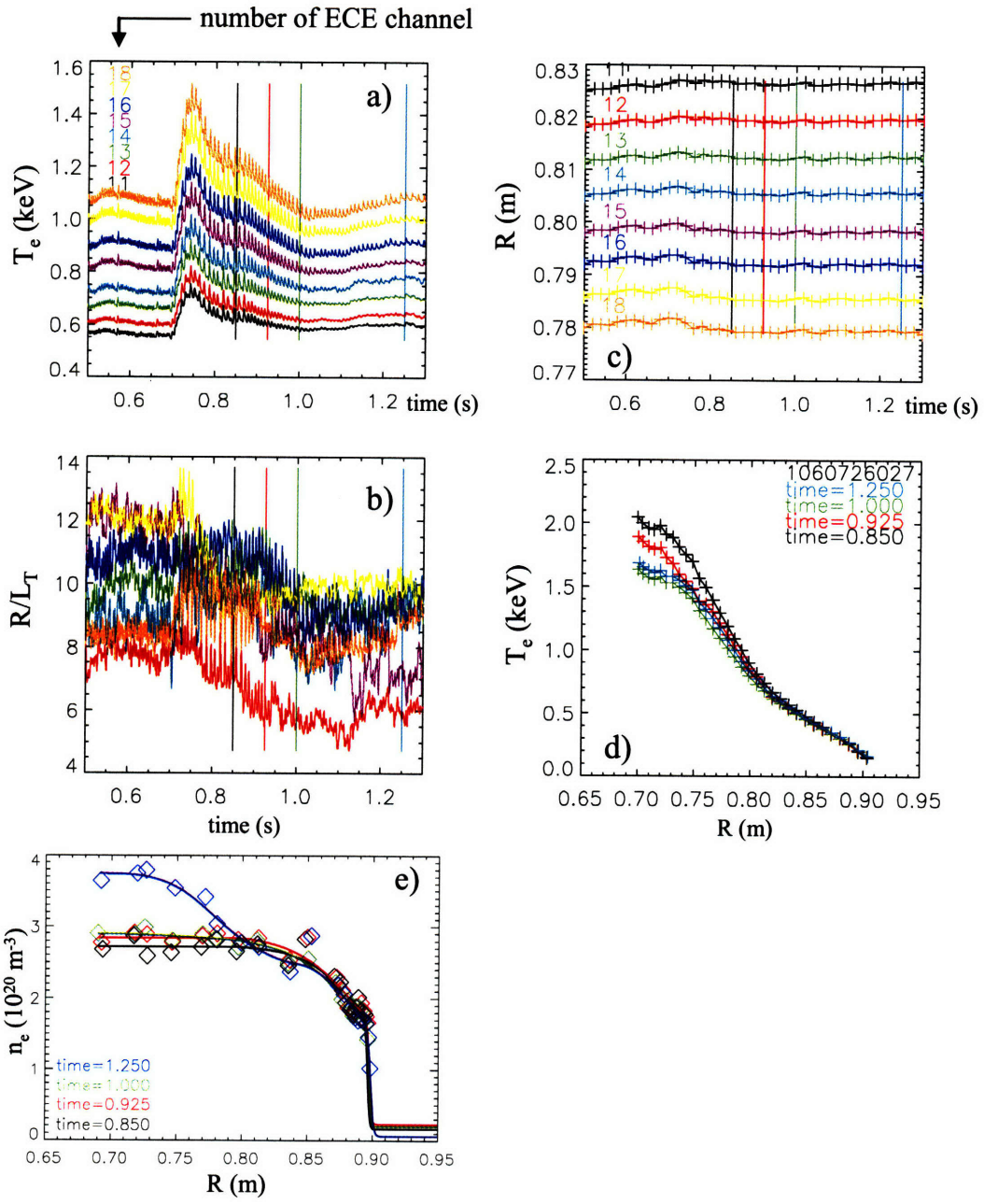

Figure 5-8: Electron temperature gradient measurements for the discharge in Fig. 5-7. (a) Electron temperature time traces of selected ECE channels. The channels are chosen around the ITB foot with their radial position shown in plot (c). Vertical lines on plots (a) – (c) show time slices corresponding to 100% on-axis, 50%-50% on- and off-axis, and 100% off-axis heating phases (last two). (b) R/L_T values for selected radial ECE positions, indicating a decrease in R/L_T for radial positions around ITB foot as heating power is gradually shifted from on- to off-axis. (d) Electron temperature profile at selected times. Central temperature drops with no apparent change on the outer plasma region when the heating power is shifted outward. (e) Electron density profiles at selected times. ITB develops during the off-axis heating phase.

100% off-axis heating (last two time slices). These times are marked by the vertical lines in the other panels. A reduction of the core temperature is observed when the heating scheme is changed from on-axis to off-axis. For a more careful analysis of the temperature gradient, several ECE radial channels are chosen around the ITB foot location. The ITB foot is located near R = 0.8 m and the radial positions of the selected ECE channels are shown in Fig. 5-8(c). Temperature measurements as a function of time of the selected radial channels are shown in Fig. 5-8(a). Fig. 5-8(b) shows R/L_T corresponding to each of the selected ECE channels. From this plot it can be seen that R/L_T gradually decreases in the region of the ITB as the ICRF resonance is moved off axis. Electron density profiles at selected time slices are shown in Fig. 5-8(e). Evolution of the density profile shows that the ITB develops during the off-axis heating phase on a time scale of ~200 ms. It should be pointed out that shifting the ICRF resonance location outward reduces the size of sawteeth as well as the sawtooth inversion radius as can be seen from the Fig. 5-8(a). This might play a role in the ITB formation mechanism also, because it reduces sawtooth induced transport in the center of the plasma, which in turn might balance or even dominate the neoclassical inward pinch in this region.

A few shots were made during this experiment with faster trade-off between on- and off-axis heating. The analysis of the temperature gradient for these discharges shows the same change of R/L_T near the region of the ITB foot, just on a faster time scale consistent with the change of the heating scheme. An ITB develops during the 100% off-axis heating phase.

5.3 Plasma current scan and role of magnetic shear

As was pointed out in section 2.3, so far the triggering of the ITB on C-Mod and the location of the ITB foot have not been linked to any particular rational q surfaces. However, previous experiments demonstrated that this location can be somewhat controlled through variation in the magnetic field. [10] Fiore *et al.* [2] performed more rigorous systematic analysis of the foot location running regressions on plasma current I_p, inverse toroidal field $1/B_t$, and the ratio I_p/B_t. The latter yields the highest correlation with the overall dependence of r/a (foot) = $1.98 * I_p/B_t + 0.06$, which in turn suggests a dependence on the q profile.

A set of experiments described here was part of a broader scan to study this phenomenon. During these experiments the magnetic field was kept constant and plasma current was varied on discharge-to-discharge basis. The ICRF antennas operated at 80 MHz, so the magnetic field of 6.43 T was chosen to move the ICRF nominal resonance location sufficiently off-axis to produce ITBs. Overall, these experiments supported the previously derived trend that the ITB foot location widens with increasing plasma current at a fixed magnetic field. However, it was found that not all of the discharges developed ITBs even though some of them had a long, steady-state EDA H-mode phase.

Some global plasma parameters for two selected discharges are shown in Fig. 5-9. Fig. 5-9(a) depicts a non-ITB discharge as can be judged by the line-integrated density time trace on the top plot. The plasma undergoes L-H transition shortly after the application of ICRF heating and remains in the steady-state EDA H-mode phase until the ICRF power is shut off. Fig. 5-9(b) on the right hand side shows a discharge that developed an ITB. The ITB develops 200-300 ms into the H-mode phase as can be seen

by the increase of the density time trace and then terminates with end of the ICRF heating. The plasma density and stored energy are higher in this case, which is a consequence of the higher ICRF power and plasma current.

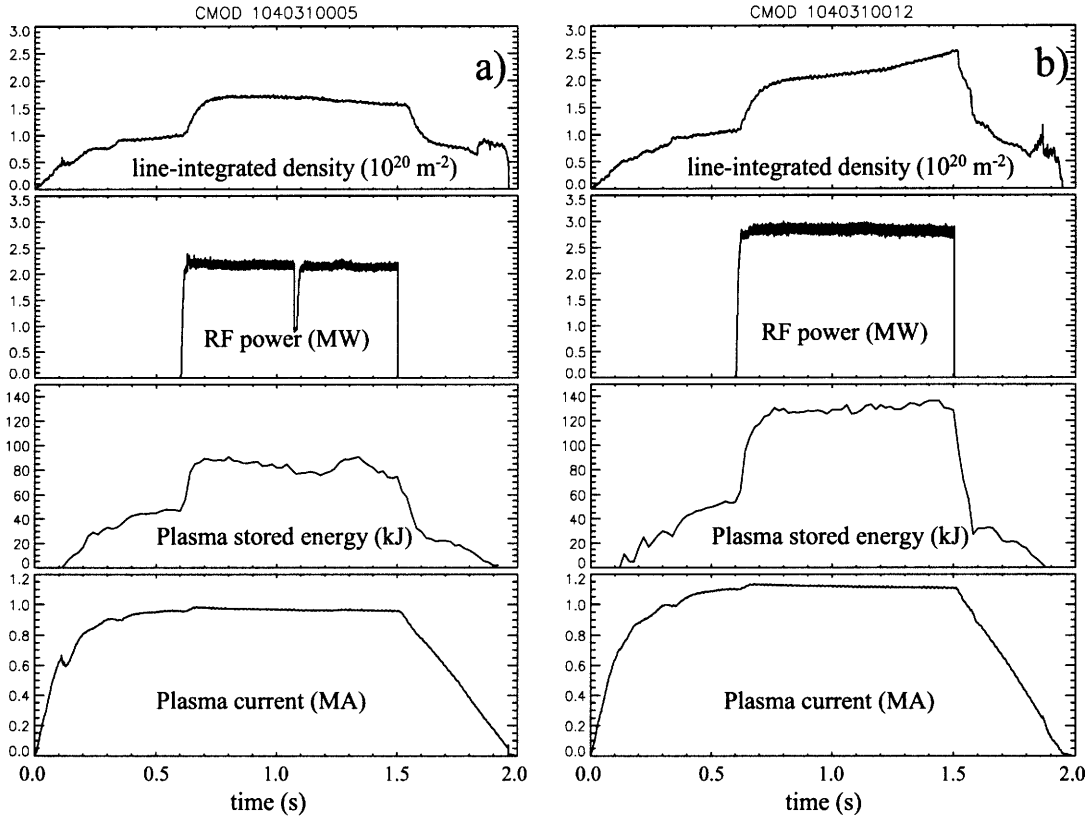

Figure 5-9: Global plasma parameters for selected non-ITB (a) and ITB (b) discharges from the plasma current scan experiment. In both cases the nominal ICRF resonance location was at r/a ~ 0.5.

The analysis of the plasma temperature was done using the 18-channel GPC ECE diagnostic [11]. R/L_T values calculated at the same radial locations in plasma as for the magnetic field scan experiment are shown in Fig. 5-10. Red data points correspond to the discharges that developed ITB while black data points correspond to the ones that did not. The experiment covered a variety of plasma current and ICRF power values. There

is no clear difference between ITB and non-ITB discharges for the electron temperature gradient at any radial location other than possibly plasma core region.

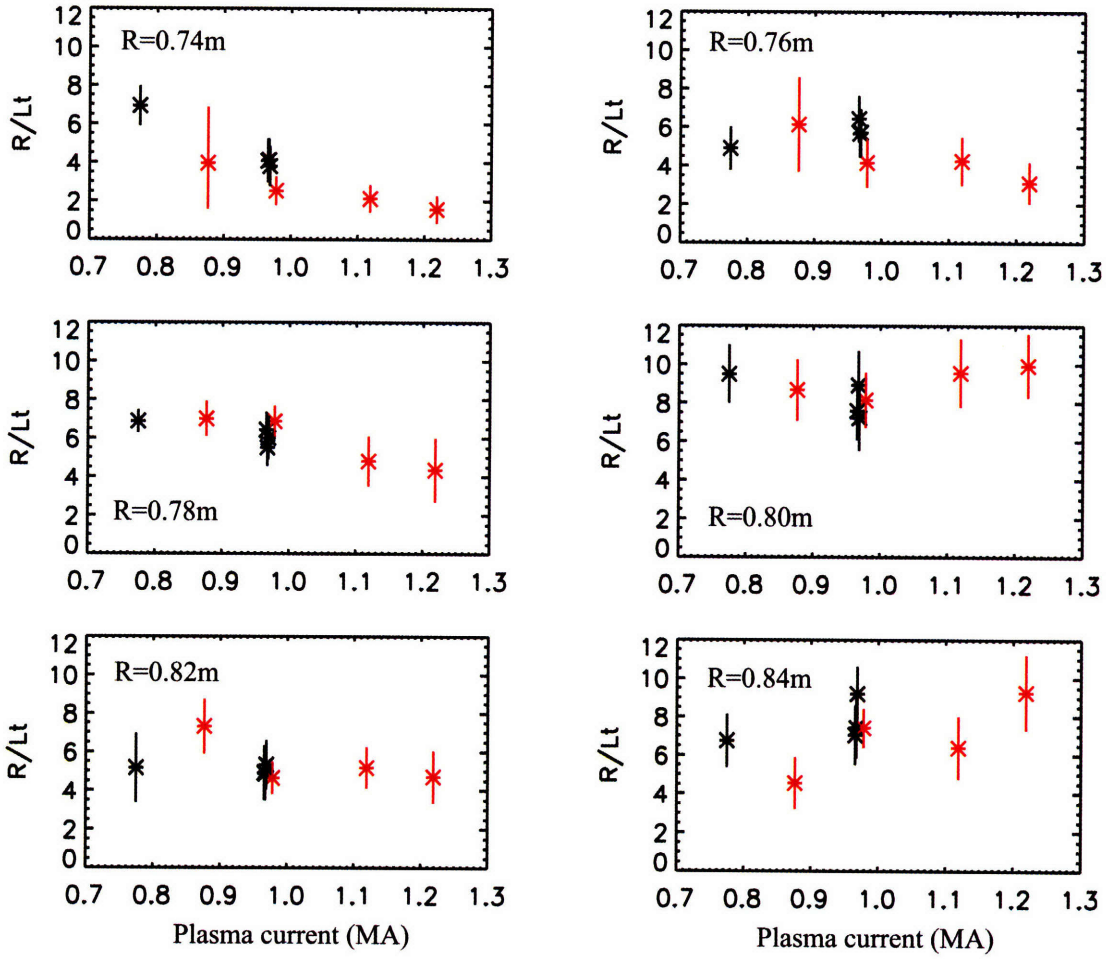

Figure 5-10: R/L_T values for the electron temperature calculated at the same radial location as before for ITB (red) and non-ITB discharges from the plasma current scan experiment. No apparent difference for ITB vs. non-ITB cases is seen for the temperature gradient except possibly in the plasma core.

For all discharges the nominal ICRF resonance location calculated with the toroidal magnetic field was at r/a ~ 0.5. Previous C-Mod results suggest that one should expect ITBs in all cases. The fact that some of the discharges did not develop ITBs suggests that some other mechanism might be at play. This mechanism potentially can be the *q* profile or/and magnetic shear. Reversed or low magnetic shear is well known to

be an important stabilizing factor leading to the ITB formation on other machines. [4, 5] Even though C-Mod has normal shear, the q profile still can play a similar role, not only in defining the ITB foot location but also in the triggering mechanism. Since C-Mod does not have motional Stark effect (MSE) diagnostic for measuring q profile, our analysis has to rely on equilibrium reconstruction provided by EFIT.

EFIT [12] is a magnetic equilibrium reconstruction code which performs a numerical solution of the Grad-Shafranov equation [13, Ch. 6.2],

$$\Delta^* \psi = -\mu_0 R^2 \frac{dp}{d\psi} - F\frac{dF}{d\psi} \tag{5.1}$$

$$\text{where } \mathbf{B} = \frac{1}{R}\nabla\psi \times \mathbf{e}_\phi + \frac{F}{R}\mathbf{e}_\phi \tag{5.2}$$

$$\text{and } \mu_0 \mathbf{J} = \frac{1}{R}\frac{dF}{d\psi}\nabla\psi \times \mathbf{e}_\phi - \frac{1}{R}\Delta^*\psi\,\mathbf{e}_\phi . \tag{5.3}$$

$p(\psi)$ and $F(\psi)$ are two free functions, which together with the boundary conditions determine the plasma equilibrium. A standard magnetic EFIT is run on C-Mod automatically after every shot. It performs a non-linear least-squares fit to a set of coefficients defining p' and FF', subject to constraint equations based on magnetic measurements supplemented by additional constraints which serve to restrict the solutions in a physically reasonable way.

The magnetic shear defined as $s = (r/q)dq/dr$ is calculated based on the EFIT equilibrium. The 4 best shots (2 ITB, 2 non-ITB) were selected from the plasma current scan experiment, two of which are presented in Fig. 5-9. The results of the magnetic shear calculation for these shots are depicted in Fig. 5-11. The averaging has been done over the steady portion of the discharges (pre-ITB phase for ITB discharges). This figure

demonstrates that there is now a difference in the magnetic shear for ITB vs. non-ITB discharges as calculated by the standard EFIT.

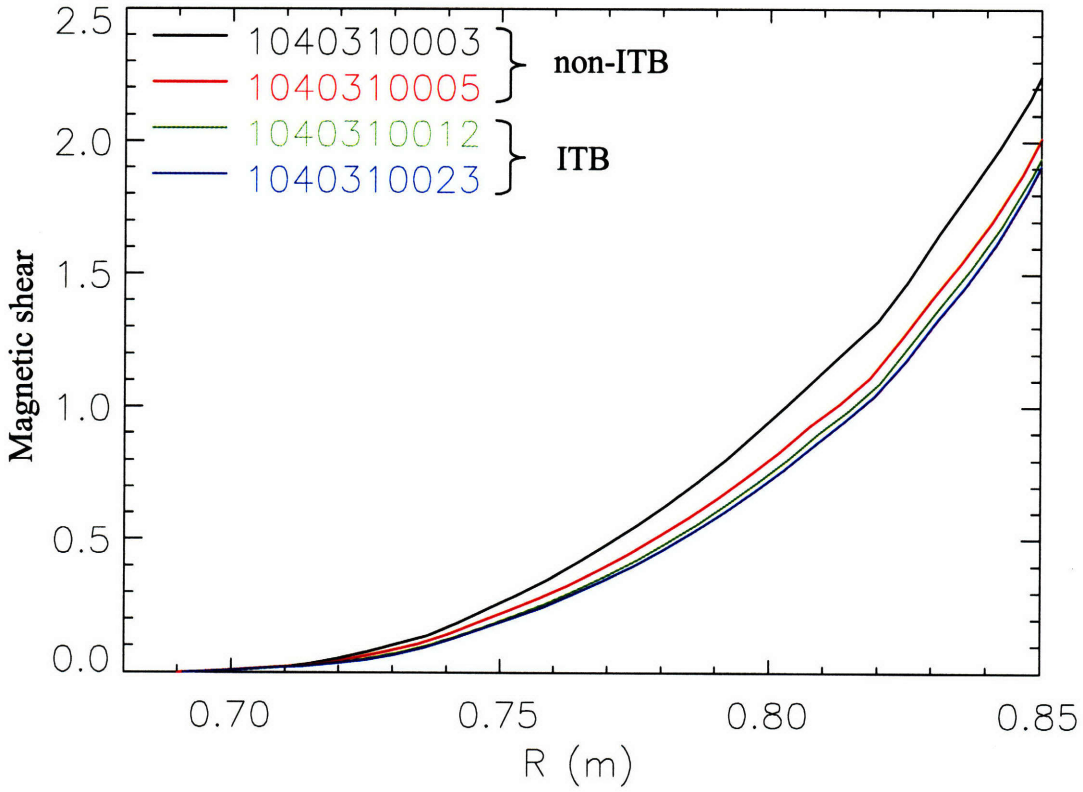

Figure 5-11: Magnetic shear for the selected discharges from the plasma current scan experiment. Time averaging has been done over the steady portions of the H-modes (pre-ITB phase for ITB discharges). Shots 03 and 05 did not develop ITBs, while shots 12 and 23 did.

The automatically generated equilibrium calculations are based strictly on the magnetic data, and the solution parameters are designed to provide a reasonably good solution for flux-surface geometry, stored energy, and other quantities for a wide range of plasma conditions. This comes at a price, because in order to achieve this robustness the functional form of p' and FF' profiles is severely restricted. By default a third order polynomial for FF' and a second order polynomial for p' are assumed. While the integral properties such as stored energy and even some local quantities like peak

pressure are expected to be pretty accurate, one cannot expect the same degree of accuracy for the entire q profile, especially towards the center of the plasma where the influence of the measured boundary conditions is less significant. Therefore, it should not be a surprise that the magnetic shear of the above mentioned discharges is similar even when an ITB develops.

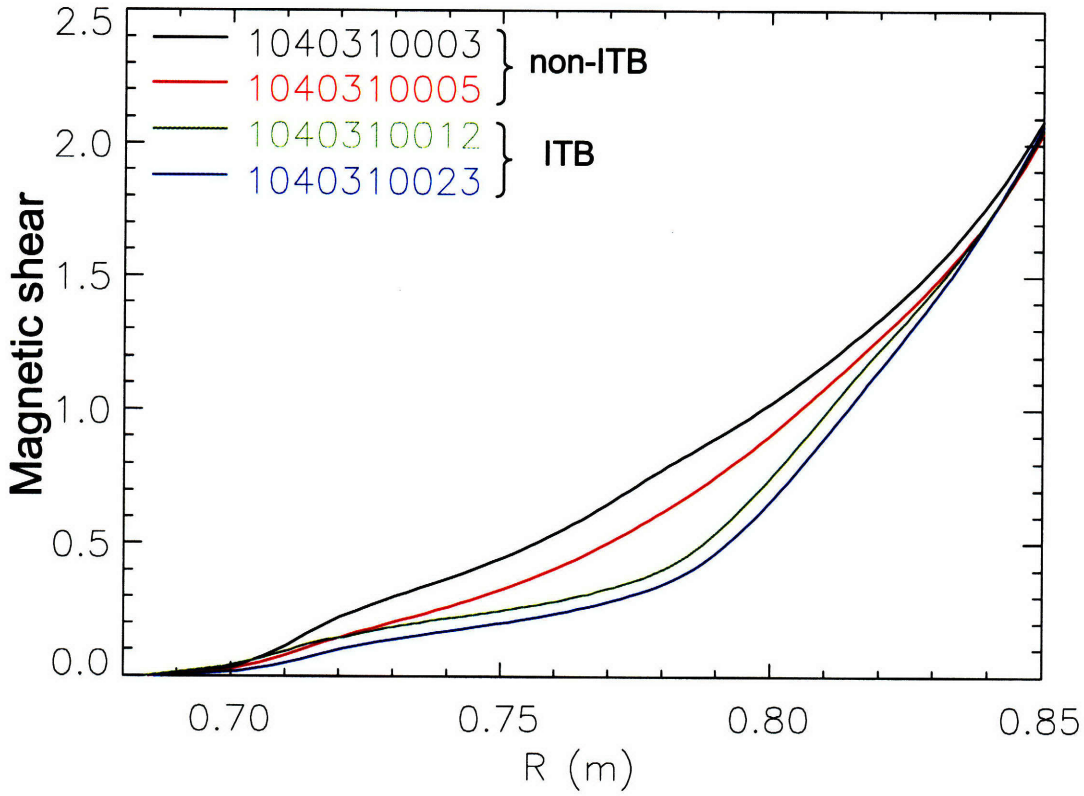

Figure 5-12: Magnetic shear for the selected discharges from the plasma current scan experiment as calculated based on the kinetic EFIT. Averaging has been done over the steady portions of the H-modes (pre-ITB phase for ITB discharges). Shots 03 and 05 did not develop ITBs, while shots 12 and 23 did. Magnetic shear is lower in the core plasma region for the discharges that developed ITBs.

To improve on this situation one can incorporate kinetic measurements of the pressure profile into the EFIT calculations. Pressure profiles are measured by Thomson scattering and are used to constrain p', which in this case can have more degrees of freedom permitted in the parameterization. The results of the magnetic shear calculations

based on the kinetic EFIT runs are presented in the Fig. 5-12. The averaging of the magnetic shear values was done over the same time windows as for the Fig. 5-11. It is clearly seen that the magnetic shear is lower for the discharges which ultimately developed ITBs. Temporal analysis reveals that this trend is observed in the core plasma region throughout most of the discharge duration. Moreover, this low magnetic shear region extends radially to approximately a position where ITB foot is located later in the discharge. This fact suggests that low magnetic shear might play an important role in triggering ITBs in C-Mod plasmas.

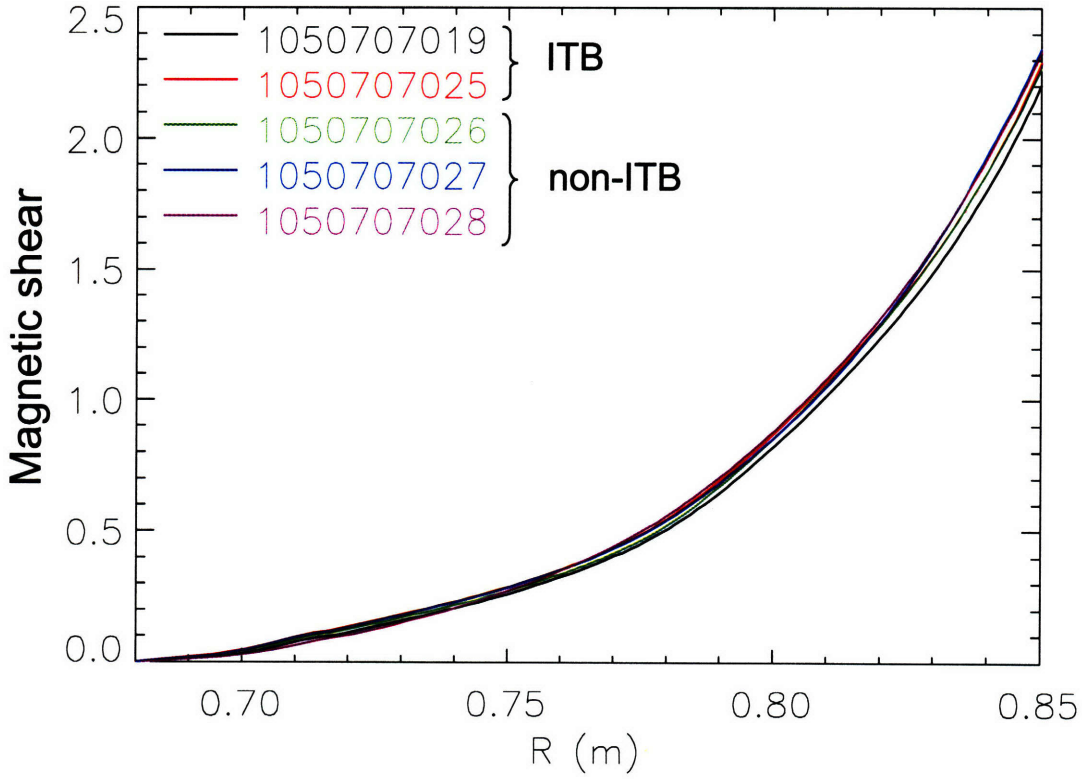

Figure 5-13: Magnetic shear for the selected discharges from the magnetic field scan experiment as calculated based on the kinetic EFIT. Averaging has been done over the steady portions of the H-modes (pre-ITB phase for ITB discharges). Magnetic shear is similar for all the analyzed discharges.

Similar analysis has been performed for the discharges from the magnetic field scan experiment. The magnetic shear determined from the kinetic EFIT equilibrium reconstruction is plotted in Fig. 5-13. As in the previous case the averaging has been done over the steady portions of the H-mode phase corresponding to pre-ITB values for the ITB discharges. From this figure it can be seen that the magnetic shear is indeed very similar for all the analyzed discharges. This is the result of the similarity of the q_{95} values as well as plasma density and temperature profiles, as expected from the experimental design.

Several sets of experiments were performed on Alcator C-Mod to experimentally verify certain hypotheses about the ITB formation in ICRF-heated plasmas on C-Mod. To summarize, these studies revealed 2 possible mechanisms of instability suppression: a) decrease of the temperature gradient achieved through the off-axis heating and b) lower magnetic shear. These stabilizing mechanisms can suppress the turbulence induced outward diffusion, leading to a density peaking which results from the neoclassical inward pinch. Further exploration of these phenomena requires stability analysis and will be presented in the next two chapters with the results of the plasma modeling.

References for Chapter 5

[1] R. E. Rice *et al.*, Nucl. Fusion **42**, 510 (2002).
[2] C. L. Fiore *et al.*, Phys. of Plasmas **11**, 2480 (2004).
[3] S. J. Wukitch *et al.*, Phys. of Plasmas **9**, 2149 (2002).
[4] R. C. Wolf, Plasma Phys. Control. Fusion **45**, R1 (2003).
[5] J. W. Connor *et al.*, Nucl. Fusion **44**, R1 (2004).
[6] P. J. O'Shea, A. E. Hubbard, and Alcator C-Mod group, *Proc. 9th Joint Workshop on ECE and ECH, Borrego Springs,* CA, January 23-26, 1995 (World Scientific, Singapore, 1995), pp. 393-401.
[7] J. E. Rice and E. S. Marmar, Rev Sci. Instrum. **66**, 752 (1995).
[8] C. L. Fiore and R. L. Boivin, Rev Sci. Instrum. **66**, 045 (1995).
[9] L. W. Heard *et al.*, Rev. Sci. Instrum. **70**, 1011 (1999).
[10] J. E. Rice *et al.*, Nucl. Fusion **43**, 781 (2003).
[11] G. Taylor *et al.*, *Bull. Am. Phys. Soc.*, **43**, 1821 (1998).
[12] L. Lao, H. John, R. Stambaugh, A. Kellman, and W. Pfeiffer, Nucl. Fusion **25**, 1611 (1985).
[13] J. P. Freidberg, *Ideal Magnetohydrodynamics* (Plenum Press, 1987).

Chapter 6

6 TRANSP simulations

TRANSP [1] is a large system of codes which is essentially an extensive collection of theoretical and experimental physics as well as empirical data processing knowledge. It is one of the best tools available for analyzing data from various tokamaks. These calculations are necessary to generate inputs for the gyrokinetic stability code used in the next chapter. They are also useful in understanding the nature of the ITBs. For the C-Mod tokamak, TRANSP is usually run remotely on a computer cluster at Princeton Plasma Physics Laboratory and the results are then stored in the MDS+ tree in the C-Mod computer system. Details on how to prepare TRANSP runs and do post-run analysis can be found in Refs. [2, 3].

6.1 Input profiles

TRANSP, like many other transport analysis codes requires smooth profiles of plasma density and temperature as input since their gradients affect plasma transport and equilibrium properties. For this purpose software packages were developed for fitting plasma electron density and temperature.*

Smooth density profiles are obtained by fitting the combined core and edge Thomson scattering data. Typically in C-Mod plasmas, edge and core regions have very

* The original fitting packages also known as fit_ne and fit_te were developed in cooperation with Darin Ernst. The graphical user interface named fiTS was primarily developed by MIT undergraduate students Eric Grebing and David Ely under the guidance of D. Ernst and myself.

different density scale lengths. It is especially true during the H-mode phase of the discharge where a narrow (~ 3-4 mm) H-mode barrier and relatively flat core density profile coexist. Moreover, edge TS radial resolution is ~ 1-2 mm while the core TS system has spatial resolution on the order of 1-2 cm. For these reasons, the core and edge plasma regions are fitted separately using different fitting algorithms. The edge region, where edge TS data with a few core data points are used, is typically fitted with a *tanh* function. This particular functional form was adapted from Ref. [4], where it was used for the H-mode pedestal studies on C-Mod. It as was found empirically to work well for the L-mode phase too. The core plasma region, with a few data points from the edge measurements, is fitted with a B-spline [5], which takes into account experimental uncertainties in the TS data. The initial overlap of the fitting regions ensures good overlap of the resultant fits. Finally the individual fits for the plasma core and edge are continuously stitched together over a certain region to yield a final smooth density profile which is used as an input for the TRANSP code. An example of such a fit for the H-mode phase is shown in Fig. 6-1(a). Density measurements form the core and edge TS diagnostics are shown in squares and diamonds respectively. Typical error bars on these measurements are 10-15%. The red line shows the smooth fitted density profile produced by the density fitting package. In order to derive profiles of the plasma effective charge, these measurements can be used in conjunction with the $n_e\sqrt{Z_{eff}}$ profiles from VB measurements corrected for T_e shown by the blue curve. The resultant radial profile of Z_{eff} is shown in Fig. 6-1(b). In order to minimize the diagnostics' artifacts, some additional processing such as truncation and radial smoothing is done for the TRANSP analysis. An example of the density and Z_{eff} profiles during the fully developed ITB

phase in C-Mod plasmas is shown in Fig. 6-2, where symbols and color coding are the same as in Fig. 6-1. Also shown in the plot are the positions of the ITB foot and inflection point as determined from the VB measurements, which can serve as a proxy for the electron density when Z_{eff} is flat across the profile. Impurity accumulation in the plasma core, which is a typical effect for the ITB plasmas, is clearly seen as the rise of the Z_{eff} inside the ITB foot.

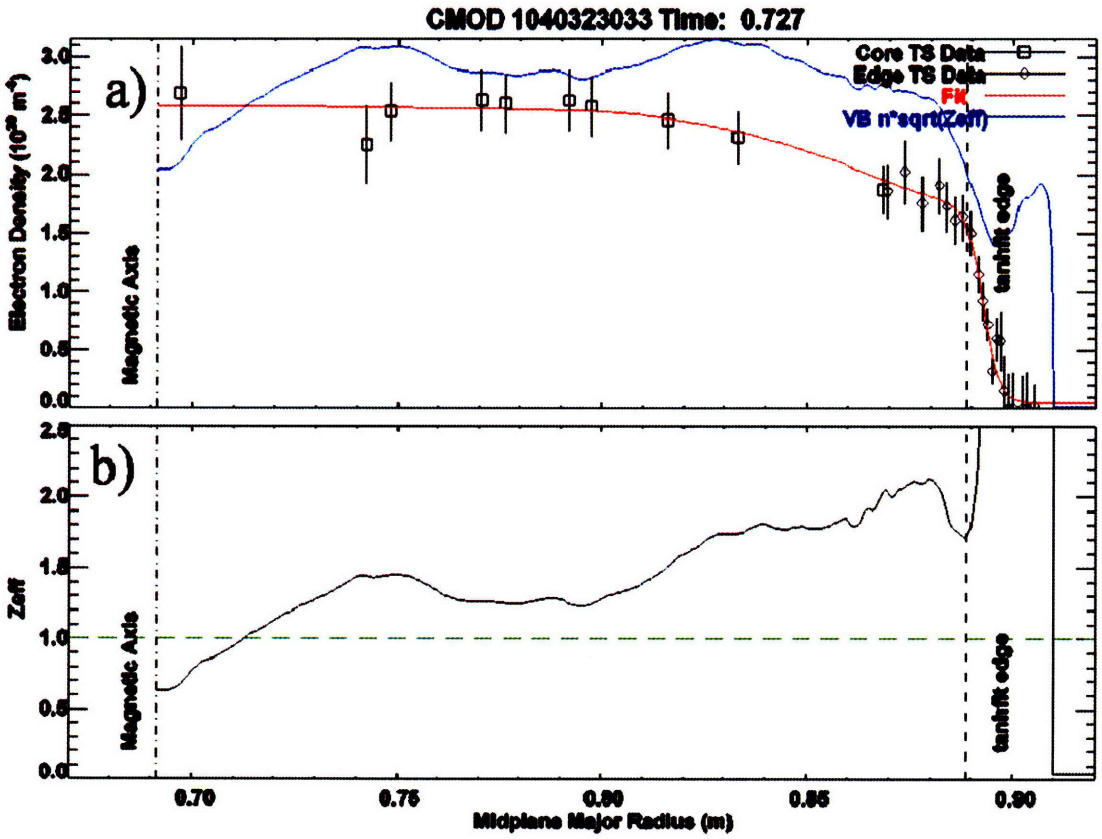

Figure 6-1: Typical plasma density (a) and Z_{eff} (b) profiles during the H-mode phase. (a) Squares correspond to core TS density measurements while diamonds depict edge TS data points. The red line is the smooth density profile as produced by the density fitting routine. The blue curve corresponds to the $n_e\sqrt{Z_{eff}}$ profile as measured by the VB diagnostic. (b) Profile of the effective plasma charge as determined from the TS density and VB measurements.

Smooth temperature profiles are obtained by fitting all available T_e data including core and edge TS diagnostics as well as various ECE diagnostics: GPC, GPC2, and FRCECE. In this case all ECE data are interpolated onto the TS time grid and can be remapped onto the low field side to construct a profile. Also for each ECE data point at each time slice, the ratio of the local plasma density to the critical value, at which the ECE signal is cutoff, is calculated. This ratio is used as a validity check to find and disregard all ECE data that is nearing cutoff.

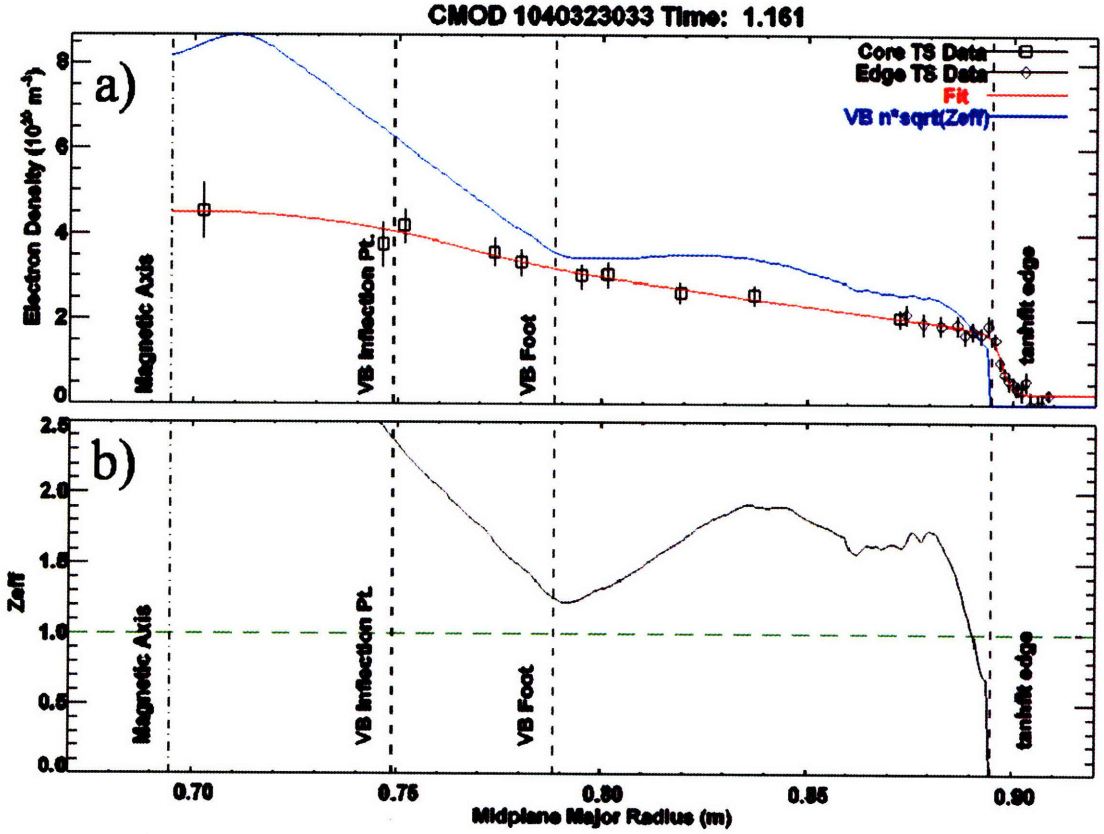

Figure 6-2: Typical plasma density (a) and Z_{eff} (b) profiles during the fully developed ITB phase. Symbols and color coding are the same as in Fig 5-1. The ITB foot and inflection point are determined from the VB measurements which can serve as a proxy for the density profile. Impurity accumulation inside the ITB is seen in the Z_{eff} profile.

This is done because the density near the critical value can attenuate the ECE signal and result in false temperature readings. The temperature fitting is done in a way similar to the density fitting procedure. Both edge and core regions are fitted separately and then combined by a cubic spline. The fitting procedures are run automatically, but have a variety of keyword and parameters a user can change to get satisfactory fitting results. An example of the temperature profile obtained this way is shown in Fig. 6-3.

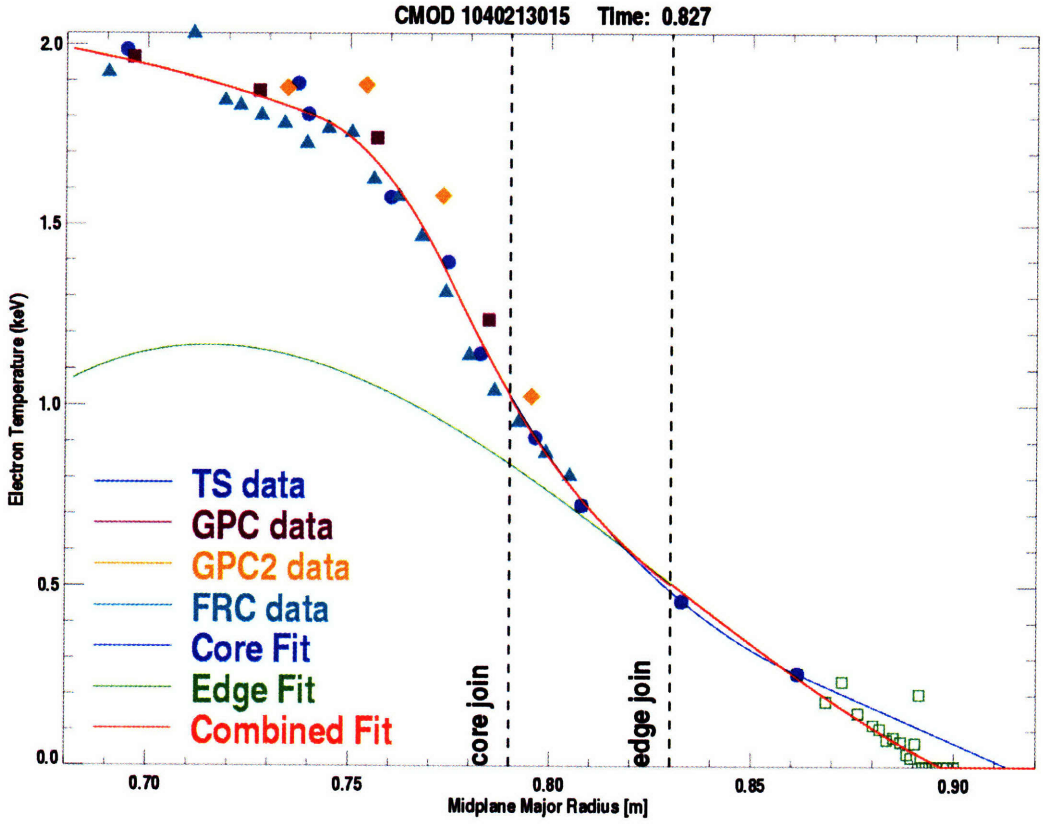

Figure 6-3: Electron temperature measurements and fits. Individual fits to the core and edge data are combined over the region defined by 'core join' and 'edge join' parameters as shown.

A more detailed description of the fitting algorithm can be found in the Appendix A. The fiTS user's manual (UsersManual.pdf), the main documentation

(FrontendDoc.pdf) as well as the routines' description (AuxFuncs.pdf) are stored on the C-Mod Linux cluster and can be found at /usr/local/cmod/idl/fits/documentation/.

6.2 TRANSP equilibrium reconstruction

Since direct measurements of the magnetic field pitch angle and therefore, the current density and electric field are not available on C-Mod, one has to rely on either EFIT or TRANSP equilibrium reconstruction. TRANSP performs its own calculations of the magnetic geometry. For that, it uses a fixed boundary equilibrium solver VMEC [6]. TRANSP solves the poloidal magnetic field diffusion equation, which is derived from Maxwell's equations and has the form

$$\frac{\partial}{\partial t}\frac{\partial \psi}{\partial \rho} = \frac{\partial}{\partial \rho}\left(\frac{2\pi\langle \mathbf{E}\cdot\mathbf{B}\rangle}{RB_t\langle R^{-2}\rangle}\right) \tag{6.1}$$

where ψ is the poloidal flux, R is the local major radius, and ρ is the radial flux surface coordinate, and $\langle\ \rangle$ denotes the flux surface average. The parallel electric field and parallel current density are related by [3]

$$\langle \mathbf{E}\cdot\mathbf{B}\rangle = \eta_{\parallel}\langle(\mathbf{J}-\mathbf{J}_{DR})\cdot\mathbf{B}\rangle \tag{6.2}$$

where $\eta_{\parallel}$ is the parallel resistivity and $\mathbf{J}_{DR}$ is the total current density not driven by the electric field. The boundary condition for the solution is the measured total plasma current as a function of time

$$I_p = 2\pi\int_0^a J_{\parallel}(r)rdr \tag{6.3}$$

Different models for the resistivity are allowed in TRANSP, but a neoclassical model was used for all TRANSP runs for this thesis research. Neoclassical resistivity is a complex function of n_e, T_e, and Z_{eff}. The latter profiles are obtained using fitting routines as described in the previous section. The profiles of Z_{eff} are assumed to be flat during the L- and H-modes with the values averaged over the core plasma region, and a single impurity specie is assumed. Boron or oxygen is typically used as the impurity in these TRANSP runs, which corresponds to the average Z_{eff} of the C-Mod plasmas. Peaked Z_{eff} profiles are used for the analysis of the fully developed ITB phase. This approach is consistent with both previous results of impurity measurements [7, 8] and empirical evidence found from TS data analysis (e.g., see Fig. 6-1(a)). The computed loop voltage, which is given by

$$V_{loop} = \left(\frac{2\pi \langle \mathbf{E} \cdot \mathbf{B} \rangle}{R B_t \langle R^{-2} \rangle} \right)_{r=a} \tag{6.4}$$

serves as a check on the accuracy of these calculations. Usually equations (6.3) and (6.4) cannot be satisfied simultaneously. However, the computed loop voltage is usually in a good agreement with the measurements. A typical example of such calculations is presented in Fig. 6-4.

The result of the analysis of the resultant q profile is shown in Fig. 6-5 where the magnetic shear for the selected discharges from the current scan experiment is plotted. From this picture, it is clearly seen that the magnetic shear is lower for the discharges that developed ITB than it is for the ones that did not. This trend is valid for the core plasma region, and is in agreement with the results of the kinetic EFIT calculations. Overall, this

suggests that magnetic shear can play an important role in the formation of ICRF-heated ITBs on C-Mod.

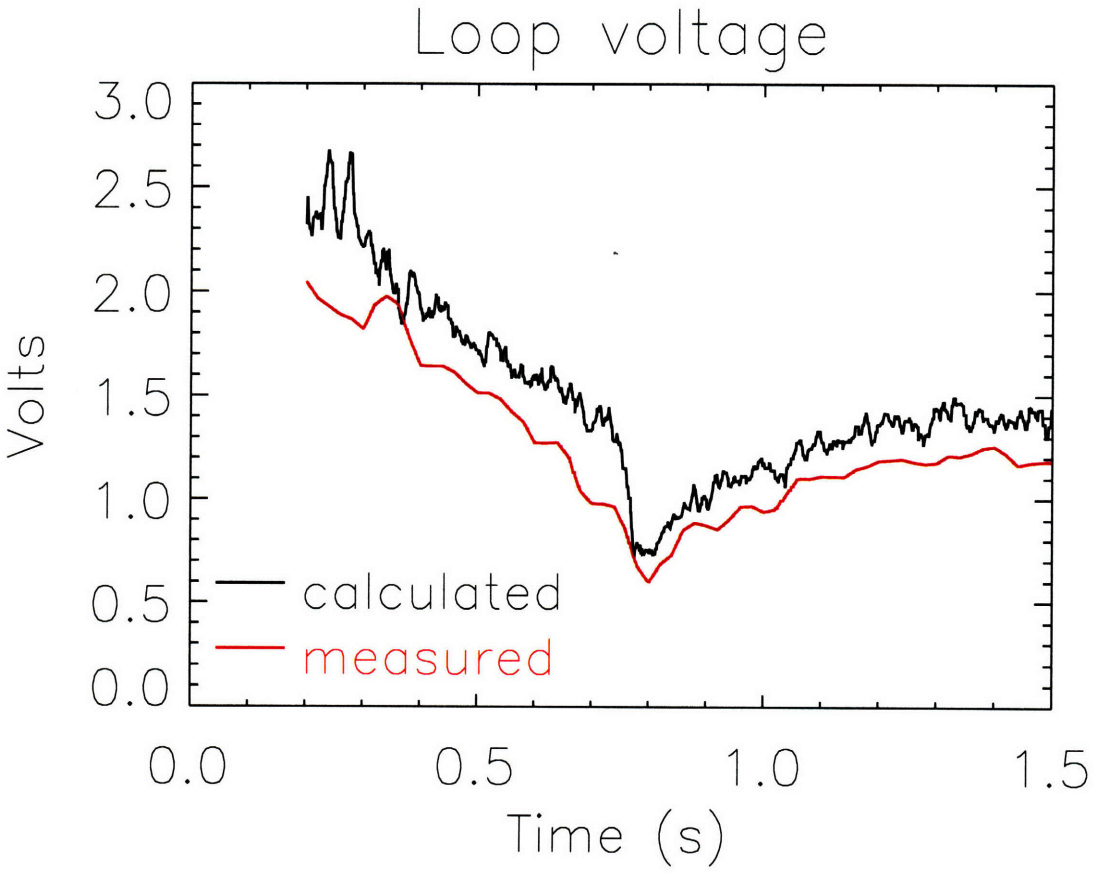

Figure 6-4: Calculated by TRANSP (black) and experimentally measured loop voltage as function of time for one of the H-mode discharges.

Since these discharges are sawtoothing and q_0 drops below 1, TRANSP runs were set up to use the Kadomtsev sawtooth model [9], which resets q_0 to 1 at each sawtooth crash. Additional switches to keep $q_0 > 1$ are available in the TRANSP namelist. The analysis shows however, that regardless of whether these switches are used in the TRANSP runs, the resultant magnetic shear exhibits the same trend depicted in Figs. 5-12 and 6-5.

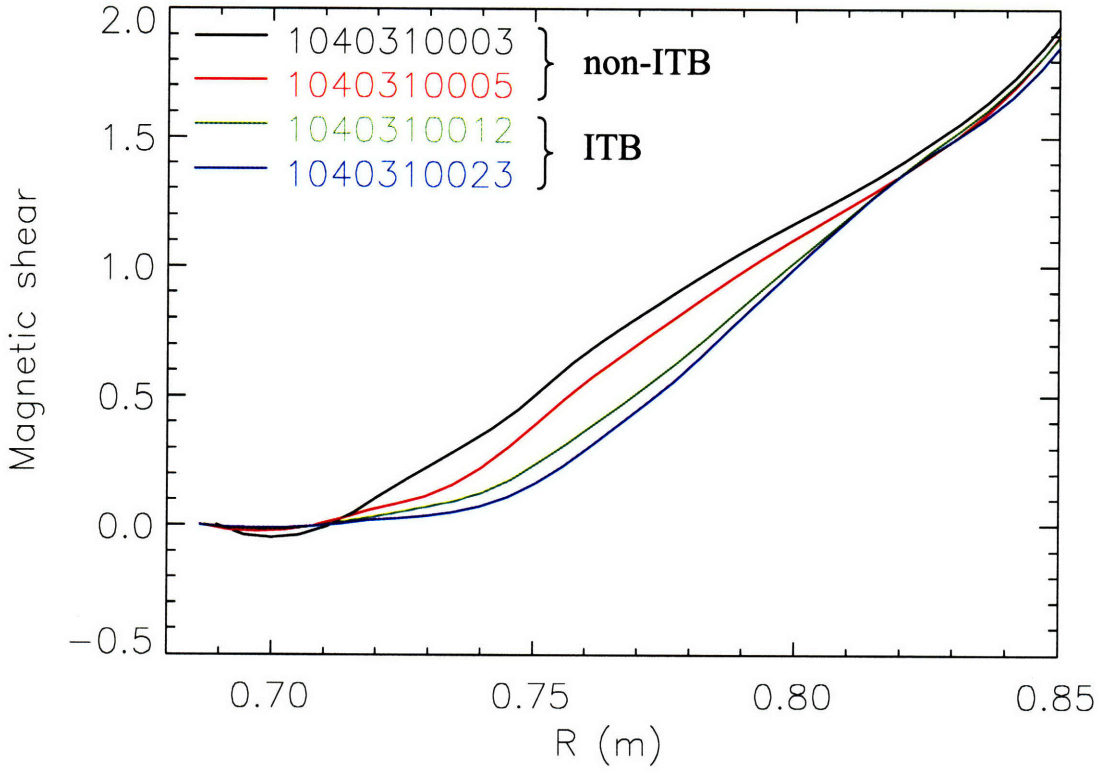

Figure 6-5: Magnetic shear for the selected discharges from the plasma current scan experiment as calculated by TRANSP. Averaging has been done over the steady portions of the H-modes (pre-ITB phase for ITB discharges). Magnetic shear for the ITB discharges is lower in the core plasma region, which is in agreement with the kinetic EFIT calculations.

6.3 ICRF power deposition

In addition to ohmic heating, Alcator C-Mod uses ICRF heating as a source of auxiliary heating. There are no direct measurements of the power deposition profiles, however. One has to rely again on the TRANSP calculations. In TRANSP the ICRF power deposition from the D(H) minority ion cyclotron heating is calculated using a bounced averaged Fokker-Planck code coupled to the full wave code TORIC. [10] The ICRF power deposition depends on the fraction of the minority ions. On C-Mod it is obtained through spectroscopic measurements of D_α and H_α radiation and is typically 4-

5%. TRANSP calculations for the discharges from the magnetic field scan experiment show that the ion minority tail temperature does not exceed 5 keV. This result is in good agreement with the experimental measurements [11] from Alcator C for similar plasma parameters. At this rather low temperature, the hydrogen minority ions from the tail of the distribution created by ICRF tend to equilibrate with both the deuterium ions and the electrons. Fig. 6-6 shows the radial density profiles of the ICRF power as well as the total power distribution between ions and electrons for some of the analyzed non-ITB (Fig. 6-6a) and ITB (Fig. 6-6b) discharges.

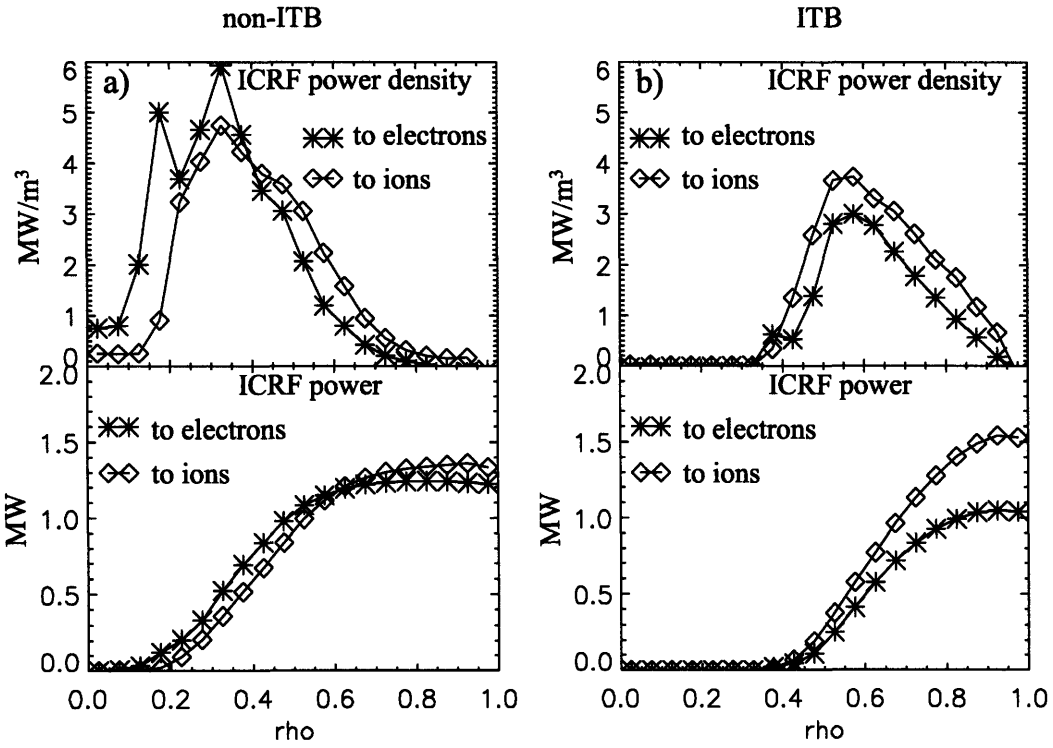

Figure 6-6: ICRF radial power density profiles (upper plots) and radial total power distribution (lower plots) as calculated by TRANSP for a) non-ITB and b) ITB discharges during the pre-ITB H-mode phase. There is approximately the same amount of ICRF power going to ions (diamonds) and electrons (asterisks) in the non-ITB discharge. There is ~50% more ICRF power going to ions than to electrons in the ITB discharge.

Profiles are plotted against square root of normalized toroidal flux $\rho = \sqrt{\overline{\psi}}$. The upper plots in Fig. 6-6 show density profiles of ICRF power going to deuterium ions

(diamonds) and electrons (asterisks), while the bottom plots depict the total integrated ICRF power distribution between ions (diamonds) and electrons (asterisks). From this picture it can be seen that approximately the same amount of ICRF minority heating power goes to ions and electrons in the discharges that do not develop ITBs. However, there is approximately 50% more power going to deuterium ions than to electrons in the discharges that develop ITBs. Also it can be clearly seen that the ICRF heating location is indeed shifted outward for the ITB discharge which corresponds to the higher magnetic field. All these facts can be important for the temperature considerations, since both temperature gradients and values affect stability of ITG modes.

6.4 *Ion temperature and transport analysis*

TRANSP solves particle and power balance equations in order to find particle flux Γ and heat flux **q** as well as the corresponding particle diffusion D and heat diffusion χ coefficients. In a simple form these equations can written as follows

$$\nabla \cdot \Gamma_j = S_j - \frac{\partial n_j}{\partial t} \tag{6.5}$$

$$\nabla \cdot q_j = Q_j + \frac{3}{2} n_j \frac{\partial T_j}{\partial t} \tag{6.6}$$

where j refers to the plasma species, S is the particle source, and Q is the thermal source. In C-Mod discharges, the core particle source is zero, and therefore, the pinch term must play an important role in density peaking. Particle flux is assumed to consist of diffusive part plus an inward neoclassical pinch

$$\Gamma_e = -D_e \nabla n_e + \Gamma_e^{neo} \tag{6.7}$$

The neoclassical component of the total particle flux is computed based on the Hinton-Hazeltine formulation [12] and includes the Ware pinch [13] as well as contributions from the temperature and density gradient driven terms. A comparison of the neoclassical Ware pinch and total electron velocities during the pre-ITB phase is shown in Fig. 6-7. The analysis suggests that the neoclassical pinch is strong enough on C-Mod to explain the experimentally observed density rise, which is consistent with the previous TRANSP analysis [14] and non-linear gyrokinetic calculations by Ernst *et al.* [15], as well as the results presented in the next chapter.

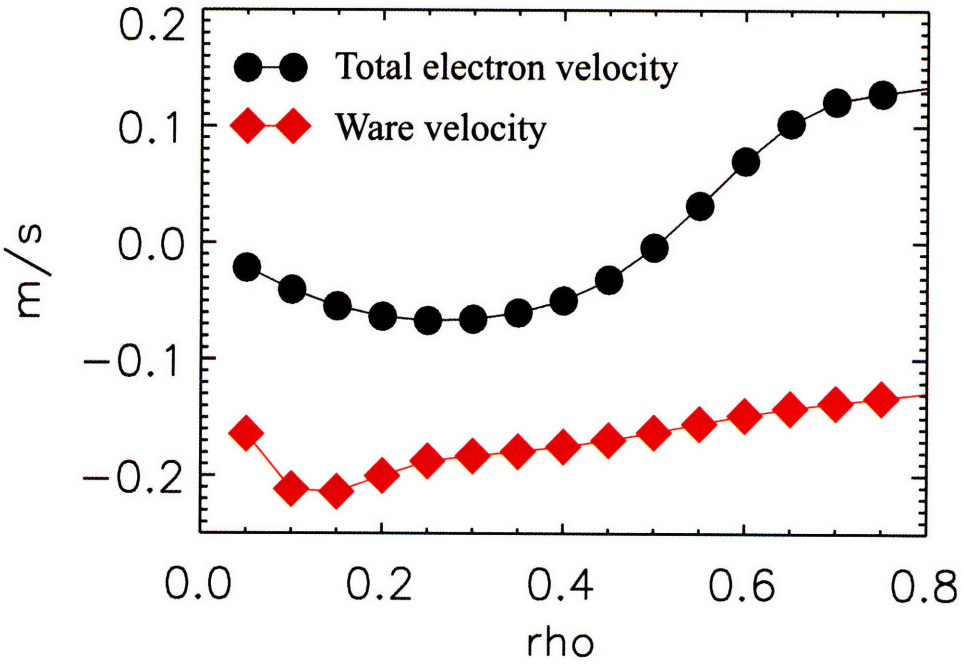

Figure 6-7: Radial profiles of the total electron and Ware velocities during the pre-ITB H-mode phase of the discharge.

For the heat flux calculations, TRANSP assumes the flux to be entirely diffusive, so that it can be written as $q = n\chi\nabla T$. The power balance analysis requires knowing temperature profiles for both electrons and ions as well as heat sources. In addition to

ohmic heating, heat sources include direct electron and ion ICRF heating, mode conversion, and slowing down of the minority tail as well as heat exchange between the ions and electrons. All of these are calculated by the built-in RF code TORIC and TRANSP self-consistently. While the electron temperature on C-Mod is measured with several diagnostics, measurements of the ion temperature profiles are quite limited for most experiments. However, ion temperature profiles can be modeled in TRANSP by solving the conducted heat flux for T_i given a model for χ_i. Such analysis was performed for the 80 MHz magnetic field scan. In these modeled discharges the plasma ion temperature profile was calculated under the assumption that χ_i is proportional to the neoclassical ion thermal diffusivity [16], $\chi_i = \kappa\chi^{\text{Chang-Hinton}}$, which is a standard procedure in this type of analysis [3, Ch. 3.6].

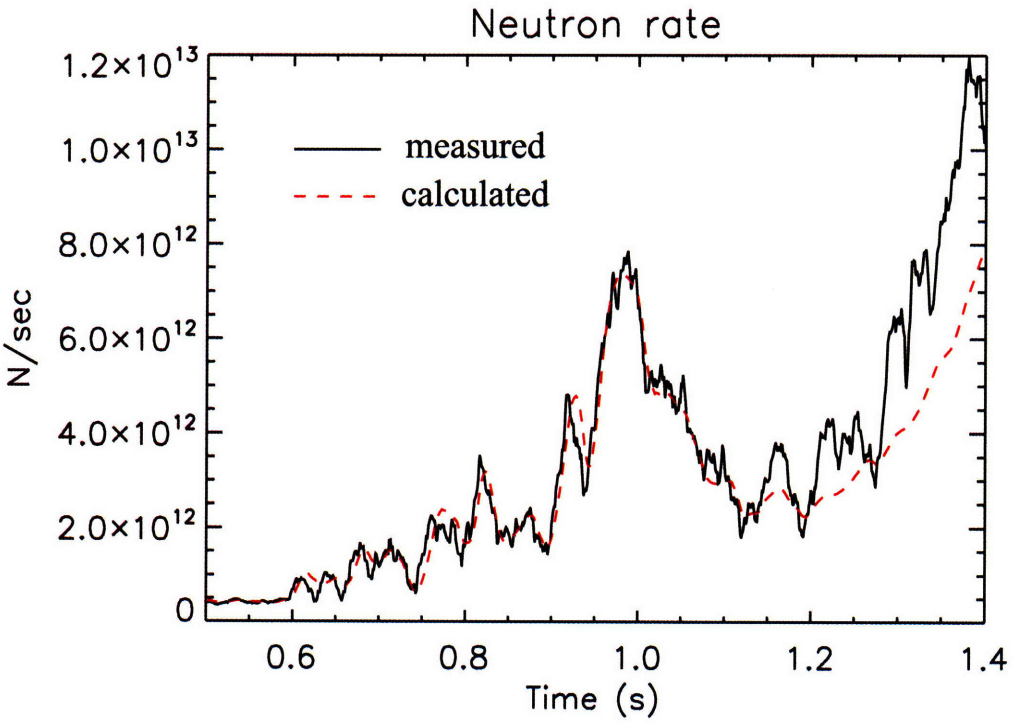

Figure 6-8: Measured and calculated by TRANSP neutron rates. Good agreement is obtained throughout most of the discharge until the ITB starts to develop at t=1.2 s.

The factor of proportionality κ is chosen in a feedback corrected loop such that the calculated neutron rate matches the one measured in the experiment. A comparison of the experimentally measured and calculated neutron rates is shown in Fig. 6-8. Good agreement is obtained throughout the discharge in this case up until the ITB starts to develop at around t = 1.2 s.

The results of the ion temperature simulation are shown in Fig. 6-9. All of the calculated profiles are shown during the H-mode (pre-ITB) phase.

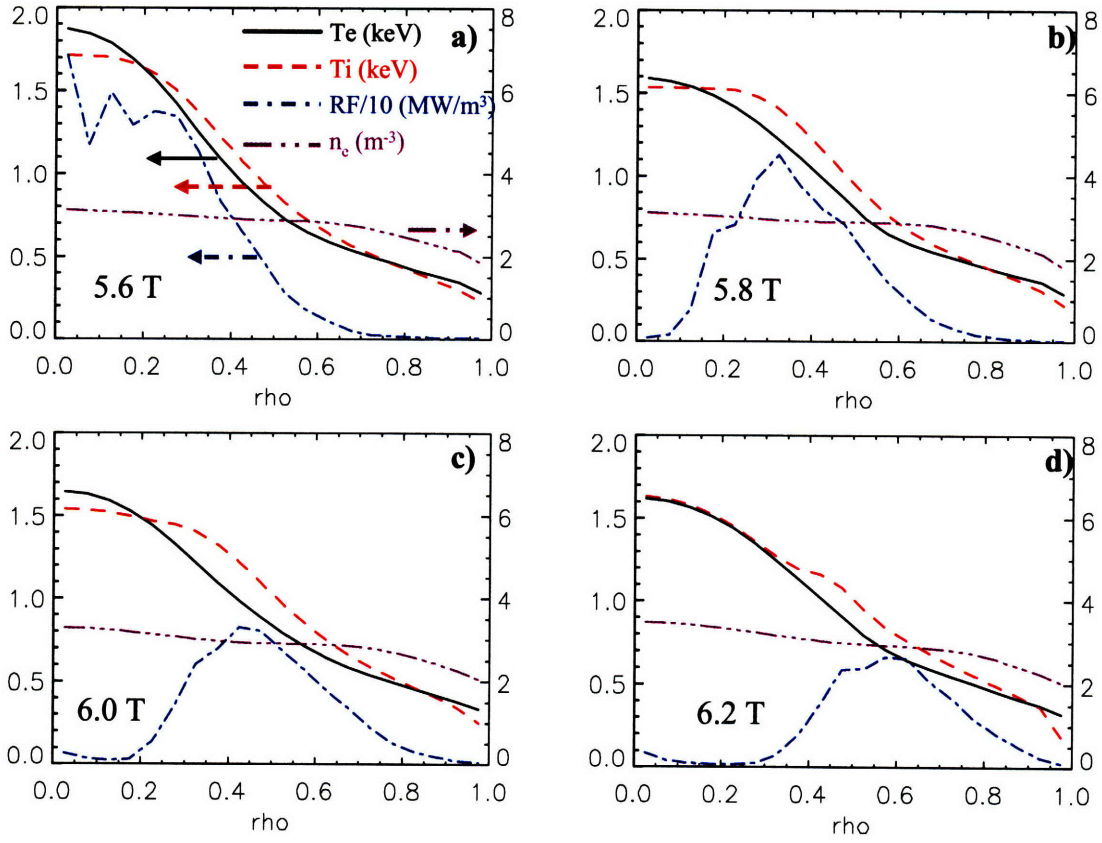

Figure 6-9: TRANSP calculations of ion temperature. Profiles are taken during H-mode (pre-ITB) phase of the discharges. Solid line - measured electron temperature; dashed line - calculated ion temperature; "— • —" - scaled ICRF power deposition profiles; "— • • • — " - measured electron density. The ion temperature profile flattens as the ICRF power deposition profile is moved outward, with the absolute deviation between T_i and T_e being small. The region of reduced T_i gradient moves with the ICRF resonance.

Profiles are plotted against square root of normalized toroidal flux $\rho = \sqrt{\overline{\psi}}$. Electron density profiles are similar for all discharges. The resultant ion temperature profiles (dashed line) are fairly close to the electron temperature (solid line), which is consistent with experimental observations and the fact that the high C-Mod density should lead to a strong coupling, giving good equilibration between ions and electrons.

The ion temperature profile measurements in this case were limited to the $T_i(0)$ values derived from the neutron rate measurements. However, these values are in good agreement with both measured $T_e(0)$ and TRANSP calculated $T_i(0)$. Fig. 6-9 demonstrates once again that changing the magnetic field indeed shifts the ICRF deposition profile. Furthermore, the modeled ion temperature profile gets broader as the ICRF resonance is moved outward, which is consistent with the experimental observations discussed previously. The discharge corresponding to Fig. 6-9(d) developed an ITB. The flat region of the ion temperature profile in this case shifts to r/a ~ 0.45, approximately the position where the ITB foot is seen later in the discharge.

To illustrate further and quantify this trend, the values of R/L_T for the ion temperature profiles of Fig. 6-9 have been calculated at the radial positions shown in Fig. 5-1(b). The results of these calculations are shown in Fig. 6-10, where the ITB and non-ITB regions are the same as in Fig. 5-4. As with the electron temperature profiles (compare with Fig. 5-4), R/L_{Ti} values exhibit a similar downward trend at or near the ITB foot location.

It should be noted that in these TRANSP simulations the coefficient κ in the χ_i formulation equals 8-10 during L-mode and decreases down to 2-4 during H-mode.

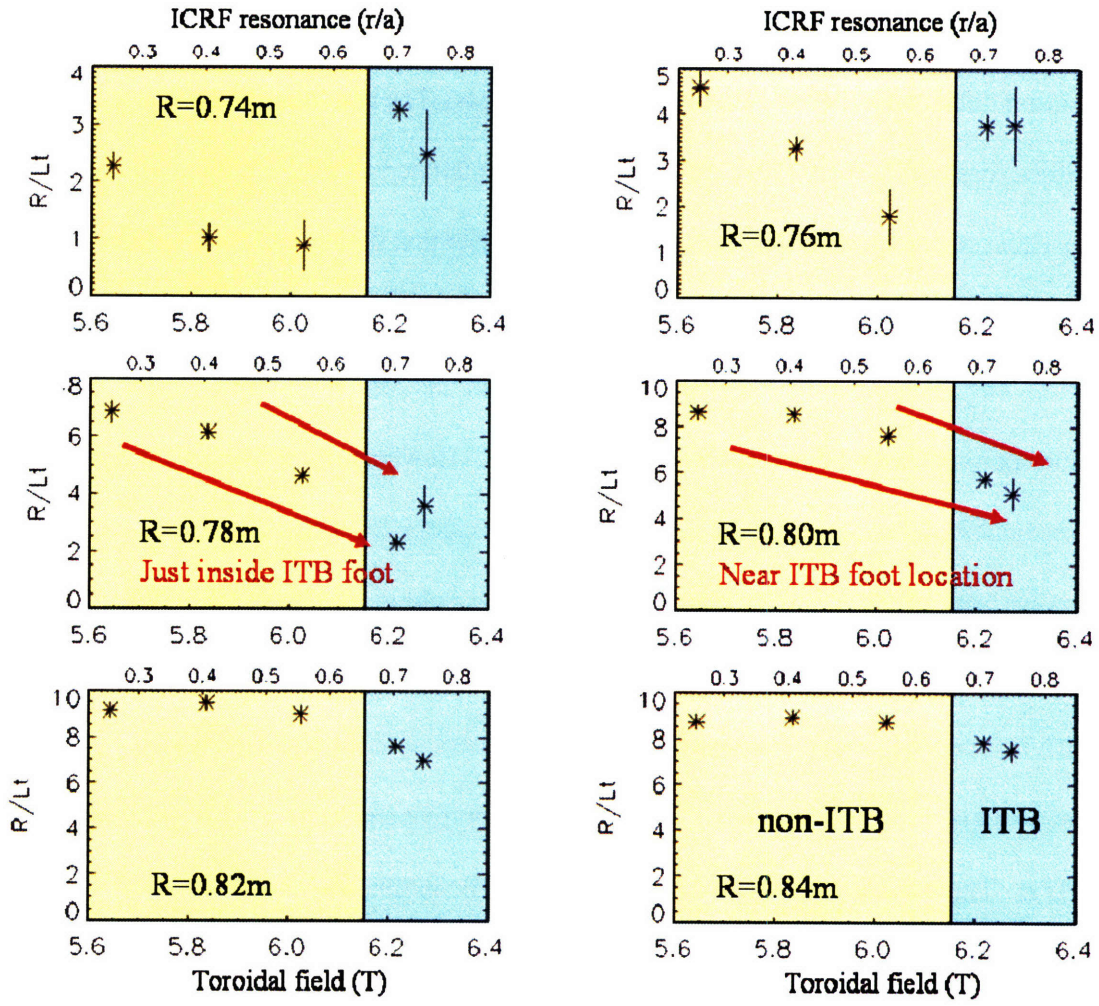

Figure 6-10: R/L_T for the ion temperature calculated at the indicated radial positions shown on Fig. 5-1(b). All values are calculated during H-mode (pre-ITB) phase. Ion temperature profiles are calculated by TRANSP and are shown in Fig. 6-9. The r/a position of the ICRF resonance is shown on the upper axis. The yellow region on each plot corresponds to non-ITB discharges, while the blue region contains discharges that developed ITBs. As with the electron temperature, there is a downward trend for R/L_T at positions at or near ITB foot location.

For certain discharges, especially the ones that developed an ITB, this coefficient drops down to and even below 1. This occurs primarily during the ITB phase of the discharge and is often seen in transport analyses for C-Mod ITB discharges, and in analyses of ITBs on other experiments. Varying certain plasma parameters such as impurity content, Z_{eff} or T_e within experimental errors changes the energy equilibration term between ions and electrons. This changes the values of κ and as a result of χ_i

necessary to produce such ion temperature that would lead to having the calculated neutron rate match the measured one. The resultant coefficient of proportionality, κ equals 1.5-2.5 during the pre-ITB phase in the H-modes for the discharges that developed ITBs. It is important to emphasize that as a result of these sensitivity studies, the overall trends for T_i being broader than T_e and the region of reduced gradient of T_i moving outward with the ICRF power deposition profile persist. It is also important to note that similar results for the ion temperature profiles and the same trend of profile widening with the ICRF outward shift is obtained if the model χ_i profile has the form $\chi_i = \kappa\chi_e$.

The particle diffusion coefficient is inversely proportional to the density gradient, which is relatively flat in the H-mode phase of the discharge. This makes the coefficient subject to large uncertainties and defeats the physical interest of deriving it from TRANSP calculations. The resultant thermal diffusion coefficients are shown in Fig. 6-11, where TRANSP calculations of the effective ($\chi_{eff} = (\chi_i n_i \nabla T_i + \chi_e n_e \nabla T_e)/(n_i \nabla T_i + n_e \nabla T_e)$, asterisks) and neoclassical (χ_{NC}, diamonds) thermal conductivities are plotted.

χ_{eff} remains well above neoclassical values across the whole plasma volume for the non-ITB discharge, while during the ITB it approaches neoclassical values inside the ITB foot, which is at r/a = 0.5. These profiles are consistent with previous C-Mod results [17, 18]. The drop in χ_{eff} inside the barrier foot to near neo-classical levels suggests once again that this ITB forms an energy barrier as well as a particle barrier.

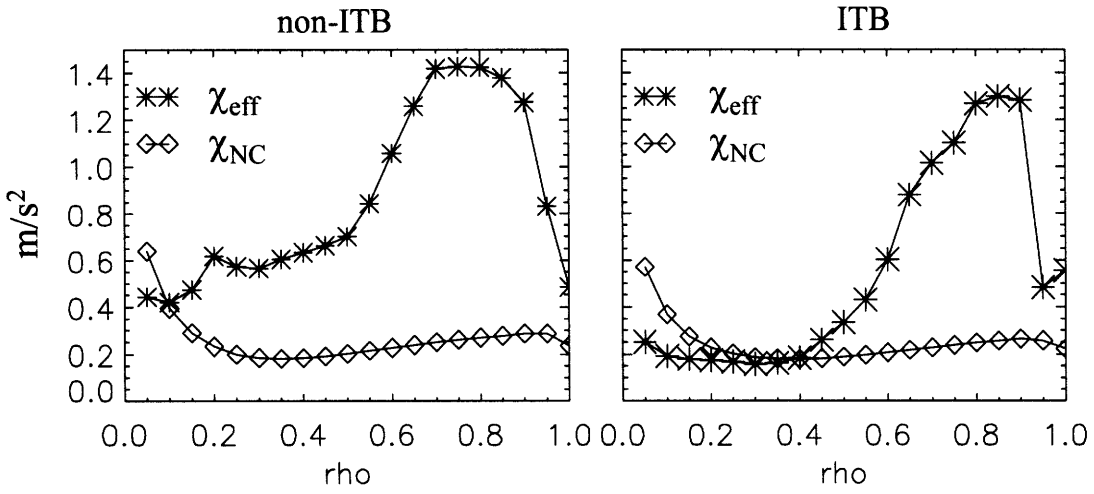

Figure 6-11: Radial profiles of the thermal transport coefficients as calculated by TRANSP for the non-ITB (left) and ITB (right). Effective thermal conductivity (asterisks) is significantly higher than neoclassical values (diamonds) across the whole plasma volume during the H-mode phase in the non-ITB discharge. However, it reaches neoclassical values inside the ITB foot during the ITB phase.

TRANSP simulations performed for the discharges from the current scan experiment support the trend that the magnetic shear is lower for the discharges that develop ITBs. This trend persists in the core plasma region even during the pre-ITB H-mode phase, which again suggests that the magnetic shear might play a stabilizing role in the ITB formation mechanism. Calculations of the ICRF power deposition profiles demonstrate that the ICRF heating location indeed shifts according to the magnetic field. The analysis of the power distribution between ions and electrons shows that approximately 50% more power goes to ions in the off-axis heated discharges. Therefore, there might be enough power for the ions to widen or flatten at least locally the ion temperature profiles during the off-axis heating scheme as suggested by the TRANSP T_i simulations. This can affect the stability of ITG modes which will be explored in the next chapter. The analysis of the effective thermal coefficients shows a

reduction to neo-classical level inside the ITB, which is consistent with the previous results and demonstrates that ITBs on C-Mod are thermal barriers as well.

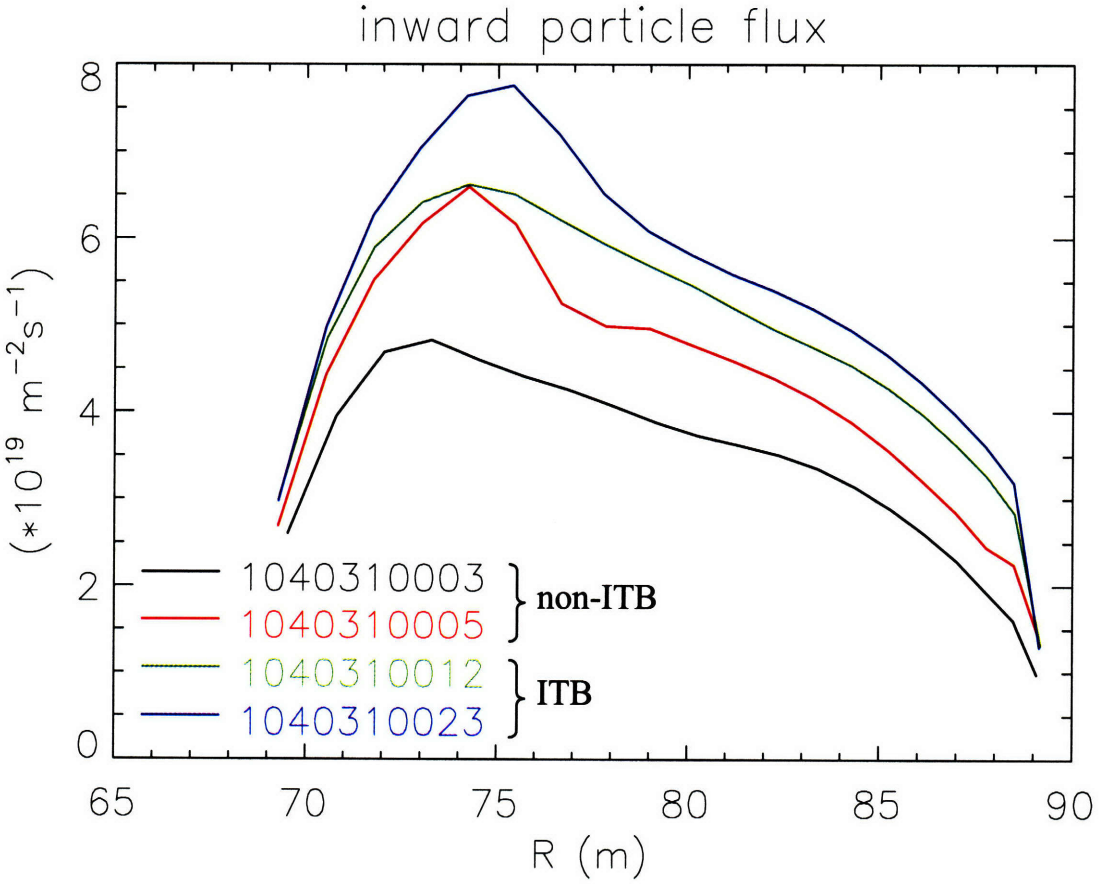

Figure 6-12: Inward particle flux as calculated by TRANSP at times corresponding to the H-Mode phase (pre-ITB for ITB discharges). Ware pinch is higher for the ITB discharges as a result of the higher H-mode density.

Transport analysis of the discharges from the current scan experiment reveals that the inward neoclassical particle pinch is stronger for the ITB discharges. This is a consequence of the higher H-mode density which in turn is a result of the higher plasma current. Fig. 6-12 shows Ware pinch profiles for the analyzed discharges at times corresponding to the pre-ITB phase of the H-mode. Moreover, careful analysis of the

ICRF power deposition profile reveals that it is slightly shifted outward for the ITB discharges, which is again a result of the higher plasma current and therefore, slightly higher total magnetic field. The latter suggest a temperature gradient link. Overall, these facts can explain the ultimate difference between ITB and non-ITB discharges in these experiments.

Finally it should be noted that TRANSP calculations are not performed in a sequence corresponding the results presented in this chapter. Instead all the calculations are done self-consistently in an iterative manner with multiple feedback loops, creating the final outputs.

References for Chapter 6

[1] R. J. Hawryluk, in *Physics of Plasmas Close to Thermonuclear Conditions*, edited by B. Coppi, G. G. Leotta, D. Pfirsch, R. Pozzoli, and E. Sindoni (Pergamon, Oxford, 1980), Vol. 1, p. 19.
[2] http://w3.pppl.gov/~pshare/help/transp.htm
[3] J. Schachter, Local Transport Analysis for the Alcator C-Mod Tokamak, PhD Thesis, MIT, 1997.
[4] J. W. Hughes, Edge Transport Barrier Studies On the Alcator C-Mod Tokamak, PhD Thesis, MIT, 2005.
[5] http://en.wikipedia.org/wiki/B-spline
[6] S. P. Hirshman, U. Schwenn, and J. Nuhrenberg, *J. Comput. Phys.* **87**, 396 (1990).
[7] E. S. Marmar, J. E. Rice, J. L. Terry, and F. H. Seguin, Nucl. Fusion **22**, 1567 (1982).
[8] E. S. Marmar *et al.*, Rev. Sci. Instrum. **72**, 940 (2001).
[9] B. B. Kadomtsev, Sov. J. Plasma Phys. **1**, 153 (1975).
[10] M. Brambilla, Plasma Phys. Cont. Fusion **41**, 1 (1999).
[11] T. D. Shepard *et al.*, Phys. Fluids B **3**, 1657 (1991).
[12] F. L. Hinton and R. D. Hazeltine, Rev. Mod. Phys. **48**, 239 (1976).
[13] A. A. Ware, Phys. Rev. Lett. **25**, 916 (1970).
[14] S. J. Wukitch *et al.*, Phys. Plasmas **9**, 2149 (2002).
[15] D. R. Ernst *et al.*, in Fusion Energy 2004 (*Proc. 20th IAEA Fusion Energy Conf.*, Vilamoura, 2004) (Vienna: IAEA) CD-ROM file TH/4-1 and http://www-naweb.iaea.org/napc/physics/fec/fec2004/datasets/index.html.
[16] C. S. Chang and F. L. Hinton, Phys. Fluids **25**, 1493 (1982).
[17] J. E. Rice *et al.*, Nucl. Fusion **42**, 510 (2002).
[18] C. L. Fiore *et al.*, Phys. Plasmas **11**, 2480 (2004).

Chapter 7

7 Gyrokinetic stability and transport analysis

Turbulence driven by micro-instabilities is believed to be responsible for the anomalous transport in tokamaks. Therefore, numerical simulations of these instabilities are desired to understand whether the plasma is stable to the microturbulent modes and, if these modes are unstable, to determine the resultant transport level. For this thesis research, such simulations were performed using the gyrokinetic code GS2. [1, 2]

7.1 GS2 code: geometry and model equations

7.1.1 Linear GS2 code

GS2 is a gyrokinetic stability code which numerically solves the gyrokinetic equation (4.2) including an appropriate collisional operator along with the quasineutrality condition. The linear version of GS2 was developed by Kotschenreuther *et al.* [1] The code solves for the distribution function using finite differences in time and parallel direction, but is spectral in the radial and perpendicular directions. Velocity space is discretized in energy and pitch angle. The energy grid is regular, while for circulating particles, the pitch angle grid is determined by Gaussian quadrature. For trapped particles, the pitch angles are selected so that each parallel spatial grid point is a turning point. A Lorentz collisional operator is used for pitch angle diffusion and the equilibrium distribution functions of all species are taken to be Maxwellian. Finite Larmor radius effects as well as kinetic effects from trapped particles and magnetic drifts are included.

The magnetic geometry can be numerically input from an equilibrium solver, or various analytic models can be used. Our simulations utilized the Miller equilibrium with specified elongation, Shafranov sshift, and triangularity for each flux surface.

In the simplest tokamak equilibrium model, the coordinate *r* defines the minor radius and θ and ζ are the poloidal and toroidal angles respectively. In this equilibrium model, the magnetic field is $B = B_0 /(1 + \varepsilon \cos(\theta))$, where ε = r/R, and R is the major radius of the center of the selected magnetic surface. Instabilities grow on the rational magnetic surfaces defined as $m = nq(r)$, where m and n are poloidal and toroidal mode numbers respectively, on which $k_{||} = 0$, and Landau damping is weakest. More generally, $k_{||}$ is given by $k_{||} = sk_\theta \frac{x}{L_s}$, where s is the magnetic shear with the corresponding scale length L_s and x is the distance from the rational magnetic surface. Increasing this distance increases ion Landau damping and therefore, causes the perturbed potential eigenfunction to decay. This causes the instability to center around the rational surfaces, creating a "modelet" at each surface. [3] In the ballooning representation, or approximation, all modelets are assumed to be identical, which is in essence a translational invariance in the radial direction. In the case of ballooning modes (high n number), the equations to be solved are reduced to one-dimensional equations (in coordinate space) along the magnetic field lines on any given magnetic surface through the so-called ballooning transformation [4]. This is essentially a Fourier representation in θ space. Individual modelets on successive rational surfaces are added up with the appropriate accounting for the phase shift between the surfaces, to form a ballooning mode. Using this representation, the perturbed electrostatic potential is expressed as [1]

$$\tilde{\Phi}(r,\theta,\zeta,t) = \exp[in(\zeta - q(r)\theta] \sum_{p=-\infty}^{\infty} \hat{\phi}(\theta - 2\pi p, r, t) \exp[inq(r) 2\pi p], \qquad (7.1)$$

where p labels the rational surfaces. $\hat{\phi}$ is defined in the infinite θ domain and $\tilde{\Phi}$ is periodic in the toroidal and poloidal angles. Then the linearized gyrokinetic equation for each plasma species s takes the form [1, Eq. 2]

$$\frac{\partial}{\partial t}\hat{g}_s + \frac{\mathrm{v}_{\|}}{qR}\frac{\partial}{\partial \theta}\hat{g}_s + i\omega_{ds}\hat{g}_s + C(\hat{g}_s) = \frac{e_s}{T_s}F_{ms}J_0\left(\frac{\partial}{\partial t} + i\omega_{*s}^T\right)\left[\hat{\phi}(\theta) - \frac{\mathrm{v}_{\|}}{c}\hat{A}_{\|}(\theta)\right], \qquad (7.2)$$

where $\hat{g}_s \equiv \hat{f}_s + (e_s / T_s)F_{ms}\hat{\phi}(\theta)$, F_{ms} is the Maxwellian part of the distribution function for species s, $\omega_{ds} = \omega_{*s}(L_{ns}/R)(E/T_s)(1 + \mathrm{v}_{\|}^2/\mathrm{v}^2)\{\cos\theta + [\hat{s}\theta - \alpha\sin\theta]\sin\theta\}$, $k_\theta = -nq/r$, $k_\perp = k_\theta\left\{1 + [\hat{s}\theta - \alpha\sin\theta]^2\right\}^{1/2}$, $\hat{s}$ is the magnetic shear, $\alpha \equiv -q^2 R(d\beta/dr)$, $\omega_{*s}^T \equiv \omega_{*s}\{[1 + \eta_s[(E/T_s) - 3/2]\}$, $J_0 \equiv J_0(k_\perp \mathrm{v}_\perp/\Omega_s)$, and the rest of the notation is standard. The collisional operator used in the GS2 code is a Lorentz operator

$$C(\hat{g}_e) = \frac{1}{2}\nu_e(E)\frac{\partial}{\partial \xi}(1 - \xi^2)\frac{\partial}{\partial \xi}\hat{g}_e \qquad (7.3)$$

where $\xi \equiv \mathrm{v}_{\|}/\mathrm{v}$, $\nu_e(E) \equiv [\nu_{ei}/(\mathrm{v}/\mathrm{v}_e)^3][Z_{eff} + H_{ee}(\mathrm{v}/\mathrm{v}_e)]$, v_e is the electron thermal velocity, and $H_{ee}(x) \equiv \exp(-x^2)/(\sqrt{\pi}x) + [1 - 1/(2x^2)]erf(x)$. A similar linearized operator is used for ions and impurities.

7.1.2 Non-linear GS2 code

The non-linear version of the GS2 code was developed by Dorland *et al.* [2]. This code employs a similar field-aligned coordinate system using toroidal flux tubes [5, 6], which is a convenient description for microturbulent drift modes that are highly elongated along and narrowly localized across the magnetic field lines ($k_{\|} << k_{\perp}$). In these coordinates the magnetic field can be written as

$$\mathbf{B} = \nabla\alpha \times \nabla\psi \tag{7.4}$$

Obviously, both α and ψ are constant on field lines and therefore, are natural coordinates for the flux tube. $\nabla\psi$ is perpendicular to the magnetic surface and ψ defines the flux surface. $\nabla\alpha$ is tangential to the magnetic surface and perpendicular to the magnetic field line and α defines the individual flux tube. [7] A third coordinate is the distance along the flux tube.

In such coordinates, the nonlinear gyrokinetic equation can be written as [5]

$$\left(\frac{d}{dt} + \mathrm{v}_{\|}\,\mathbf{b}\cdot\nabla + i\omega_d\right)\tilde{f} = i\omega_*^T\,\tilde{\chi} - e\frac{\partial F_0}{\partial\varepsilon}\frac{\partial\tilde{\chi}}{\partial t} \tag{7.5}$$

Here the distribution function $F_0 = F_0(\varepsilon,\psi)$ depends only on the energy $\varepsilon = m\mathrm{v}^2/2$ and the poloidal flux coordinate ψ. The total time derivative is given by $d_t = \partial_t + (c/B)[\tilde{\chi},\cdot]$, where $[\cdot,\cdot]$ denotes the Poisson bracket. The fields are represented by

$$\tilde{\chi} = J_0(\gamma)\left(\tilde{\phi} - \frac{\mathrm{v}_{\|}}{c}\tilde{A}_{\|}\right) + \frac{J_1(\gamma)}{\gamma}\frac{m\mathrm{v}_{\perp}^2}{e}\frac{\tilde{B}_{\|}}{B} \tag{7.6}$$

where $\gamma = k_\perp \mathrm{v}_\perp / \Omega$, $\omega_*^T = nc\partial_\psi F_0$, and n is the toroidal mode number of the perturbation. Eq. (7.5) describes the evolution of the fluctuations which satisfy

$$\frac{\tilde{f}}{F_0} \sim \frac{e\tilde{\phi}}{T} \sim \frac{\tilde{A}_\parallel}{B\rho} \sim \frac{\tilde{B}_\parallel}{B} \sim \frac{\omega}{\Omega} \sim \frac{\rho}{L} << 1,\ k_\parallel L \sim k_\perp \rho \sim 1 \tag{7.7}$$

as was discussed in chapter 4. The self-consistent electromagnetic field fluctuations are computed from the gyrokinetic Poisson-Ampere equations [5]

$$\nabla_\perp^2 \tilde{\phi} = 4\pi \sum_s e \int dv \left[e\tilde{\phi} \frac{\partial F_0}{\partial \varepsilon} + J_0(\gamma)\tilde{f} \right], \tag{7.8}$$

$$\nabla_\perp^2 \tilde{A}_\parallel = -\frac{4\pi}{c} \sum_s \int dv\, e\, \mathrm{v}_\parallel J_0(\gamma)\tilde{f}\ , \tag{7.9}$$

$$\frac{\tilde{B}_\parallel}{B} = -\frac{4\pi}{B^2} \sum_s \int dv\, m\, \mathrm{v}_\perp^2 \frac{J_1(\gamma)}{\gamma} \tilde{f}\ . \tag{7.10}$$

The simulations are done in a volume narrow in α and ψ space. Therefore, the variation of the equilibrium quantities across the flux tube is ignored.

The detailed description of the GS2 code and how to prepare runs is beyond the scope of this thesis. More details on that can be found in Refs. [1, 2, 5, 6, 8]

7.2 Linear GS2 analysis

In the previous chapters we identified some possible stabilizing mechanisms which might play an important role in triggering ITBs in C-Mod ICRF heated discharges. These are low magnetic shear and the observed broadening of the temperature profile. In order to assess the effects of these mechanisms on the diffusion caused by the microturbulent modes, stability analysis using the linear gyrokinetic code GS2 was

performed. Calculations were carried out on the MIT Plasma Science and Fusion Center Theory Group parallel computational cluster Marshall [9]. In this analysis, growth rate profiles of ITG/TEM/ETG modes were computed using profiles generated by the TRANSP calculations, utilizing the tools GS2_PREP and GS2_PLOT [8].

7.2.1 ITG growth rate profiles

Because they have longer wavelengths, ITG modes are the primary candidates for the anomalous transport in the C-Mod plasmas. First, in order to study the effect of the temperature gradient on the stability of ITG modes, linear GS2 analysis was performed for the discharges from the magnetic field scan experiment. Calculations were performed in a non-adiabatic electrostatic mode using four plasma species: electrons, deuterium, minority hydrogen, and boron as an impurity. In all cases, the stability analysis was done at the ITB onset time. The modes are characterized by normalized wave vectors, $0.1 \leq k_{\perp}\rho_i \leq 1$, where $k_{\perp}$ is the wave vector component perpendicular to the magnetic field line. In the spectrum analysis of the mode we found that the growth rate of ITG modes peaks at $k_{\perp}\rho_i \sim 0.3\text{-}0.4$ ($\rho_i = \sqrt{T_i / m_i} / \omega_{ci}$) for all of the analyzed discharges. Fig. 7-1 shows a typical ITG spectrum for an outer plasma region that is strongly unstable to ITG modes.

The resultant ITG growth rate profiles for the discharges from the magnetic field scan experiment are depicted in Fig. 7-2. Growth rates are plotted as a function of the normalized toroidal flux, ρ. Plasma profiles adopted for these gyrokinetic simulations are shown in Fig. 6-9. Profiles shown in Fig. 7-2 correspond to the different discharges each with a different magnetic field. In this particular case, the lower field corresponds to on-

axis heating, while higher field corresponds to more off-axis heating as can be seen from the Fig. 6-9.

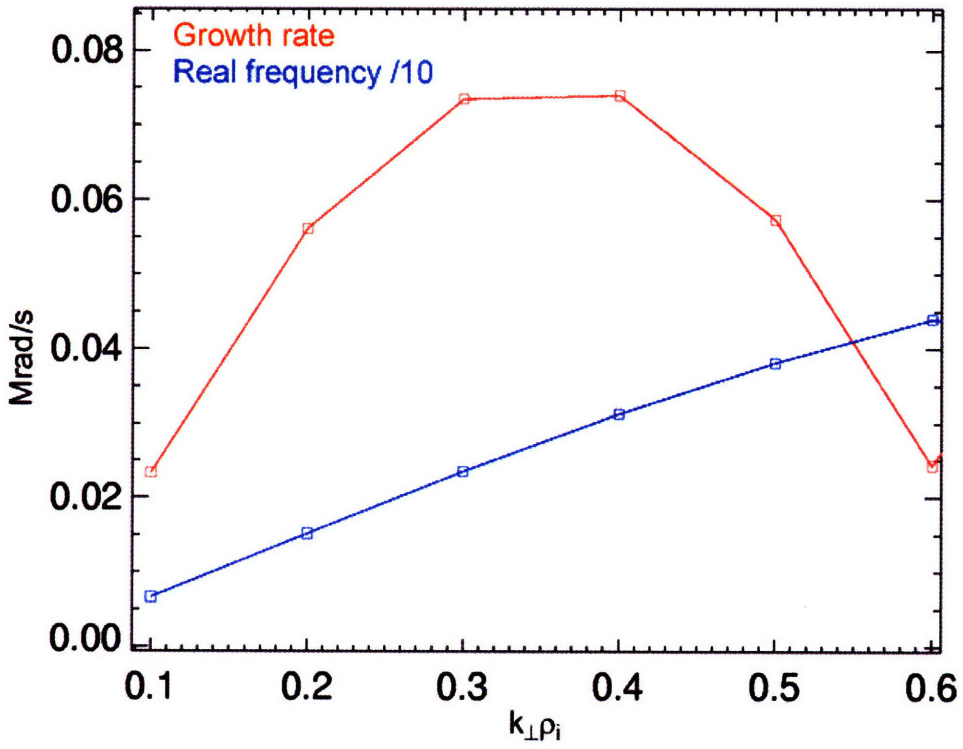

Figure 7-1: Linear growth rate and real frequency spectrum for ITG modes calculated at the ITB onset time for a radial position just outside ITB. ITG mode spectrum peaks at $k_\perp \rho_i \sim 0.3$-0. 4 for all of the analyzed discharges.

Fig. 7-2 shows that ITG modes are suppressed in the core plasma region and the region of stability to ITG modes gets wider as the ICRF resonance is moved outward. This analysis also suggests that the growth rate of ITG modes is systematically lower for the discharges that developed ITBs than that of the non-ITB discharges.

Moreover, the ITB foot is located at r/a ~ 0.5, approximately the location to which the stable region extends at higher field. This figure also suggests that one should expect a slightly broader ITB for 6.3 T discharge than for 6.2 T. However, electron density

profiles as measured by Thomson scattering system do not have enough spatial resolution to make a conclusive statement for such similar discharges.

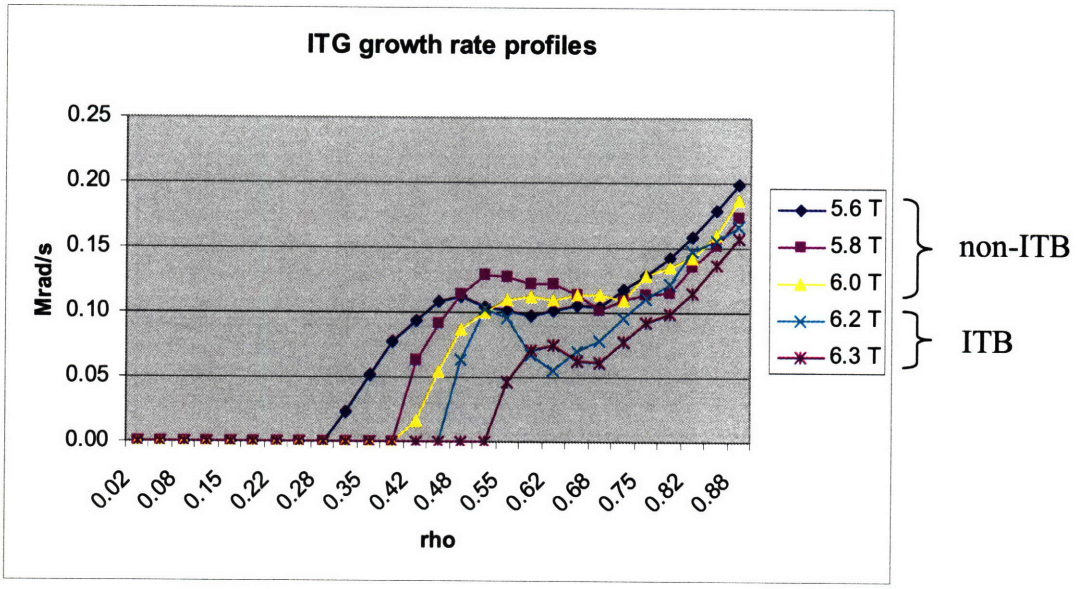

Figure 7-2: Linear ITG growth rate profiles calculated at ITB onset times for the discharges from the magnetic field scan experiment. Higher field corresponds to more off-axis heating. There is no ITG turbulence found in the core plasma region. The region of stability to ITG modes gets wider as the ICRF resonance is moved outward by changing the magnetic field. For ITB discharges it extends radially to approximately the location of the ITB foot. ITG growth rates are systematically lower for the discharges that developed ITBs.

The analysis of a broader dataset of C-Mod ITB discharges does not allow us to conclude that ITB foot is always located at exactly the position of the ICRF resonance either, since there are cases where the ITB is formed to the inside of the ICRF power deposition. Fig. 6-9(d) shows an example of that.

In order to assess the effect of the magnetic shear, similar GS2 stability analyses were performed for the discharges from the plasma current scan experiment. The results of the ITG growth rate calculations are plotted in Fig. 7-3. The spectra of the ITG modes for these runs are similar to the previous case. Different profiles in Fig. 7-3 correspond to the discharges with different plasma current. The results suggest that the region of

stability to ITG modes gets (marginally) wider with increasing plasma current. Also the ITG growth rates for the higher current discharges are somewhat lower.

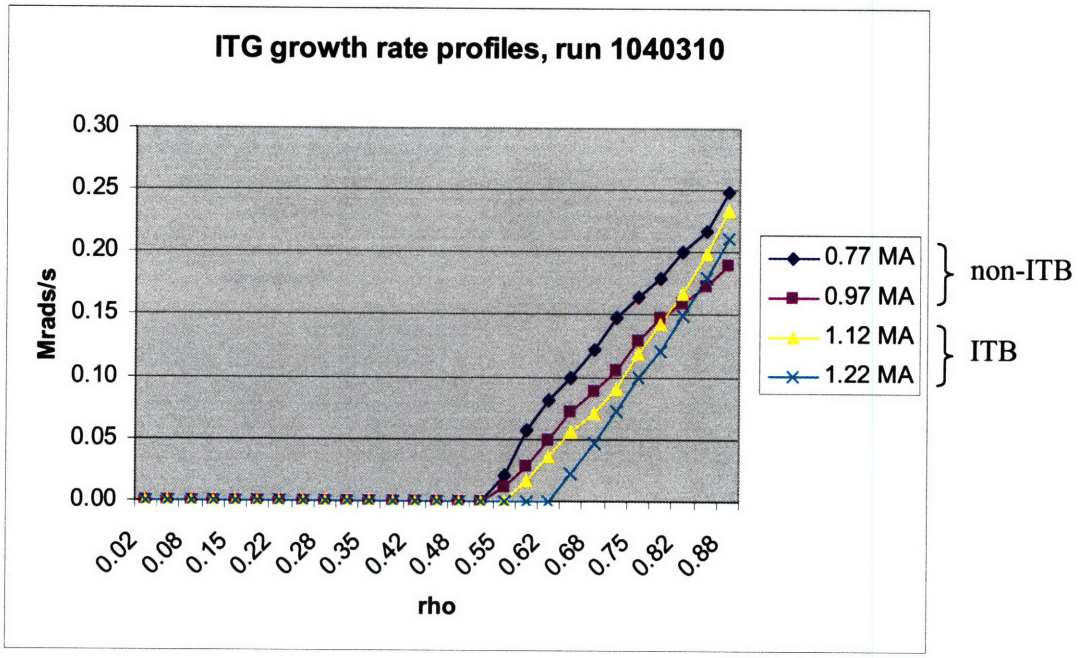

Figure 7-3: Linear ITG growth rate profiles calculated at ITB onset times for the discharges from the plasma current scan experiment. The region of stability to ITG modes gets wider with increasing the current. ITG growth rates are somewhat lower for the discharges that developed ITBs.

The dependence of the linear ITG growth rate on the magnetic shear was investigated through a systematic scan while keeping the rest of the plasma parameters intact. For that, several radial locations for the 1.1 MA discharge were chosen, for which the magnetic shear was multiplied by a set of factors ranging from -0.2 to 1.5. The results are shown in Fig. 7-4.

These results are in qualitative agreement with the gyrokinetic simulations done for DIII-D by Kinsey, Waltz, and Candy. [10] However, there is an upshift in the magnetic shear space compared to the DIII-D results, where ITG growth rate peaks at lower shear values. Moreover, this picture cannot explain the dependence of the ITB formation on the magnetic shear suggested by kinetic EFIT and TRANSP calculations.

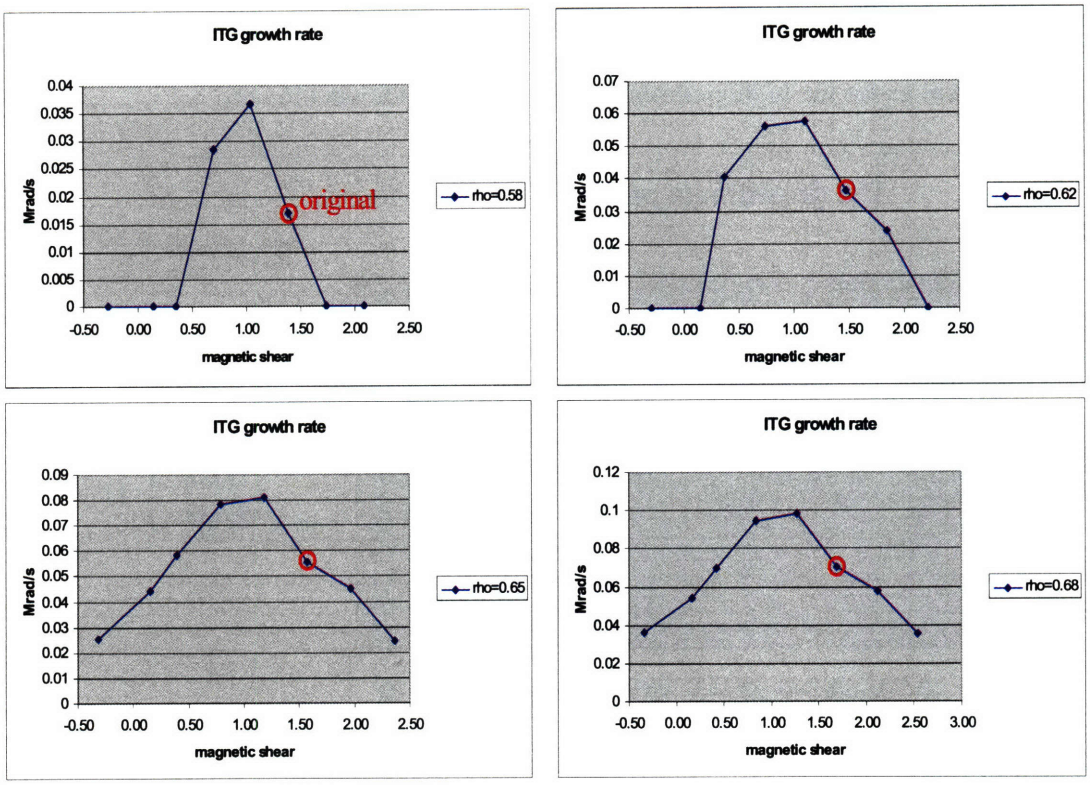

Figure 7-4: Linear ITG growth rates as a function of magnetic shear calculated at different radial positions for the 1.1 MA discharge. Marked are the original magnetic shear values.

First of all, the difference in the magnetic shear for ITB vs. non-ITB discharges calculated by kinetic EFIT and TRANSP is observed in the core plasma region that is stable to the ITG modes. This difference is minimal in the outer region where ITG modes are unstable. Furthermore, linear GS2 analysis suggests that if there is a dependence on the magnetic shear, then lowering its value should result in higher ITG turbulence level. This trend is in contradiction to the framework that ITB formation is related to the suppression of turbulent transport.

Even though kinetic EFIT and TRANSP calculations suggest a link between lower magnetic shear and ITB formation, so far we have not been able to back this hypothesis with linear GS2 calculations. It is possible that nonlinear GS2 calculations are

required to resolve this issue. At this stage C-Mod does not have a means of changing the magnetic shear in a controlled way. The machine also lacks a diagnostic for direct measurement of the magnetic shear. This complicates the analysis and hinders the direct testing of the hypothesis that the magnetic shear might play a role in triggering ITBs in C-Mod plasmas.

7.2.2 Linear critical gradient

Since for the flat density profile limit, the stability of ITG modes depends on the R/L_T value, it is instructive to calculate the critical value and estimate the proximity to this value. For this, profiles from the field scan experiments were used with the temperature gradients multiplied by a set a factors ranging from 1.2 to 3. Thus a set of ITG growth rate profiles was obtained for each case. Then for each radial position in each curve, linear interpolation of the ITG growth rate vs. the temperature gradient was used to derive the critical value. The results are plotted in Fig. 7-5.

This figure shows the comparison R/L_{Ti} values derived from the ion temperature profiles calculated by TRANSP (asterisks) and the critical gradient values estimated from linear GS2 analysis. Interestingly enough, the derived critical values are relatively constant and do not seem to depend on plasma parameters. It is seen that the region of reduced temperature gradients for which $R/L_T < R/L_T^{crit}$ extends further out for the high field, or conversely, off-axis heated discharges.

For more careful analysis of the critical linear threshold, two points on the opposite sides of the spatial region of interest near the location of ITB were chosen. The first point corresponds to $\rho = 0.32$ from a 5.6 T discharge, and the second point

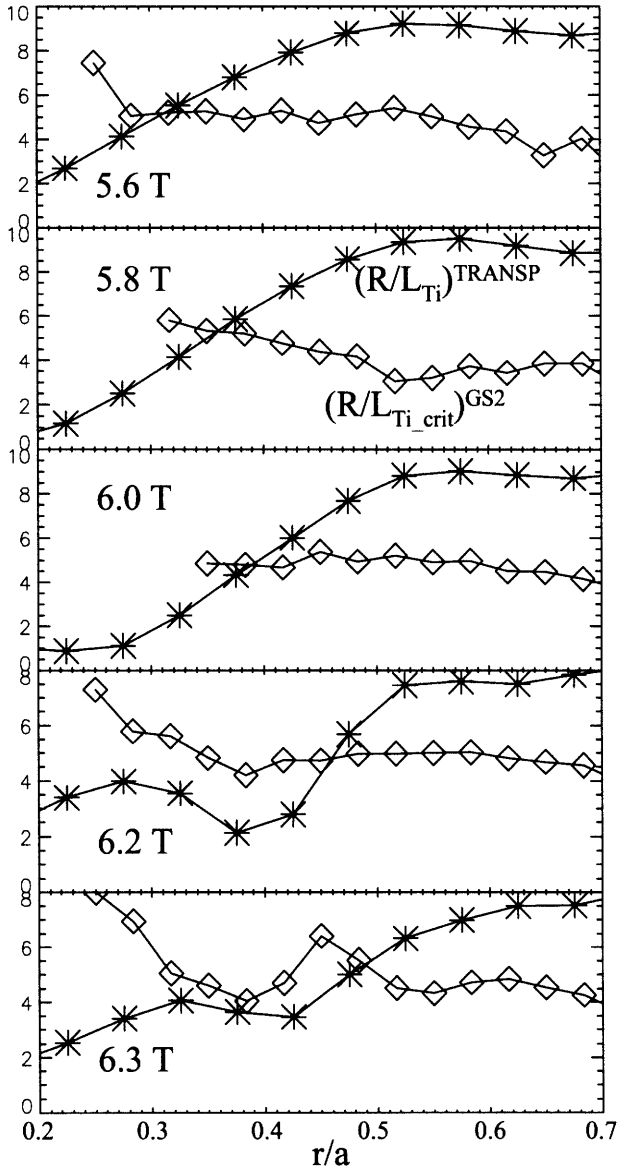

Figure 7-5: R/L_T for the ion temperature. Asterisks correspond to the R/L_{Ti} values derived for the ion temperature profiles calculated by TRANSP. Diamonds represent critical R/L_T values from linear GS2 analysis. The region of reduced gradient for which $R/L_T < R/L_T^{crit}$ extends further out for the high field, or conversely, off-axis heated discharges. The sawteeth inversion radius extends to r/a ~ 0.25.

corresponds to $\rho = 0.62$ from a 6.3 T discharge. The results are shown in Fig. 7-6. These runs were done with three ion species (deuterium, hydrogen, and boron) and adiabatic electrons in order to reduce the influence of the electron modes near marginal stability. Linear dependence is observed in the ITG growth rate as a function of the temperature

gradient, which enables us to derive the linear threshold for the ITG instability.The R/L_T^{crit} value is estimated to be 4.7 for the inner point and 4 for the outer point. The derived threshold is expected to be a complex function of plasma parameters, but its values are fairly close to the ones derived by the interpolation method (Fig. 7-5), which do not show much variation with the input parameters.

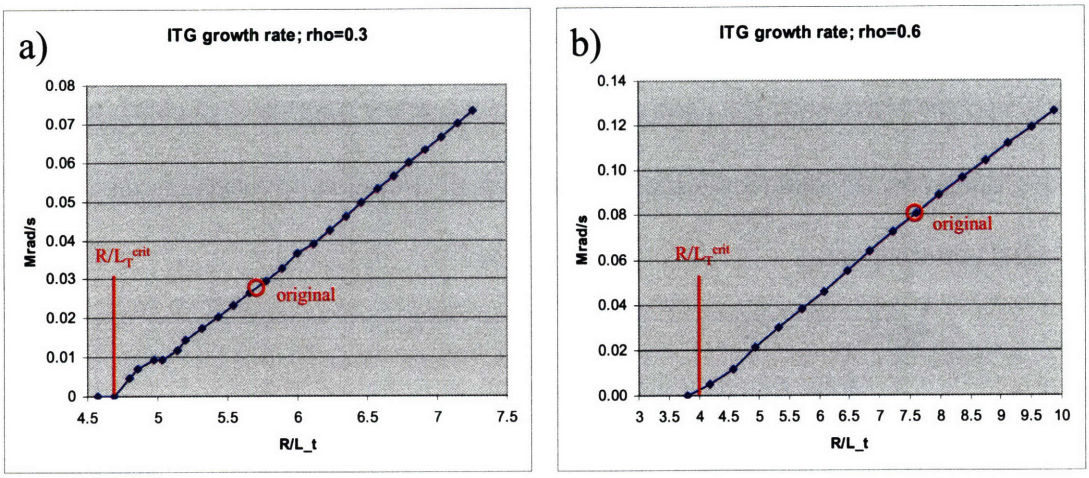

Figure 7-6: ITG growth rates as a function of R/L_T for a) 5.6 T discharge, $\rho = 0.3$; b) 6.3 T discharge, $\rho = 0.6$. Original values are marked in red. There is linear dependence of the ITG growth rates on the temperature gradient. The critical value of $R/L_T = 4.7$ is obtained for the inward point, while $R/L_T = 4$ for the outward point. The value of the temperature gradient for the outer point is further away from marginal stability, which is consistent with higher growth rate obtained in the linear GS2 calculations.

The value $\rho = 0.6$ corresponds to the third unstable radial zone for 6.3 T discharge in the linear GS2 calculations as can be seen from Fig. 7-2. It is further away from marginal stability than the $\rho = 0.3$ point, which corresponds to the first unstable zone for the 5.6 T discharge.

7.2.3 TEM/ETG growth rate profiles

Analysis of the electron modes for the above mentioned discharges has been performed as well. Fig. 7-7 shows a typical TEM/ETG pre-ITB spectrum for a position just outside of the ITB foot location. The spectrum for ETG modes usually peaks at $k_\perp \rho_i$ ~ 25, with a slight shift toward shorter wavelengths for radial positions closer to the plasma edge. The fastest growing ETG modes in our analysis usually have growth rates of 6-8 Mrads/s. No significant particle transport is expected from short-wavelength ETG modes, due to the adiabatic ion response, which results from ion-orbits averaging out the potential perturbations.

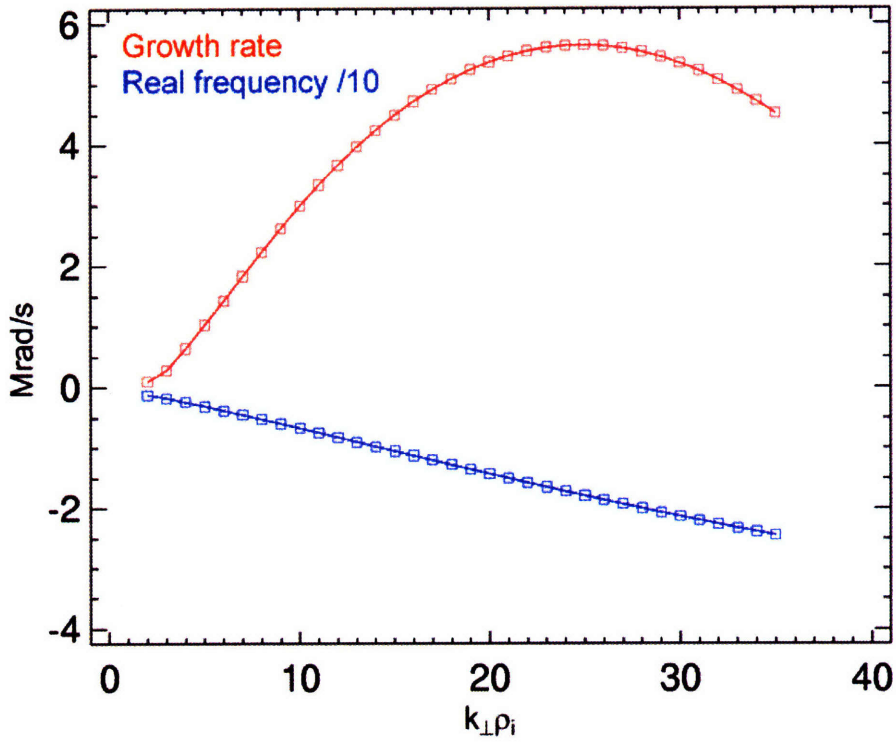

Figure 7-7: Linear growth rate and real frequency spectrum for TEM/ETG modes calculated at ITB onset time for a radial position just outside the ITB. The ETG mode spectrum usually peaks at $k_\perp \rho_i$ ~ 25 with a slight shift toward shorter wavelengths for positions closer to the plasma edge. The TEM range does not have distinct boundaries and corresponds to a longer wavelength part of the spectrum.

In Fig. 7-7 no clear or distinct contribution from trapped electron modes can be seen in the longer wavelength part of the spectrum. Standard mixing length arguments imply that the nonlinear saturation of these instabilities occurs when non-linear damping becomes comparable to the linear growth rate. This leads to a scaling of particle and thermal transport coefficients of $D, \chi \sim \Delta x^2 / \Delta t \sim \gamma / k_\perp^2$, where γ, $k_\perp$ are the growth rate and the perpendicular wave vector of the fastest growing mode. Comparison of growth rates and wave numbers of ITG and ETG modes leads to the conclusion that the contribution of the ETG modes to the overall transport on C-Mod is negligible. Of course, ETG turbulence may be highly anisotropic [2], resulting in transport levels much higher than mixing length estimates. Nevertheless, recent nonlinear ETG simulations that include ion dynamics show that ETG modes make only a small contribution to overall transport when ITG modes are unstable. [11] Further linear GS2 calculations for the C-Mod discharges do not reveal any difference between ETG growth rate profiles for ITB vs. non-ITB cases. Shown in Fig. 7-8 are the ETG growth rate profiles for the shots used in Fig. 7-2. Even though some variations in the profiles are observed, it is not possible to derive any systematic trend or make a clear distinction between ITB and non-ITB cases in the way that it can be done for ITG modes in Fig. 7-2. This suggests that the major difference in particle transport occurs due to suppression in ITG growth rates.

Further investigations were made to try to identify the electron mode. The potential candidates, TEMs and short-wavelength ETGs, respond differently to the electron temperature gradient and collisionality. Therefore, a few radial points from around the ITB region were chosen for the collisonality scan. First of all, setting

$\nabla T_e = 0$ makes the mode disappear, which excludes the density gradient driven TEM mode. Second, changing the collisionality within a wide range only marginally affects

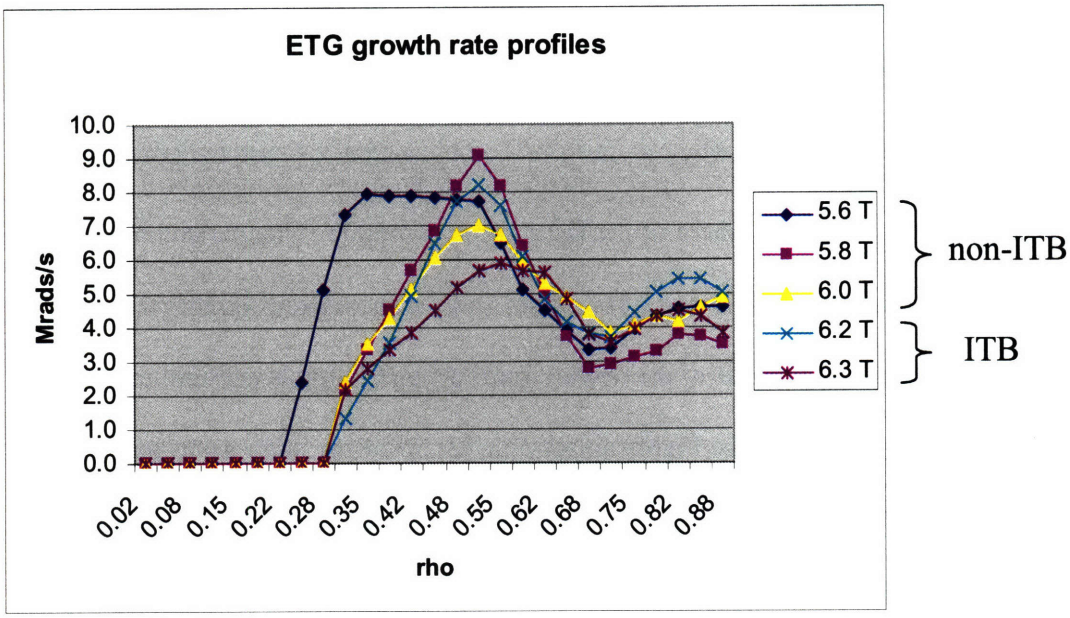

Figure 7-8: Linear ETG growth rate profiles calculated at ITB onset times. There is no clear difference between ETG growth rates corresponding to ITB vs. non-ITB discharges.

the mode's growth rate. This is expected for ETG but not TEM turbulence, since collisionality affects the particle trapping that is required for the trapped particle instability. The results of this exercise are shown in Fig. 7-9. The collisionality parameter adopted in GS2 runs is defined as $\nu^* = \nu_{ei} \frac{a}{v_t \sqrt{2}}$, where a is the minor radius. For this scan, the base case corresponds to $\nu^* = 0.25$, while for high and low collisionality this parameter equals 0.6 and 0.1 respectively. These runs suggest that the short wavelength electron mode observed in GS2 simulations is probably ETG.

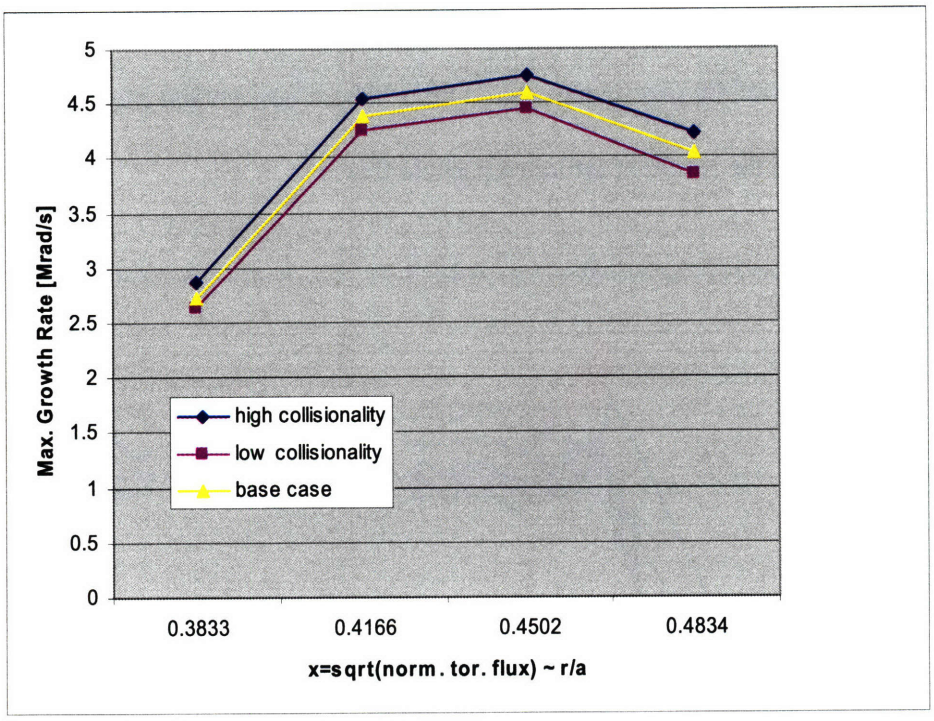

Figure 7-9: The electron mode's growth rate at selected radial positions in the region of ITB for different collisionality. The mode's growth rate is almost unaffected by changing collisionality within a wide range, which suggests that the observed mode is ETG rather than TEM.

7.3 Non-linear GS2 analysis

Non-linear gyrokinetic simulations are required to calculate the resultant diffusive particle flux. These calculations were performed for two radial points described in the previous section. Three plasma species (electron, deuterium, hydrogen) were used with the impurity density added to the major ion species to maintain quasineutrality. 10 poloidal modes were used spanning $0 \le k_\theta \rho_i \le 1$. Calculations were carried out on the computer cluster at the National Energy Research Scientific Computing Center. [12]

Fig. 7-10 shows the typical evolution of the electrostatic potential. Zonal flows which correspond to $k_\theta = 0$ (red curve on the plot) are driven by the primary instability

and compete with it, causing the non-linear saturation of the turbulence level. Each individual run advances 100-200 μsec in simulation time. Therefore, several runs are usually needed to estimate the resultant saturated particle flux.

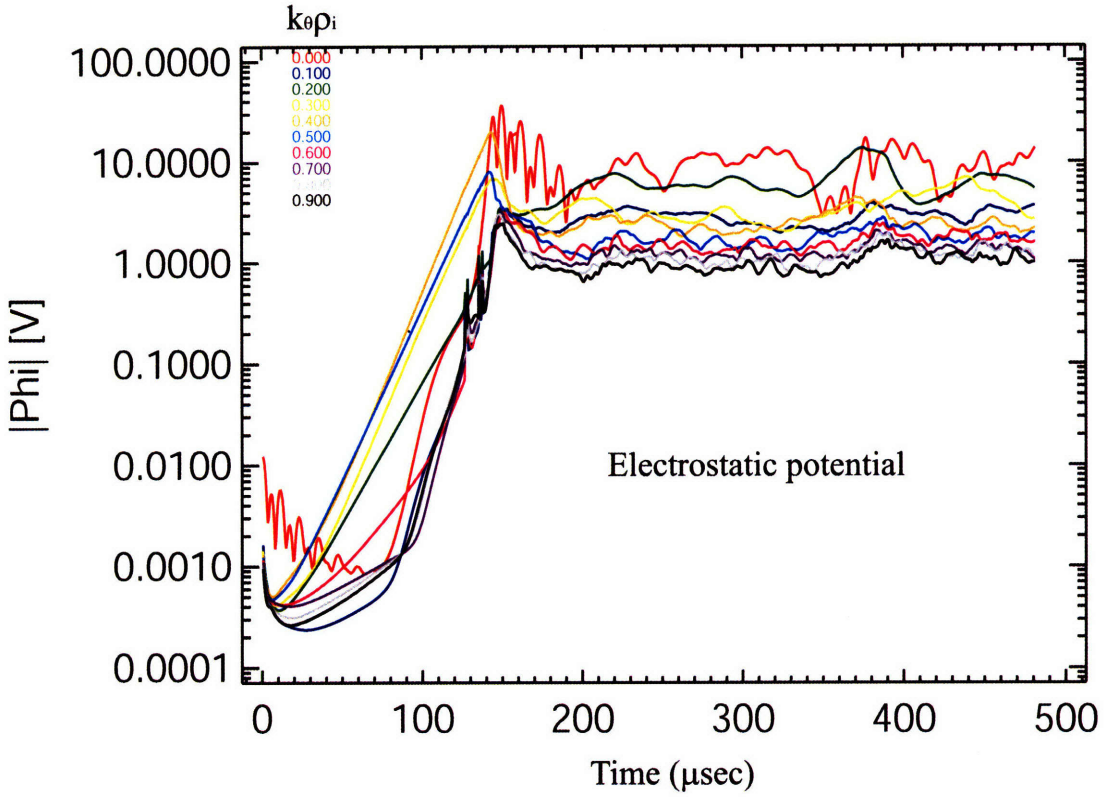

Figure 7-10: Evolution of the electrostatic potential. Zonal flows with k_θ=0 (red curve) grow on the primary instability and compete with it, causing the saturation of the turbulence level.

Fig. 7-11 depicts the evolution of the particle flux for each species. The resultant electron and ion fluxes are the same, while the total charge flux is zero as one would expect from quasineutrality. The flux itself is intermittent, which is an inherent property of the turbulence. Therefore, the run time has to be long enough to enable averaging over several bursts. Examples of a contribution of each poloidal harmonic to the overall particle flux and the resultant flux spectrum for a converged GS2 run are shown in Fig. 7-12.

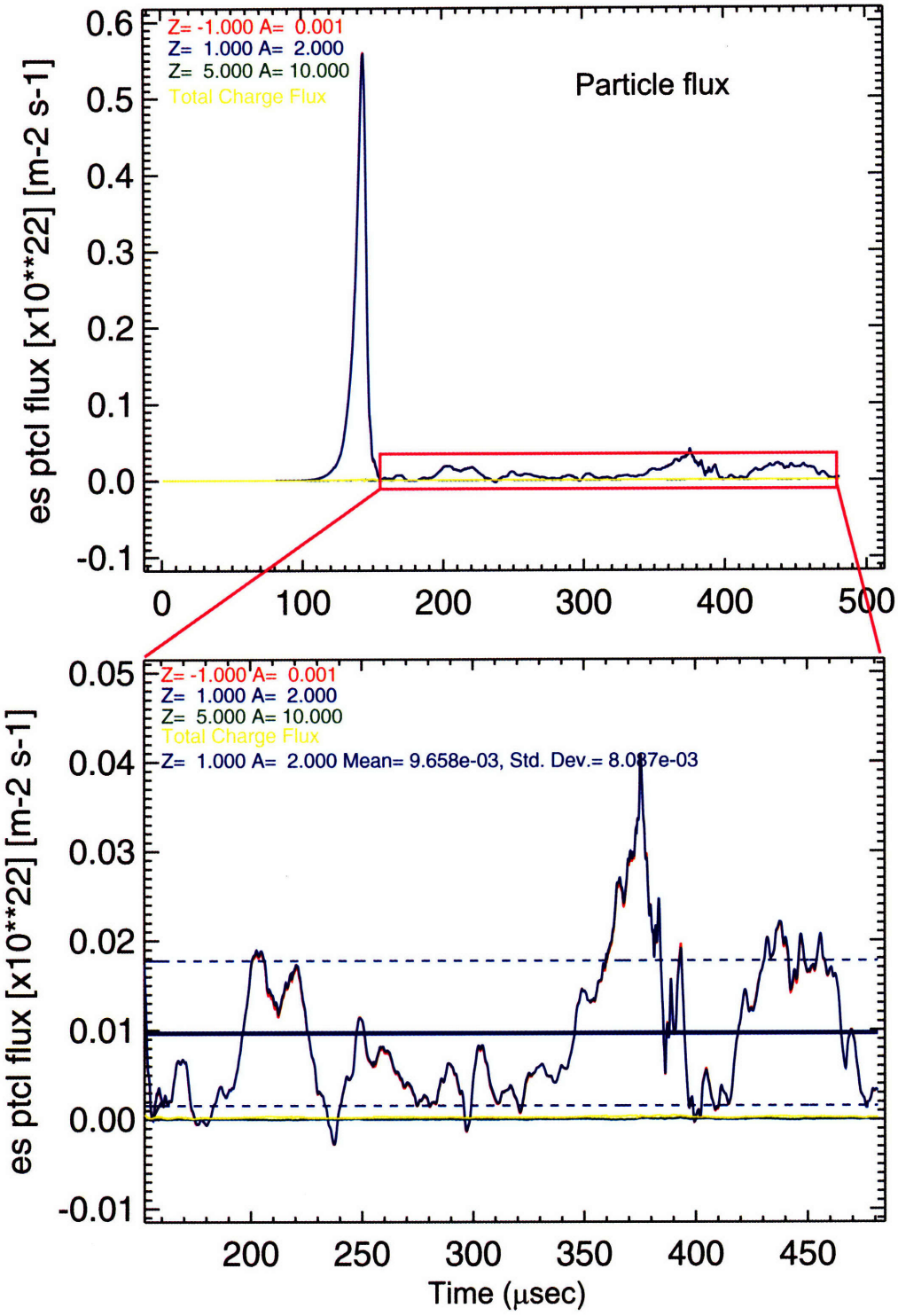

Figure 7-11: Evolution of the particle flux for each species. It is intermittent; therefore, long enough runs are needed to average over several bursts. Electron and ion fluxes are the same, and the resultant total charge flux is zero as one would expect.

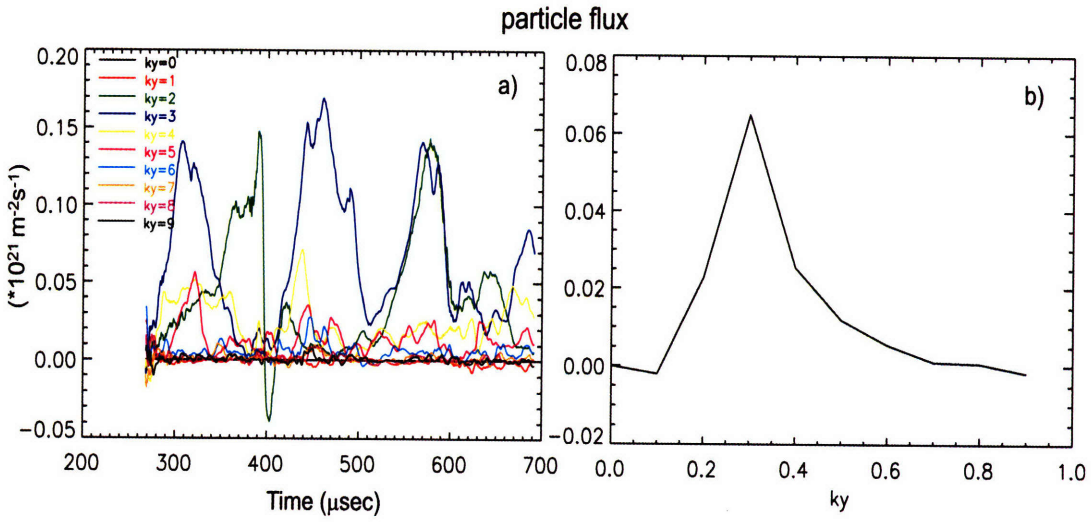

Figure 7-12: Contribution of poloidal harmonics to the overall particle flux (a) and the resultant spectrum of the flux (b). The spectrum peaks at $k_\perp \rho_i = 0.3$ (labeled ky on the plot) which corresponds to the fastest growing mode in the linear spectrum.

The outward diffusion flux for the $\rho = 0.6$ zone is estimated to be $\Gamma \sim 9.7 \times 10^{19}$ $m^{-2}s^{-1}$. This is comparable to the TRANSP estimate of the neoclassical inward particle flux for the same time phase and radial position. The latter is estimated to be $\Gamma \sim 4.5 \times 10^{19}$ $m^{-2}s^{-1}$. This is consistent with the expectations that the zone outside the transport barrier is dominated by the outward diffusion. The analysis of the Ware pinch reveals that it increases slightly towards the center, while the turbulence driven outward flux is expected to decrease according to the ITG growth rate profiles in Fig. 7-2. A two-fold decrease of the outward flux as a result of the flattening of the temperature profile is sufficient for the Ware pinch to overcome the diffusive term and peak the density profile. The result of comparison of the inward and outward particle fluxes is similar to the previous C-Mod results [13, 14], which suggest that the inward pinch on C-Mod is strong enough to cause a peaked density profile.

Fig. 7-11 shows a base case, where plasma parameters were taken directly from the TRANSP results. In order to assess how the turbulent flux changes with the temperature gradient, a systematic scan has been performed. Fig. 7-13 shows the particle flux as a function of R/L_T for the $\rho = 0.6$ zone of the 6.3 T discharge. During this scan the temperature gradients of all species were scaled by the same factor, while all other plasma parameters were kept intact. The time corresponds to the pre-ITB phase of the H-mode as before. Fig. 7-13 enables us to estimate the non-linear threshold for the instability, which in this case is $R/L_T^{crit} \approx 4.8$. The difference between non-linear and linear critical temperature gradients is a 'Dimits shift' [15], which in this case constitutes ~ 20%.

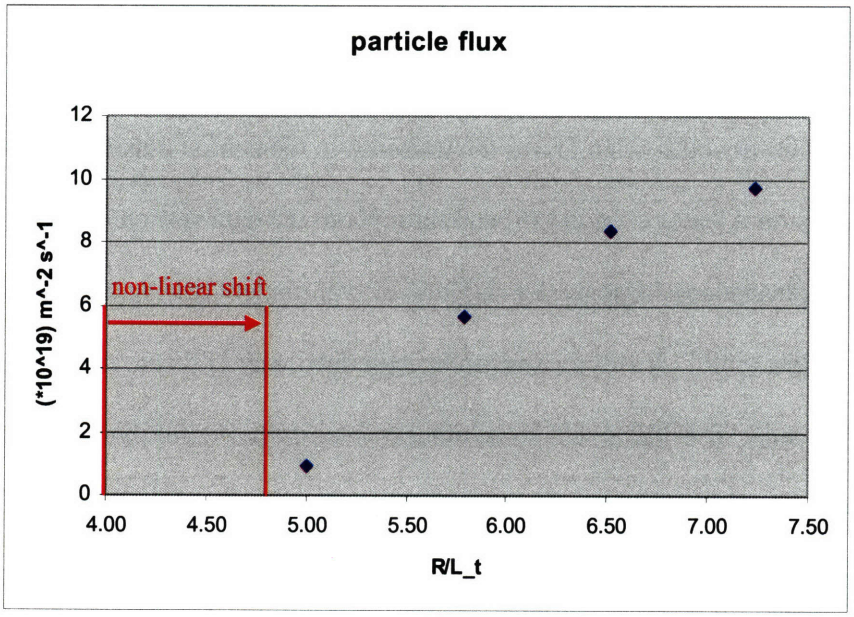

Figure 7-13: Particle flux as a function of R/L_T as calculated by non-linear GS2. Temperature gradients of all species were scaled by the same factor, while all other plasma parameters were kept intact and corresponded to pre-ITB values. The estimated R/L_T^{crit} is about 4.8.

It turns out that the $\rho = 0.3$ point from the 5.6 T discharge is very close to marginal stability, which is expected since it is the first unstable zone for this discharge

even in the linear gyrokinetic simulations. Therefore, a 10% decrease in the temperature gradient results in virtually zero particle flux and no non-linear critical temperature gradient is obtained for this zone. The particle flux estimated for the base case is $\Gamma \sim 2.1 \times 10^{19}$ $m^{-2}s^{-1}$, which is smaller than the $\rho = 0.6$ case and is consistent with the linear results.

Another non-linear simulation was done for $\rho = 0.48$ from the 6.0 T discharge. This radial position corresponds to the barrier region. The resultant particle flux for this point is $\Gamma \sim 11 \times 10^{19}$ $m^{-2}s^{-1}$, which is higher than the previous two values and again is consistent with the linear results.

7.4 Discussion and summary

It is not entirely clear what drives the transport in the central plasma region. Stability analysis on Alcator C-Mod [16] and throughout the database on other machines [17] shows that plasma core is generally stable to microturbulent drift modes to relatively large r/a values ($r/a \geq 0.5$). It still remains to be explained why ITBs are not seen all the times at smaller radii. It is likely that some other transport driving mechanisms are at play in the inner part of the plasma that do not allow the density to peak in the core region where the plasma is predicted to be stable to ITG modes. The potential candidate for C-Mod could be the transport induced by sawtooth oscillations. In all cases, the ITB foot is located outside the sawtooth inversion radius and there is gap between sawtoothing and ITG-unstable regions. However, as was pointed out before, the sawteeth are definitely more pronounced for on-axis heated discharges with larger temperature perturbations outside the inversion radius. GS2 analysis reveals that increasing

temperature gradients by ~ 50-100 %, which is not unreasonable for the region just outside the sawtooth inversion radius, helps close this gap for on-axis heated discharges. This might help explain the fact that ITBs on C-Mod are obtained only in the discharges with off-axis ICRF heating.

Non-linear GS2 simulations reveal another interesting effect. Although no anomalous pitch is observed for the experimental input parameters considered, increasing the temperature gradients for all species leads to a particle pinch. The pinch does not seem to be affected by changes in the density gradients. The nature of this pinch is not well-understood and more non-linear gyrokinetic simulations are required to address its relevance for C-Mod high density plasmas. The simulations suggest that the particle pinch is associated with shorter wavelengths. This points to the need to include more poloidal modes in the spectrum and therefore, much more computational power is needed to address the issue.

Linear gyrokinetic simulations suggest that anomalous transport on C-Mod is dominated by ITG modes. They also reveal that the region of stability to ITG modes gets wider as the ICRF resonance is moved off-axis. The resultant diffusive particle flux is consistent with the neoclassical inward pinch calculated by TRANSP. Overall, gyrokinetic simulations seem to support the framework that suppression of ITG turbulence is one of the key mechanisms in triggering ITBs in C-Mod off-axis ICRF heated discharges. The role of the magnetic shear is harder to assess through gyrokinetic simulations, since all evidences suggest that the magnetic shear for ITB and non-ITB discharges is similar in the region unstable to ITG.

Some of the results of the gyrokinetic and TRANSP analysis presented here can be found in Ref. [18].

References for Chapter 7

[1] M. Kotschenreuther, G. Rewoldt, and W. M. Tang, Comput. Phys. Commun, **88**, 128 (1995).
[2] W. Dorland *et al.*, Phys. Rev. Lett. **85**, 5579 (2000).
[3] J. W. Connor and R. J. Hastie, Plasma Phys. Control. Fusion **46**, 1501 (2004).
[4] J. W. Connor, R. J. Hastie, and J. B. Taylor, Phys. Rev. Lett. **40**, 396 (1978).
[5] http://gs2.sourceforge.net
[6] M. A. Beer, *Gyrofluid Models of Turbulent Transport in Tokamaks*, PhD Thesis, Princeton University (1994).
[7] D. R. Ernst *et al.*, *Int. Sherwood Fusion Theory Conf.*, Annapolis, Maryland, USA April 22-24, 2007.
[8] D. R. Ernst *et al.*, Phys. Plasmas **7**, 615 (2000).
[9] http://marshall.psfc.mit.edu/
[10] http://fusion.gat.com/~kinsey/gyrodb/gyro-database.pdf; also J.E. Kinsey, R. E. Waltz, and J. Candy, *The Effect of Safety Factor and Magnetic Shear on Turbulent Transport in Nonlinear Gyrokinetic Simulations*, submitted to Phys. Plasmas.
[11] J. Candy and R. E. Waltz, in Fusion Energy 2006 (*Proc. 21st IAEA Fusion Energy Conf.*, Chengdu, 2006) (Vienna: IAEA) CD-ROM file TH/2-1 and http://www-naweb.iaea.org/napc/physics/fec/fec2006/html/index.html.
[12] http://www.nersc.gov/
[13] S. J. Wukitch *et al.*, Phys. Plasmas **9**, 2149 (2002).
[14] D. R. Ernst *et al.*, in Fusion Energy 2004 (*Proc. 20th IAEA Fusion Energy Conf.*, Vilamoura, 2004) (Vienna: IAEA) CD-ROM file TH/4-1 and http://www-naweb.iaea.org/napc/physics/fec/fec2004/datasets/index.html. Also D. R. Ernst *et al.*, Phys. Plasmas **11**, 2637 (2004).
[15] A. M. Dimits *et al.*, Phys. Plasmas **7**, 969 (2000).
[16] M. H. Redi *et al.*, Phys. Plasmas **12**, 072519 (2005).
[17] M. Romanelli, C. Bourdelle, and W. Dorland, Phys. Plasmas **11**, 3845 (2004).
[18] K. Zhurovich *et al., Microturbulent drift mode suppression as a trigger mechanism for internal transport barriers on Alcator C-Mod*, accepted for publication in Nucl. Fusion.

Chapter 8

8 Conclusions and future work

The work described in this thesis contributed to the study of the physics behind the formation mechanisms of internal transport barriers on the Alcator C-Mod tokamak. Because transport barriers lead to improved confinement regimes with ultimately higher fusion yield, it is an important topic for the development of fusion reactors as a source of energy.

A number of significant contributions to the scientific community in general and to the C-Mod group in particular were made as a result of this thesis research. First of all, a new core Thomson scattering diagnostic installed on C-Mod in 2002 significantly improved measurements of plasma density and temperature profiles as described in Ch. 3. It almost doubled the spatial resolution of the existing system and related laboratory work resulted in doubling of the time resolution as well. Now this system routinely provides reliable n_e and T_e measurements over the entire range of C-Mod plasma parameters, giving ~1 cm midplane resolution in the region of the ITB, and having an option to study fast (~1 ms) transient phenomena in the plasma. A new method of absolute calibration of TS systems was pioneered over the course of the thesis work. This method has several advantages over standard techniques and should be easy to deploy on other tokamaks. In Ch. 3, it is shown that supplementing TS measurements with data obtained from the Visible Bremsstrahlung diagnostic allows the derivation of the effective plasma charge profiles. Overall, the new core TS system on C-Mod proved to be a successful project, which paved the way for another diagnostic upgrade currently being installed. An

increased number of channels should allow us to better determine the position of the ITB foot and to perform parametric studies to determine the dependence of the foot location on plasma parameters.

The necessity of using TS and other diagnostics measurements for transport analysis and simulations resulted in the creation of software tools for data fitting. The resultant smooth n_e and T_e profiles are used in TRANSP and subsequently in GS2 simulations. As described in Ch. 6 and the Appendix, density and temperature fitting packages give a user a wide variety of options for data processing and fitting. These are widely used by the C-Mod group and collaborators.

The ITB formation has always been linked to the suppression of instabilities, among which microturbulent drift modes are the primary candidates for the anomalous transport in tokamaks. ITBs on C-Mod are routinely produced in EDA H-mode plasmas by putting the ICRF heating location off-axis. The working hypothesis for this thesis research was that the ITB formation can be explained within a paradigm of marginal stability. Shifting the ICRF resonance location off-axis can result in broader temperature profiles. Flattening (even local) of the temperature profile can decrease the drive for the temperature gradient driven instabilities and significantly reduce the outward diffusive flux. As described in Ch. 5, several sets of experiments were undertaken on C-Mod over the course of the thesis work to test this hypothesis experimentally. Magnetic field scan experiments, which allowed a systematic scan of the ICRF heating location, successfully demonstrated that both the electron and ion temperature profiles broaden when the ICRF resonance is shifted outward. Another experiment involved changing the heating scheme from on-axis to off-axis during a plasma discharge. The analysis of the electron

temperature profiles for this experiment also revealed flattening in the region of ITB. Overall, there is enough experimental evidence to suggest a link between an outward shift of the ICRF resonance location, temperature broadening or flattening, and ITB formation in C-Mod ICRF heated plasmas. However, more detailed measurements of the ion temperature profiles are desired. They will be possible for the future experiments thanks to a recent diagnostic upgrade on C-Mod.

Numerous transport analyses and simulations were performed over the course of the thesis research using the widely used transport analysis code TRANSP as described in Ch. 6. Among many other things, it allowed us to calculate the deposition profile of the ICRF power, the heating power distribution between ions and electrons, and to model ion temperature profiles based on the measured neutron rate. TRANSP calculations supported experimental evidence that shifting the ICRF heating location outward flattens the ion temperature profiles. They also demonstrated that more ICRF power goes to ions during the off-axis heated discharges, which can facilitate T_i flattening. Different minority fractions can be used in future experiments to change the power partition between ions and electrons and study the effect on the temperature gradients.

Gyrokinetic stability analysis was performed using the GS2 code as described in Ch. 7. Linear GS2 analysis suggested that anomalous transport on C-Mod is dominated by ion temperature gradient driven modes. It also revealed that the region of stability to ITG modes gets wider as the ICRF resonance is moved outward. Critical gradient analysis supported this trend. Non-linear GS2 calculations showed that outward diffusive particle flux is of the order of the inward neoclassical pinch and dominates it in the outer plasma region, which is strongly unstable to the ITG modes. These calculations

demonstrated that decreasing the temperature gradient indeed results in a significant reduction of the transport, which helps explain the formation of the peaked density profiles.

It is still to be explained what drives the transport in the plasma core. The results from C-Mod and the database from other machines show that typically the plasma center is strongly stable to the drift modes to a relatively large radius ($r/a \geq 0.5$). It is likely that the core transport on C-Mod is dominated by the sawteeth that are usually present. Further transport calculations will be the subject of future research. Also many more non-linear gyrokinetic calculations are desired to better understand the dependence of the turbulence level on the plasma parameters. This will be possible with the upgrade of the Marshall Theory Group computer cluster at the Plasma Science and Fusion Center, MIT.

A set of plasma current scan experiments were also done to study the dependence of the ITB formation on current. Analysis using kinetically constrained EFIT magnetic reconstruction revealed that the magnetic shear was systematically lower in the core plasma region for the discharges that developed ITBs. Equilibrium reconstruction by TRANSP supported this trend. This suggested that on C-Mod, low magnetic shear can play stabilizing role similar to that found on other machines. However, the trend was observed in the core plasma region that is already stable to ITG turbulence, which makes it difficult to perform a systematic analysis with gyrokinetic simulation. Unfortunately, currently C-Mod lacks a diagnostic for direct q profile measurements, which complicates the analysis of the role of the magnetic shear. The corresponding diagnostic for such measurements will be available for future experiments. Also up to date C-Mod did not have means for active control of plasma current and consequently, q profiles. A newly

installed lower hybrid RF system should allow us to perform experiments to test the effect of the q profile and magnetic shear on ITB formation on Alcator C-Mod.

Even though this thesis is to a large extent a result of the author's work, it, naturally, benefited at every step from the assistance and guidance of many colleagues, specifically acknowledged in the corresponding section.

Appendix A

Profiles mapping and fitting

Use of the TRANSP code requires smooth radial profiles for density and temperature. The fiTS program was developed to provide these. This is an upgrade of the fitting routines also known as fit_ne and fit_te, which were previously developed in collaboration with Darin Ernst. The fiTS code has a graphical user interface (GUI) and therefore, has more powerful visualization capabilities as well as wider range of options for data processing and fitting. This GUI was coded by MIT UROP students Eric Grebing and David Ely. The fitting algorithm remained unchanged, and it is the GUI that will be described here.

fiTS consists of two major components: density and temperature fitting. Upon loading a valid C-Mod shot, for which TS and EFIT data are available, fitted n_e and T_e profiles are produced automatically using the default parameters. These parameters were optimized based on prior experience and common sense. A user can then look at the resultant profiles for each individual time slice and change the parameters of the fit if necessary. The code gives the user the option to choose between different EFIT trees for the equilibrium data (the default is the ANALYSIS tree). Also during the loading phase a user can skip (default setting) remapping of ECE data used for the T_e profiles onto the low field side (LFS) along constant poloidal flux surfaces. All the data used for the fitting together with the resultant profiles can be saved in a file and easily restored from the widget.

A.1 Fitting of density profiles

For the density fitting, measurements from the core and edge TS systems are used. Visible bremsstrahlung (profiles of $n_e\sqrt{Z_{eff}}$) profiles are used to help identify the ITB phase of the discharge. Several criteria for the profile curvature, peaking, height, and the ITB foot location were adopted for this purpose. VB data are also used together with the derived n_e profiles to obtain profiles of Z_{eff}.

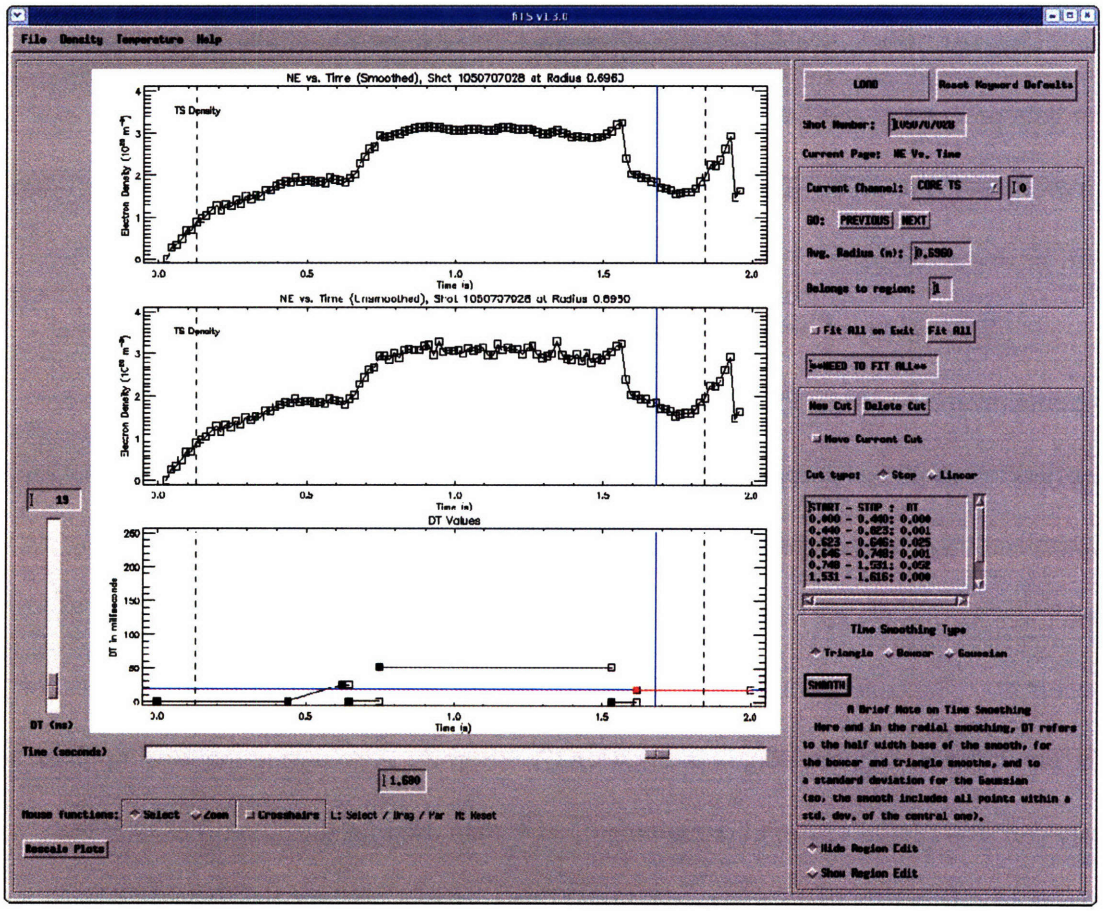

Figure 1: Density temporal smoothing page. Raw data vs. time for each individual core or edge TS channel are shown in the middle plot. A user can choose the time waveforms and type of temporal smoothing as shown in the lower graph. Smoothed data are shown on the upper plot. Different temporal smoothing can be applied to different radial regions.

Even though no temporal smoothing of the raw data is done by default, a user can and sometimes should take a look at the time evolution of the TS signals. The density smoothing page of the widget is shown in Fig. 1. Different phases of the discharge can be smoothed using different time windows. This is achieved through allowing a user to create waveforms as shown on the lower plot. Triangle, boxcar, and Gaussian windows of the specified widths can be used. Also a user can divide a radial profile into several zones (through Region Edit in the lower left corner of the page) and apply the chosen smoothing algorithm to each individual radial zone. Once the time fitting process is finished, an automatic profile refitting should be done as prompted by the GUI.

A generic view of the resultant density fitting is shown in Fig. 2.

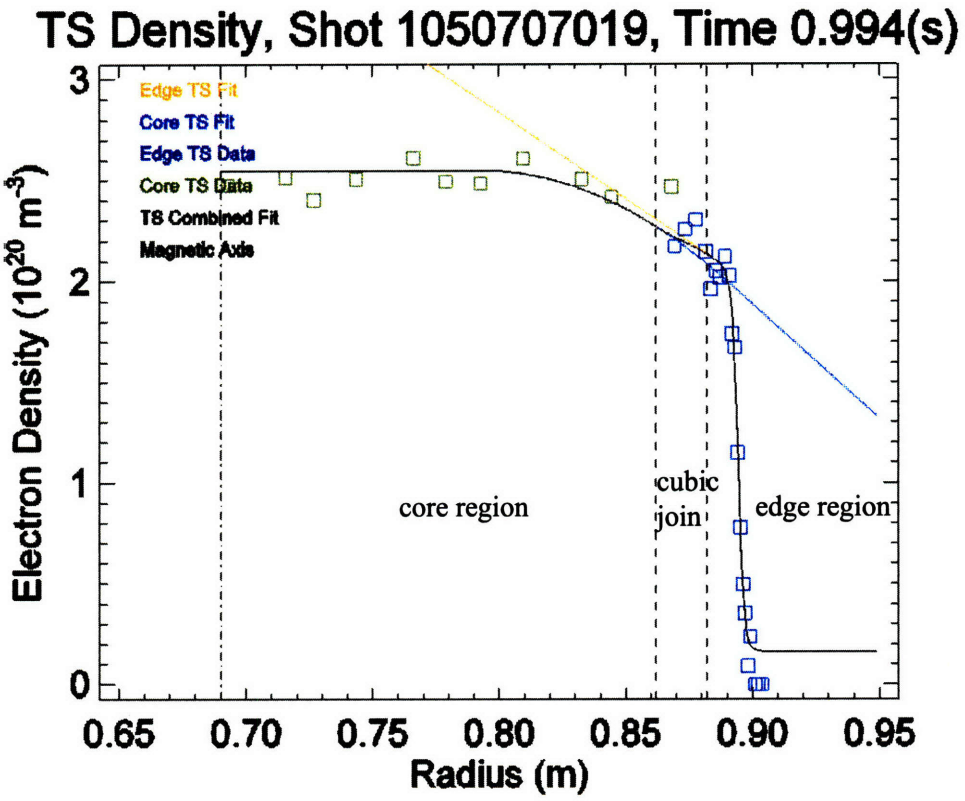

Figure 2: A general density fit for an H-mode plasma. Three radial regions with corresponding data points and fits are shown.

There are three distinct regions of the fit: core, edge, and the co-called cubic join. As it can be seen from Fig. 2, the characteristic scale lengths and the diagnostic resolution differs a lot for the core and edge plasma regions. This is why they are fitted separately and then stitched in a continuous fashion using a cubic spline.

The edge region consists of the data points from the edge TS diagnostic. A user can add a few data points (3 by default) from the core TS system to this profile. Radial smoothing can be applied with the smoothing window chosen by a user. The profile is fitted by the modified *tanh* function, which has the following form:

$$b + \frac{h}{2} * \left[1 + \tanh\left(\frac{r_0 - r}{\Delta}\right)\right] + m * \theta(r_0 - \Delta - r) * (r_0 - \Delta - r)$$

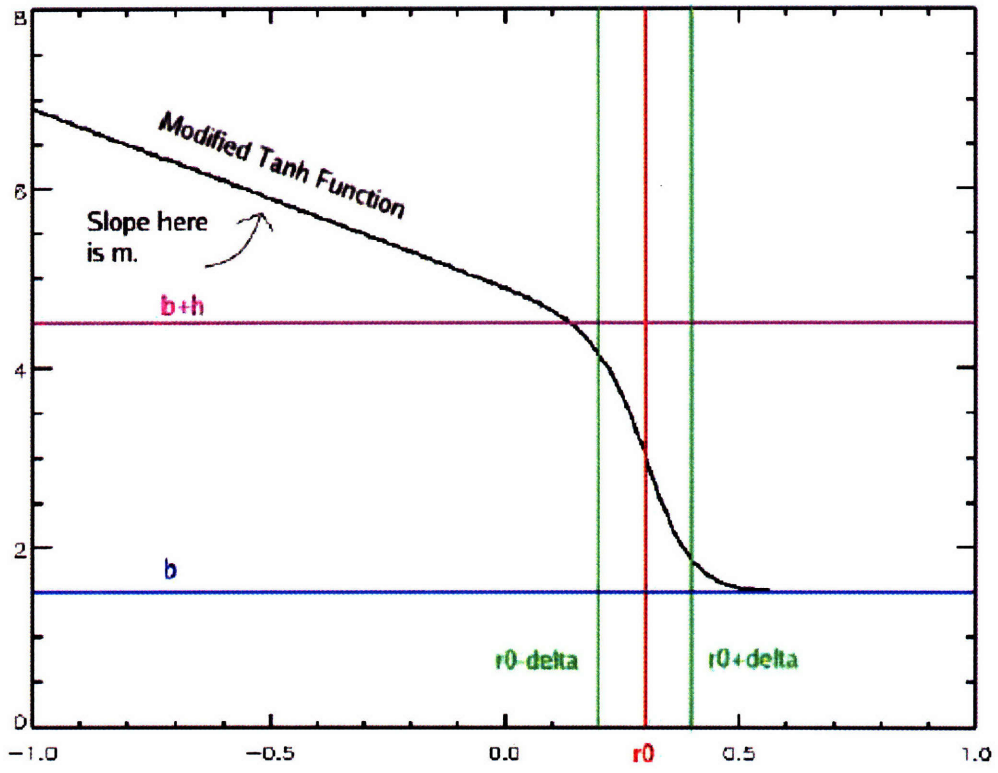

Figure 3 The modified hyperbolic tangent function.

This function has 5 parameters that define it: the midpoint, the height, the width, the outboard base level, and the inboard slope, as can be seen from the figure. Doing a check on these and other parameters such as χ^2 determines whether tanh fit is successful. It is empirically found that this type of function fits the edge region well, not only during the H-mode when an edge pedestal develops but also during L-mode. If the tanh fit is unsuccessful, then polynomial fitting is used. An example of the edge fitting page of the widget is shown in Fig. 4.

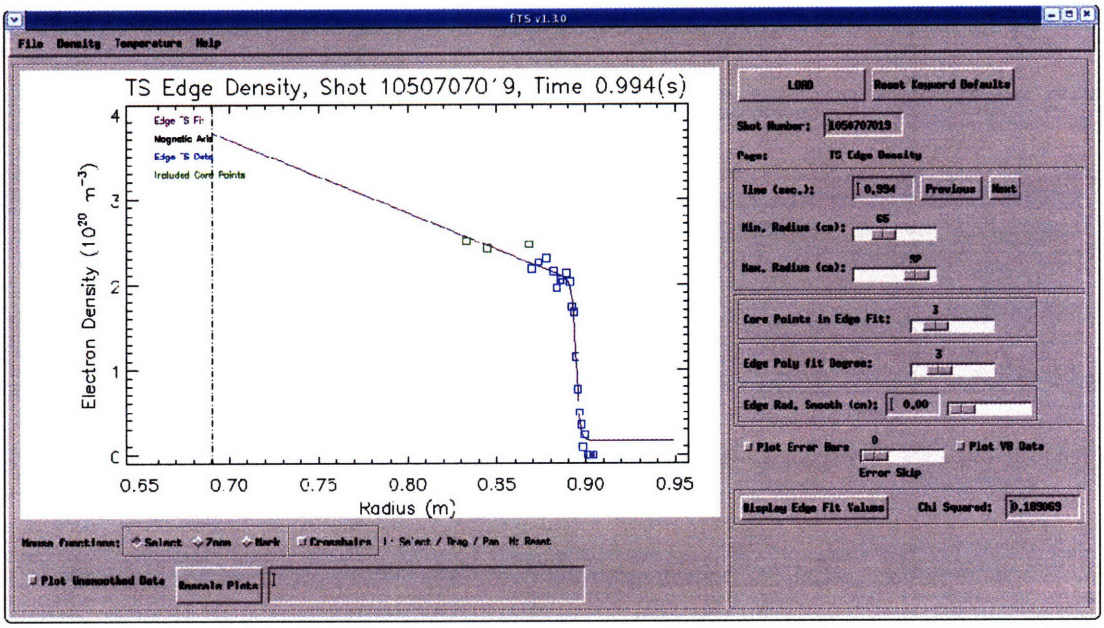

Figure 4: The edge density fitting page with the core and edge TS data shown in green and blue respectively.

The core region consists of the core TS data including a few data points from the edge TS system at the top of the pedestal. This region is fitted with B-spline, which takes into account experimental uncertainties in the measurements. The important fitting parameters for the B-spline are the order of the fitting and the number of knots, because they define how smooth the resultant profile will be. A user can change these, and different default parameters are used for the ITB and non-ITB phases of the discharge.

Higher order and more knots are used for fitting the ITB profiles. An example of the core density fitting page is shown in Fig 5.

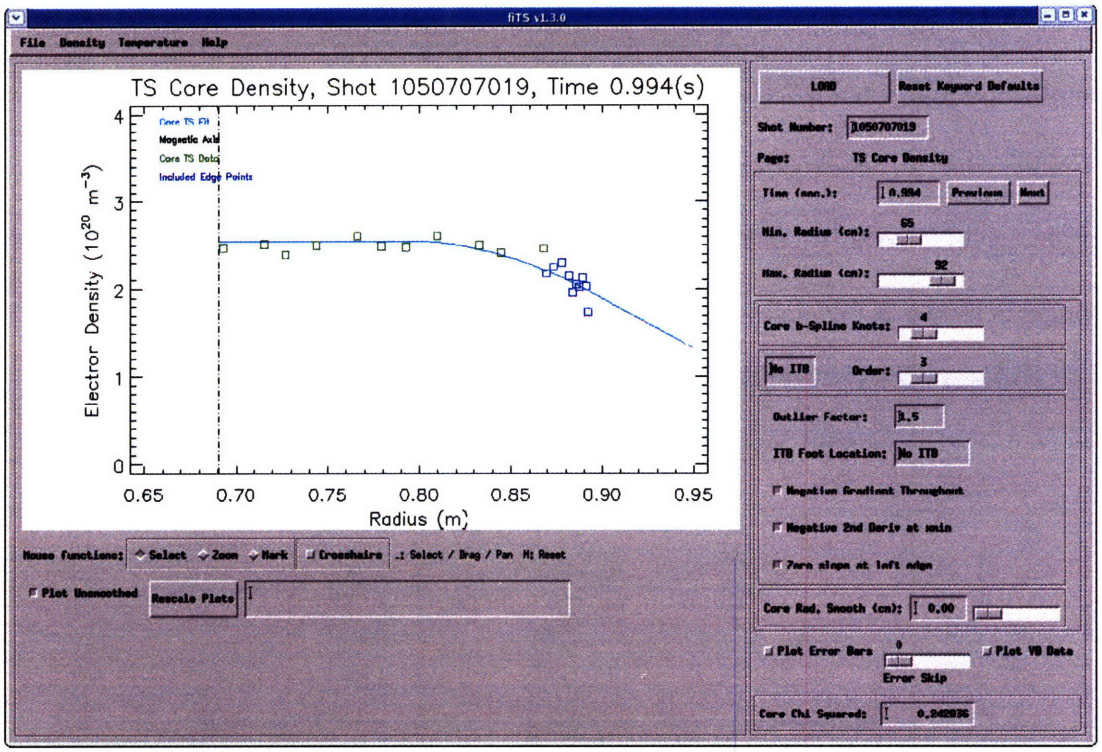

Figure 5: The core density page with the core and edge TS data shown in green and blue respectively.

A negative spatial gradient is assumed by default. However, this should not be used for the times shortly after the L-H transition when hollow density profiles are sometimes observed. Zero slope and negative curvature at the magnetic axis are also assumed. Radial smoothing can be applied. Also B-spline ignores data points that are outside a specified range from the resultant fit. This range is defined by the outlier factor (default value is 1.5).

The fact that a few edge data points are used for the core fit and vice versa ensures that they a close to each other in the overlapping region. These two are finally stitched together in a smooth fashion using a cubic spline, matching values and slopes at

two radial locations designated by the 'core join' and 'edge join' keywords. These locations are marked by the vertical lines in Fig. 2. By default the core join is calculated by the edge fit and defined as $r_0 - \Delta$ from the tanh parameters. The core join is taken to be 3 cm inboard. However, the user has freedom to change these values.

The resultant density fit is plotted on the combined density page of the widget (not shown). This page contains most of the fitting parameters described above. Keyword defaults can be reset on this page as well as the current set of parameters applied to all time slices. Here one can toggle plotting of data from individual diagnostics and individual fits. VB profiles can be plotted together with the density fit for comparison. Also a user can manually mark any data point as an outlier and exclude it from the analysis.

Using $n_e\sqrt{Z_{eff}}$ profiles from the VB measurements and the resultant density fits allows us to calculate Z_{eff} profiles. An example of the Z_{eff} page is shown in Fig. 6.

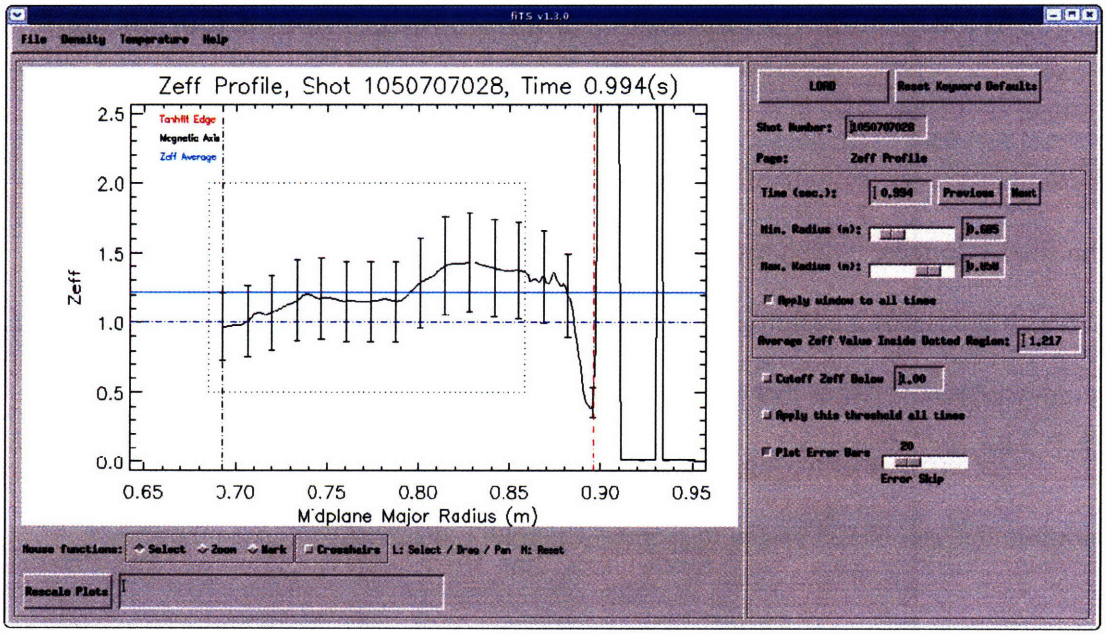

Figure 6: Z_{eff} page. Typical error bars are shown.

The widget returns profiles of Z_{eff} as well as the average values calculated within a certain radial range defined by the user. Since $Z_{eff} < 1$ is unphysical and is a diagnostic artifact, a minimum threshold can be applied.

A.2 Fitting of temperature profiles

For the temperature fitting, measurements from both the core and edge TS systems as well various ECE diagnostics (GPC, GPC2, FRCECE) are used. The fitting logic, algorithms, and data processing techniques are the same as for the density. Only important differences will be discussed.

The data reading routines identify which T_e diagnostic is available for a given shot and by default the widget uses all available data. All the data from the ECE systems are interpolated onto the TS time base. As a result, a lot of time dependence is lost and smooth T_e profiles thus obtained should not be used to study fast phenomena. One additional fitting parameter is the radius up to which ECE data are included in the core fitting. By default 0.85 m is chosen, because it was found empirically that ECE measurements are less reliable in the edge pedestal region. Another addition is the threshold parameter which is defined as the ratio of the actual density to the critical value at which the electron cyclotron emission from the plasma is cut off. This parameter helps remove ECE data points that are near the cutoff and thus not reliable.

An example of the temperature fitting page is shown in Fig. 8. In additional to plotting, the user has an option to specify which ECE diagnostic to use in the fitting.

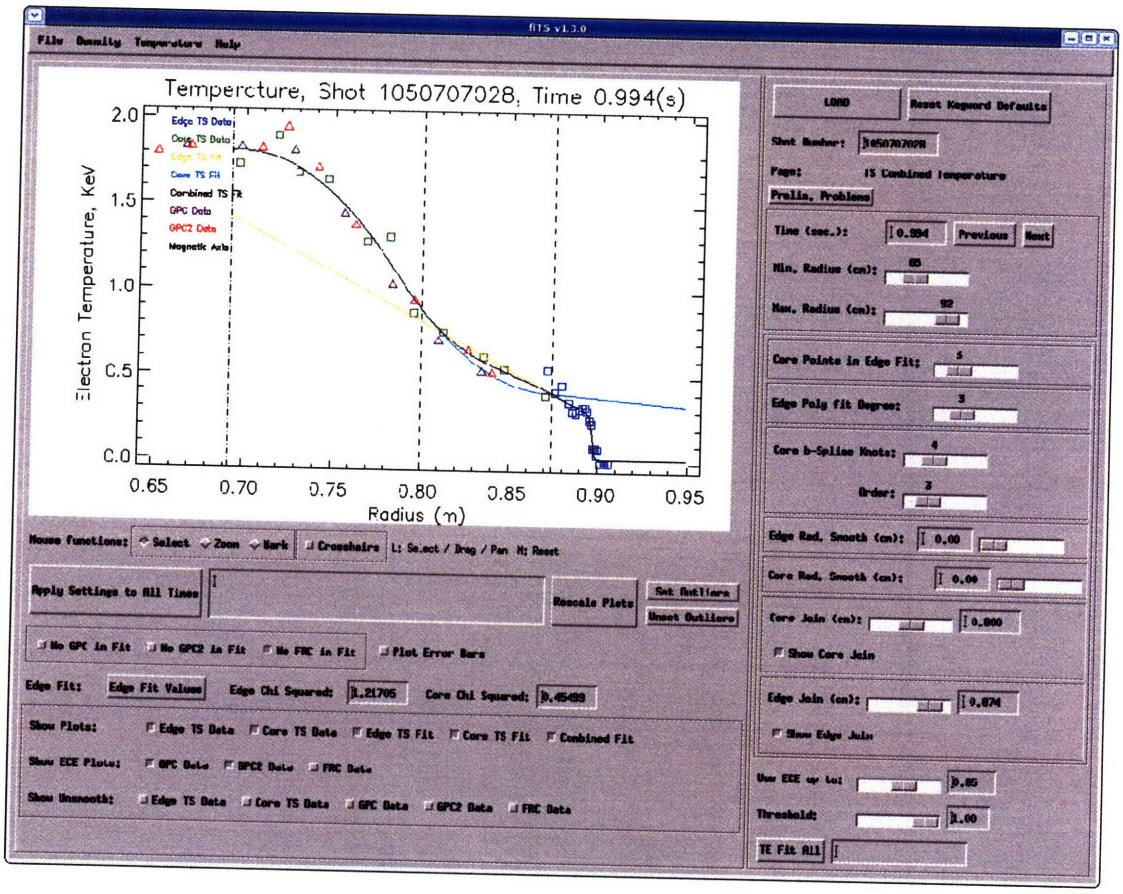

Figure 7: The combined temperature fitting page. Note different colors for different T_e diagnostics.

A.3 Summary

fiTS has proven to be a useful tool for visualizing and fitting density and temperature data obtained from various related diagnostics. This widget provides a user with a wide variety of options for data processing and fitting. Automatic profiles generated by the code are usually good enough for most applications. Buttons, keywords, and parameters are self-explanatory, however, a thorough documentation on this software exists. A curious reader can find it on the C-Mod Linux cluster under /usr/local/cmod/idl/fits/documentation.